STRUCTURAL, ELECTRICAL AND OPTICAL CHARACTERIZATION OF N- AND SI-IMPLANTED GASE SINGLE CRYSTAL GROWN BY BRIDGMAN METHOD

A THESIS SUBMITTED TO
THE GRADUATE SCHOOL OF NATURAL AND APPLIED SCIENCES
OF
THE MIDDLE EAST TECHNICAL UNIVERSITY

BY

ORHAN KARABULUT

IN PARTIAL FULFILLMENT OF THE REQUIREMENTS FOR THE DEGREE OF

DOCTOR OF PHILOSOPHY

IN

THE DEPARTMENT OF PHYSICS

NOVEMBER 2003

Approval of the Graduate School of Natural and Applied Sciences.

Prof. Dr. Canan Özgen
Director

I certify that this thesis satisfies all the requirements as a thesis for the degree of Doctor of Philosophy.

Prof. Dr. Sinan Bilikmen
Head of Department

This is to certify that we have read this thesis and that in our opinion it is fully adequate, in scope and quality, as a thesis for the degree of Doctor of Philosophy.

Assoc. Prof. Dr. Mehmet Parlak
Co-Supervisor

Prof. Dr. Bülent G. Akınoğlu
Supervisor

Examining Committee Members

Assoc. Prof. Dr. Mehmet Parlak

Prof. Dr. Raşit Turan

Prof. Dr. Çiğdem Erçelebi

Prof. Dr. Bahtiyar Salamov

Prof. Dr. Bülent G. Akınoğlu

ABSTRACT

STRUCTURAL, ELECTRICAL AND OPTICAL CHARACTERIZATION OF N- AND Si-IMPLANTED GaSe SINGLE CRYSTAL GROWN BY BRIDGMAN METHOD

Karabulut, Orhan

Ph.D., Department of Physics

Supervisor: Prof. Dr. Bülent G. Akınoğlu

Co-Supervisor: Assoc. Prof. Dr. Mehmet Parlak

November 2003, 119 pages.

Single crystals of GaSe were grown from the melt using 3-zone vertical Bridgman-Stockbarger system. In order to determine the doping effect, nitrogen and silicon ions were implanted to the grown crystals. Surface morphology and stoichiometry were examined using scanning electron microscope equipped with EDAX and structural properties were examined by X-ray diffraction technique. It was observed that the resulting ingot was stoichiometric and the structure was hexagonal. To identify the effects of ion implantation on the physical properties of the samples depending on annealing; electrical conductivity, Hall measurements,

current-voltage characteristics, photoconductivity and photoluminescence measurements were carried out in the temperature range of 100-450 K. Also, spectral transmission measurements were carried out for all the samples at room temperature.

It was observed that both N- and Si-implantation followed by annealing process decreased the resistivity values from 10^7 to 10^3 Ω-cm. Temperature dependent conductivity measurements were analyzed to deduce the dominant transport mechanisms. The trap levels were also investigated by the space charge limited currents (SCLC) measurements. The temperature dependence of hole concentrations showed that as-grown, N- and Si-implanted samples behave as partially compensated p-type semiconductors. Using suitable statistical method, transport parameters such as acceptor level, donor and acceptor concentrations were extracted from the experimental data.

Trapping centers and recombination mechanisms were determined from the temperature dependent photoconductivity measurements by investigating the relation between photocurrent and illumination intensity. N- and Si-implantation effects on GaSe were also examined by spectral photoconductivity and transmission measurements. And lastly, radiative recombination mechanisms in as-grown GaSe were investigated through photoluminescence (PL) measurements and the information related to the structural defects, the exciton levels and the structure of the forbidden gap were investigated.

Keywords: Crystal growth, Bridgman technique, GaSe, ion implantation, III-VI compounds, electrical characterization, optical characterization.

ÖZ

BRİDGMAN YÖNTEMİ İLE BÜYÜTÜLEN N- VE Si-EKİLMİŞ GaSe TEK KRİSTALLERİNİN YAPISAL, ELEKTRİKSEL VE OPTİK KARAKTERİZASYONU

Karabulut, Orhan

Doktora , Fizik Bölümü

Tez Yöneticisi: Prof. Dr. Bülent G. Akınoğlu

Ortak Tez Yöneticisi: Assoc. Prof. Dr. Mehmet Parlak

Kasım 2003, 119 sayfa.

GaSe tek kristalleri 3-bölgeli dikey Bridgman-stockbarger düzeneği kullanılarak büyütüldü. Katkılama etkisini incelemek amacıyla, büyütülen kristallere N ve Si iyonları ekildi. EDAX'lı taramalı elektron mikroskobu ve X-ışını kırınım cihazları kullanılarak, kristallerin yüzey biçimi, tamkatlılığı ve yapısal özellikleri incelendi. Kristallerin tamkatlı ve altıgensel yapıda olduğu belirlendi. İyon ekmenin, örneklerin fiziksel özellikleri üzerinde tavlamaya bağlı etkisini ortaya koymak için 100-450 K sıcaklık aralığında elektriksel iletkenlik, Hall, akım-voltaj, fotoiletkenlik ve fotoışıma ölçümleri yapıldı. Ayrıca oda sıcaklığında bütün örnekler için tayfsal geçirgenlik ölçümleri yapıldı.

N ve Si iyonları ekilmiş kristallerin tavlama sıcaklığına bağlı olarak özdirençlerinin 10^7 den 10^3 Ω-cm'ye kadar düştüğü gözlendi. Baskın taşıma mekanizmalarını belirlemek için sıcaklığa dayalı iletkenlik ölçümleri incelendi. Buna ilaveten, boşluk yükü sınırlı akım ölçümleriyle (SCLC) tuzak seviyeleri tesbit edildi. Sıcaklık bağımlı deşik derişim değerlerinden N ve Si ekili örneklerin kısmen denklenmiş p-tipi yarıiletkenler gibi davrandıkları gözlendi. Uygun istatiksel yöntemler kullanılarak alıcı seviyeleri, alıcı ve verici derişimleri gibi taşıma parametreleri deneysel verilerden çıkartıldı.

Sıcaklık bağımlı fotoiletkenlik ölçümleri kullanılarak fotoakım ile aydınlatma şiddeti arasındaki ilişki yardımı ile tuzaklama ve yeniden birleşim mekanizmaları tesbit edildi. GaSe tek kristallerine N ve Si ekilmesinin etkileri tayfsal fotoiletkenlik ölçümleri ile de çalışıldı. Ve son olarak ışımalı geçiş mekanizmaları, fotoışıma ölçümleriyle incelenerek yapısal bozukluklar, "exciton" seviyeleri ve yasak enerji aralığının yapısı araştırıldı.

Anahtar Kelimeler: Kristal büyütme, Bridgman tekniği, GaSe, iyon ekme, III-VI bileşikleri, elektriksel karakterizasyon, optik karakterizasyon.

To my mother and father

ACKNOWLEDGMENTS

I would like to express my sincerest appreciation to my supervisor, Prof. Dr. Bülent G. Akınoğlu, for his guidance, support, encouragement and his friendship throughout the course of this investigation. I would also like to express my deepest appreciation to my co-superviser Assoc. Prof. Dr. Mehmet Parlak for his guidance, patience, understanding and support during this study. I am indebted to Prof. Dr. Raşit Turan for stimulating guidance, discussions and laboratory opportunity. Appreciation is also extended to the members of this thesis committee, Prof. Dr. Çiğdem Erçelebi and Prof. Dr. Bahtiyar Salamov for their comments during the review of this thesis.

I wish also to thank my friends: Ergün Taşarkuyu, Koray Yılmaz, Tahir Çolakoğlu, Uğur Serincan, Bülent Aslan and Yücel Eke, for their valuable help, friendship and for the good times we had together.

Special thanks go to my brother Ahmet Karabulut and to all of my family members for their continuous support and love at the each stage of my educational life. Without them this work would never have come into existence.

I also should mention that this study were financially supported by METU-AFP under the project contract number AFP-2001-01-07-02-00-013. Without their support the content of this work would have been very limited.

TABLE OF CONTENTS

LIST OF TABLES

LIST OF FIGURES

CHAPTER 1

INTRODUCTION

Electrically, all the materials can be divided into three main groups, according to the ability of current carrying namely metal, insulator and semiconductor. Semiconductors are a group of materials having electrical conductivity intermediate between metals and insulators. Changing the temperature, optical excitation, and impurity content can vary the conductivity of these materials. This property makes the semiconductor materials attractive for electronic devices applications [1].

One of the most important characteristic of a semiconductor is its energy band gap and this property distinguishes it from metals and insulators. Energy band gap determines the wavelength of light that can be absorbed or emitted by the semiconductor. Since various semiconductors have wide range of band gap values, light-emitting diodes and lasers working at a wide range of wavelengths can be constructed in the near infrared and visible parts of the spectrum.

Semiconductor materials are found in column IV and neighboring columns of the periodic table. The column IV semiconductors are called elemental semiconductors because they are composed of single species of atoms. These are used for fabrication of integrated circuits elements such as transistors, diodes and rectifiers. They are also widely used in infrared and nuclear radiations detectors.

In addition to the elemental semiconductors, compounds of column III-V, II-VI and III-VI, make up the compound semiconductors. Like elemental semiconductors, compound materials become insulators at very low temperatures. At higher temperatures, however, the electronic bond can be broken and electrons can be excited into the conduction band.

In the last decades, considerable attention has been paid to the III-VI compound semiconductors, especially GaS, GaSe, GaTe, InS and InSe. They are the compounds between metals (Ga, In) and the chalcogens (S, Se, Te and O) and named as Ga- and In-chalcogens. The nature of the chemical binding in III-VI semiconducting compounds causes special features, such as layered and chain structure. These compounds have in common a distinctive property as they crystallize in layer structures which are extremely easy to cleave along the layers. The basic unit consists of two planes of metal atoms (M) sandwiched between two planes of selenium (or sulphur) atoms with the arrangement Se (or S)-M-M-Se (or S) [2]. Layers bound together by week wan der Waals forces while within the layer the bonding is covalent. These combinations of strong and weak bonds in the structure of the layer compounds resulted in a highly asymmetric charge distribution surrounding the atoms [3].

In recent years, much attention has been paid to the study of structural, electrical and optical properties of GaSe crystals. Optical and electrical properties of this highly anisotropic material makes it a promising semiconductor in optoelectronic devices especially in the visible and infrared ranges of the spectrum. Therefore, crystal structure of this material makes it an interesting subject of

study in solid state physics. But, it has been observed that the transport properties of this compound can vary from crystal to crystal depending on growth conditions. This variations make technological applications of GaSe very difficult. For specific technological applications, it is very important to control the electrical properties which can be adjusted by doping process. In general, the doping process is achieved by adding the dopants directly to the growth ampoules which is known as chemical technique. But in this method, it is quite hard to control the amount of impurity due to segregation and solubility problems. In order to avoid this difficulties, ion implantation technique was used for better dopant concentrations [4, 5, 6]. The main advantage of this technique is that the doping atoms can be implanted in different concentrations, independent of their solubility in the target materials. Therefore, the materials properties can be controlled by using the implantation technique, considering the doped region is only superficial.

1.1 Structure of GaSe

GaSe is a layered compound of the III-VI family with the direct band gap 2.0 eV at room temperature. The basic unit of this compound consists of two planes in which every Ga atom is surrounded by three Se atom and two sub-layers are bounded by Ga-Ga bridges [7]. Atoms within each layer are tightly bound with a mixture of covalent and ionic bonds, whilst the interlayer forces are of the van der Waals type [8] (Fig.1.1). The strong bonding inside the successive fourfold atomic planes and weaker van der Waals bonding between the layers results in anisotropic

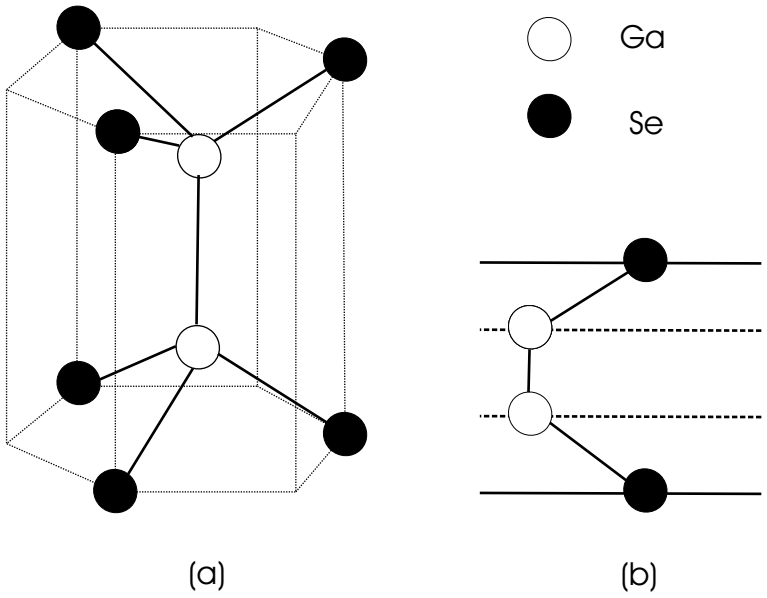

Figure 1.1: The crystal structure of GaSe. Figure (a) and (b) show the basic coordination unit and a section thought a single layer, respectively.

materials due to asymmetric charge distributions surrounding the atoms [9]. As a consequence of anisotropic bonding, there are four different polytypes which are β, γ, δ, and ϵ depending on growth conditions [10, 11, 12]. These are characterized by the different stacking sequences of their four-fold layers. These differences in stacking sequences result differences in interlayer interactions which have great importance for lattice dynamics calculations.

The crystals grown by Bridgman techniques usually have the ϵ-type structure with a variable amount of stacking faults. The lattice parameters a and c were found to be 3.75 and 15.95 A^o, respectively and the mean thickness of one layer were reported as 7.97 A^o for ϵ-type structure [13]. In general, the a value was reported about as 3.75 A^o for the four types of structure. The c values show differences depending on the type of the crystal and which were reported to

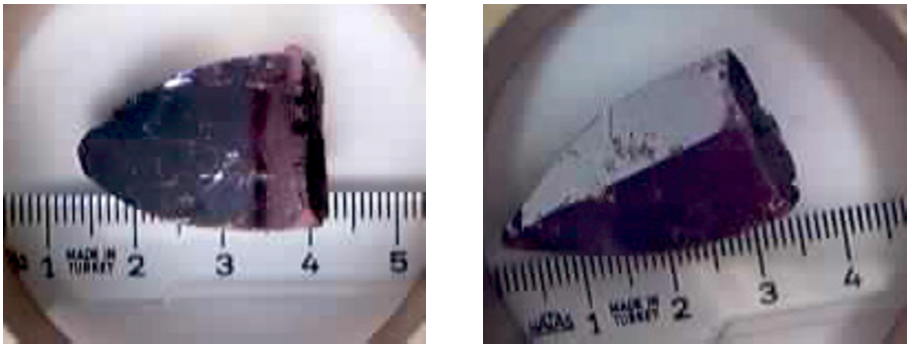

Figure 1.2: GaSe crystal ingots grown in our laboratory with layers parallel to the ampoule axis.

be 15.95, 23.86 and 31.99 A^o for β, γ, and δ-type structure, respectively. The interatomic distance between Ga-Se, Ga-Ga and Se-Se were reported to be 2.48, 2.38 and 4.77 A^o, respectively for ϵ-type GaSe crystals [9, 13].

It was generally reported that within each plane of GaSe crystal, the atoms are arranged in hexagonal or rhombohedral modifications and the c-axis is perpendicular to the layer plane [3, 14]. It is optically clear with dark red color and is easily cleavable. It has been shown that the crystal orientation depends on ampoule shape and the c-axis of grown crystals were perpendicular to the ampoule axis in pointed bottom ampoules [9]. Fig. 1.2 shows such a grown undoped GaSe crystals in our Bridgman system.

The band structure of GaSe single crystals have been studied extensively by theoreticians and experimentalists. The undoped GaSe is a p-type layered compound with a direct band gap around 2.0 ev at room temperature and having melting point at 960 ^{o}C [9]. The band calculations carried out by Schluter [15] revealed that this compound has indirect band gap lying very close to the direct

one. From the optical measurements, the direct and indirect gap of undoped GaSe were found to be 2.127 and 2.106 eV at 4.2 K, respectively [16]

1.2 Previous Studies

During the past, theoreticians and experimentalist extensively studied GaSe with respect to growth techniques [9, 11, 17, 18, 19, 20], structural [3, 7, 8, 9, 10, 11, 12, 14], electrical [14, 21, 22, 23, 24, 25] and optical properties [16, 26, 27].

Generally, GaSe crystals were grown by three methods which are Bridgman-Stockbarger (B-S), transport reactions and vacuum sublimation. The most common technique used to obtain large single crystals are the Bridgman-Stockbarger technique. Using various growth conditions such as, different ampoule shape, temperature profile, growth rate and furnace type, some studies have been carried out on undoped and doped GaSe single crystals [9, 17]. A detailed explantation of B-S technique is given in Chapter 2 and Chapter 3.

In 1986, Ishii et al. [18] obtained single crystal by vapor transport reaction using iodine as the transport agent. The stacking sequence of the as-grown crystal were either β- or ϵ-type with room temperature resistivity greater than 10^9 (Ω-cm). This stacking sequence was also observed in vapor phase grown GaSe crystals by Kuhn et al. [19]. The high electrical resistivity was attributed to the low concentrations of impurities. In the study of Cardetta et al. [28], the resistivity was reported as 2.2x10^8 (Ω-cm) by chemical vapor transport technique. Levy has reviewed the growth of layered crystal by vapor transport and Bridgman-Stockbarger method in which the transport agent and the growth parameters

were summarized in their study [20].

Terhell et al. [11], grew GaSe by using vacuum sublimation technique. It was reported that the different part of the grown ingot exhibits different polytypes. The top part of the needles was γ-type with ordered stacking sequence, whereas the bottom part was ϵ-type stacking which contains more than one dislocation.

A systematic investigation on electrical properties of undoped p-type GaSe grown from melt have been carried out in a wide temperature range of 77-850 K by Manfredotti et al. [22]. The resistivity of their crystals varied from 10^2 to 10^6 $(\Omega - cm)$ depending on growth conditions. It was reported that the resistivity is higher for uncoated ampoules and increasing with growth time. This increase was attributed to the chemical impurities steam from the interactions between material and silica ampoules. For carbon coated ampoules, the resistivity is lower and the growth time does not affect it. Five acceptor levels which are E_1=31, E_2=50-70, E_3=140-160, E_4=180-210 and E_5=280-310 meV were reported from the conductivity measurements. Some of these levels were attributed to the intrinsic acceptor centers, generated by structural defects. The other ones, and especially the deeper ones, were explained with the gallium vacancy and the chemical impurity resulting from the interaction between silica and GaSe.

A series of hole centers has also been observed with energy depths ranging from 26 to 400 meV with densities of about 10^{13} cm^{-3} from the dark conductivity and space-charge-limited current (SCLC) measurements [29]. In addition to these levels, three well defined deep-lying hole traps have been detected at 421, 465 and 543 meV above the valance band, and with concentrations ranging between

10^{12} and 10^{13} cm^{-3} from SCLC measurements [30].

Fivaz et al. [21] have studied the charge carriers and scattering mechanisms of this compound. Holes and electron mobilities have been measured as 50 and 250 $cm^2V^{-1}s^{-1}$, respectively along the layers from the Hall effect measurements. It has been observed that the mobility exhibits a temperature variation of the form $\mu \propto T^{\pm n}$, where n=2.1 for p-type GaSe. At lower temperatures, the Hall mobility is limited by impurity scattering, while at higher temperature it is controlled by phonon scattering mechanism with 40 meV phonon energy.

Because of the anisotropic properties of this layered compound, researchers have been focused on studying the electrical and optical properties along and perpendicular to c-axis. Augelli et al. [23] have measured the Hall mobility and resistivity both along and perpendicular to the layers. From the conductivity measurements, they obtained a higher resistivity value along the c-axis than along the layers with the same activation energy. Therefore, they concluded that the resistivity anisotropy is independent of temperature. From the Hall measurements, the mobility anisotropy has been found as $\mu_{\perp}/\mu_{//}$=3.5. From the mobility-temperature dependencies it was indicated that both mobilities are limited by homopolar optical-phonon scattering by Augelli et al. [23] The resistivity anisotropy of Gase has been measured by Tredgold et al. [8] and they observed that there is a relation between conductivity ratio and temperature variation such that $\sigma_{\perp}/\sigma_{//} \sim exp(\triangle E/kT)$, where $\triangle E$ is the barrier hight between the layers. Schmid et al. determined the barrier hight as 30 meV for p-type GaSe [24].

Capozzi et al. [31] studied trapping levels by means of SCLC measurements.

They observed that the trapping level is highly dependent on chemical purity of the samples. Single deep traps for the purest samples and continuous distribution of traps for heavily doped samples were reported in their study.

Capozzi et al. [26] reported the radiative recombinations of direct and indirect free excitons bound to the defect centers localized in the forbidden energy gap. Mainly, four peaks were observed at 2.098, 2.078, 2.035 and 2.002 eV at 80 K, and these peaks were attributed the direct free exciton (DFE), direct bound exciton (DBE), indirect free exciton (IFE) and indirect bound exciton (IBE), respectively.

Voitchovsky et al. [16] studied the photoluminescence of the pure and doped GaSe grown by Bridgman and transport reaction techniques. It was reported that there is a strong dependence of spectra on temperature below 40 K, and above this temperature, the spectra of all crystals were nearly the same. This behavior was explained by the rapid quenching of the luminescence resulting from recombination at trap states in between 20-40 K.

Mooser and Schluter [27] focused on the optical anisotropic nature of this layer compound. It was reported that if the electric field of the light is parallel to the c-axis, the direct optical transitions between the top of the valance band and the minimum of the conduction band are full allowed. For a perpendicular direction the transition is weakly allowed, due to spin-orbit coupling.

GaSe single crystals can be grown as both p and n type depending on growth conditions and dopant elements mostly added during the growth process [32]. The Bridgman grown undoped GaSe is p-type, while the crystals grown by transport method is n-type [9, 31]. Using Bridgman systems, GaSe single crystals

doped with different elements from different group by adding the impurities to the growth ampoule were produced and studied by various researchers. It was observed that iodine, chlorine [33], tin (Sn) [14, 32] and germanium [25] doped GaSe showed n-type conductivity, while As [25], Cd [34, 35, 36], Sb [37], Cu [38], Tm [39], Li [40], Ag [41], Zn [42], Gd [43], Mg [44], N-doped samples [45] showed p-type conductivity.

It is quite hard to control the amount of impurity in the method of adding the impurities to the ampoules due to segregation and solubility problems. The ion implantation technique does not render these difficulties however, interestingly we could only reach one article, in which PL spectra of GaSe doped with Cu atoms by ion implantation was reported [46]. The ion implantation technique is simply the launching of atoms onto the surface of the material by bombardment of the solid with energetic ions in the keV to MeV energy ranges. One advantage of this technique is that the doping atoms can be implanted in different concentrations, independent of their solubility in the target material [47]. Capozzi et al. have studied Photoluminescence spectra of Cu doped GaSe by ion implantation. It has been shown that this technique can be applied to the GaSe and the spectrum of the implanted sample was the same as that of chemically doped samples and no damage was produced by the ion bombardment [46].

1.3 Present Work

In this thesis, we grew and examined the structural, electrical and optical properties of the GaSe single crystal grown by Bridgman technique. The effect of

N- and Si-implantation on structural, electrical and optical properties by means of x-ray diffraction (XRD), temperature dependent conductivity and mobility, and photocurrent-illumination intensity dependence following to post annealing of the samples in the temperature range of 100-450 K were extensively studied to deduce physical and electrical properties of the GaSe single crystals.

A detailed theoretical background for structural, electrical and optical analysis of the grown and doped samples, and necessary theoretical information about transport properties that we used in the present work were given in chapter 2. In the next chapter, the experimental techniques used in this study were summarized starting from the ampoule cleaning procedure and synthesization to the crystal growth process. The experimental setup and methods were also explained in this chapter. The experimental results from the x-ray, electrical and optical measurements were given in chapter 4 together with detailed discussions about all the results. Finally, in Chapter 5, we have presented the general discussions and conclusions of our results.

CHAPTER 2

THEORETICAL CONSIDERATIONS

2.1 Introduction

In this chapter, methods of making crystals of semiconducting compounds were summarized. A detailed theoretical background and necessary information used for the structural, electrical and optical analysis of the grown and doped samples were also given in this chapter.

2.2 Crystal Growth

Crystal growth techniques can be separated into two main groups which are *epitaxial* and *bulk* growth according to their transition phase. The oriented growth of crystalline material on a single crystal surfaces of different materials is called *epitaxy* [48]. One can understand the epitaxial growth as the growth of a single crystal film on the surface of the same material or another substrate. In this process, the substrate serves as the seed crystal onto which the new crystalline material is grown. The growing crystal layer maintains the crystal structure and the orientation of the substrate. Using Epitaxial growth techniques, it is possible to grow a variety of crystals for electronic or optoelectronic device applications [1]. There are a lot of methods for epitaxial deposition of different materials. The

most widely used are Chemical Vapor Deposition (CVD), Liquid Phase Epitaxy (LPE), atomic Layer Epitaxy (ALE) and Molecular Beam epitaxy (MBE).

In the bulk growth, crystals can be grown from the melt by the Bridgman-Stockbarger technique, zone melting technique, Czochralski and Kyropoulos techniques. These techniques are quite adequate for compounds with a low pressure at the melting point. However, for compounds with relatively high vapor pressures some modification of apparatus is required.

The *Bridgman-Stockbarger* technique is used to produce about 40 % by weight of all the crystals grown. The reasons for this popularity are that it produces crystals quickly with good dimensional tolerances and employ relatively simple technology [49]. A detailed description of this technique was given in the next chapter. In this method, the crystal growth is achieved by slowly lowering a crucible containing a melt from an upper high temperature zone into a lower low temperature zone, which is operated at a temperature below the melting point. The crucible usually has a pointed bottom that enters the freezing zone first to avoid not more than one nucleation. As the crucible is lowered nucleation is occurred at the tip of the crucible and crystallization proceeds vertically as the melt passes down through the freezing isotherm [17].

In the *Zone melting* technique, polycrystal is loaded in a suitable container, then by constructing a small molten zone in an ingot of the material crystal is grown by moving this zone along the ingot several times. This process is called *Zone Refining*. This technique also helps considerable purification of the grown crystals since many impurities have a greater solubility in the melt than in the

solid. If a seed crystal is included in one end of the ingot, the method is called as *Floating-Zone* method [1].

In the *Czochralski* and *Kyropoulos* techniques, single crystals are grown from the melt by pulling. By these methods, it is possible to produce high quality crystals. At least half of the high quality crystals grown are by pulling from melt or by directional solidification [49]. There are some little differences between these two methods. In *Czochralski* growth, the material is melted in a suitable crucible and then is raised to a temperature a few degrees above the melting point. A suitable environment (vacuum or inert gas) is provided, according to the chemical nature of the material to be grown. The seed crystal, rotating slowly, is brought into contact with the melt surface. After reaching the thermal equilibrium, the seed is slowly raised from the melt, while the power supplied to the melt is simultaneously lowered. Growing occurs at the interface between solid and liquid phases [49]. *Kyropoulos* growth technique resembles that used for Czochralski growth but seed crystal is not raised upwards from the melt during growth. The major advantage of this growth technique is that it is possible to produce crystals with larger diameters than Czochralski growth [49].

2.3 Additions of Impurities

In order to modify the electrical and optical properties of the semiconductor for certain applications, impurities were introduced into the crystals. This process is called *doping*. If the added impurity results in additional electron (hole), the impurity is known as a donor (hole). There are two ways of doping

which are chemical and implantation. In the chemical doping technique, solute or dopant agent can be added directly to the melt or growth ampoule. Usually small amounts of impurity need to be added. The drawbacks of this method are segregation and solubility of the dopant elements in the host material.

Second and more controlled method is the implantation technique. This technique is simply the launching of atoms onto the surface of the material by bombardment of the solid with energetic ions in the keV to MeV energy ranges [47]. When an energetic ion enters a solid, it losses energy by elastic or inelastic collisions then give up their energy to the lattice atoms and finally come to rest. During this process, implanted ion beams introduce electrically active defects which can act either as traps or as recombination centers in semiconductors. Depending on the impurity and its implantation energy, implanted ions can penetrate from a few hundred angstroms to about 1μm which is called *projected range*. It is possible to calculate the average projected range theoretically. In almost all cases, in order to remove the damages introduced during the implantation and to restore the crystallinity, the implanted materials have to be annealed. The major advantage of this method is that the doping atoms can be implanted in different and desired concentrations, independent of their solubility in the target material.

2.4 Structural Characterization

The determination of structure of a grown crystal proceeds in three major steps; the shape and size of the unit cell are deduced from the angular positions of the diffraction lines. Then, the number of atoms per unit cell is computed from

the shape and size of the unit cell. Finally, the positions of the atoms within the unit cell are deduced from the relative intensities of the diffraction lines.

In order to determine the structure of the grown crystals, X-ray measurements were carried out. Since the atomic spacings are of the order of a few angstrom units ($10^{-10}m$), normal optical microscope technique do not provide sufficient resolution. However, X-ray is a form of electromagnetic radiation with a few angstroms wavelength and hence is useful for crystal structure determination.

There are three different important method for X-ray analysis of materials which are the Laue method, the rotating-crystal method and the powder method. In this work, the powder method was used for structural analysis. In this method, the position and intensities of the diffraction peaks are used to identify the structure of the substance. Analysis of the positions of the diffraction peaks gives information about the size, cell parameters, space group and orientation [50]. A monochromatic X-ray beam is directed onto a specimen which is crushed into fine particles. These little crystals will be randomly oriented with respect to the beam direction. The maximum diffraction conditions for a beam diffracted by atomic planes are given:

$$n\lambda = 2dsin\theta \tag{2.1}$$

which is known as Bragg equation. n is a positive integer and shows the order of reflection maximum, λ is the wavelength of the X-rays, d is the inter-planer spacing between successive atomic planes in the crystal and θ is the angle between the normal to the atomic plane both for the incident and reflected beams. Since

λ is fixed, there will be constructive interference observed at definite angles θ to the incident beams, owing to reflection from crystal planes of spacing d which happen to be oriented to satisfy the Bragg law (eq.2.1) [50].

To analyze the data obtained from the X-ray measurements, a computer program, TREOR90, was used. This program is a general trial-and-error indexing program for X-ray diffraction powder patterns written in Fortran by Werner et al. [51]. The program contains separate routines for cubic, tetragonal, hexagonal, orthorhombic, monoclinic and triclinic symmetries. TREOR90 searches for solutions in index space by varying the Miller indices.

2.5 Electrical Characterization

Electrical characterization in a semiconductor involves conductivity measurements, which give information about the nature of impurity and/or defects which are generally responsible for free carrier band population. In addition, Hall effect measurements have found wide application in the characterization of semiconductor materials, because it is possible to obtain the carrier concentration, mobility and scattering mechanisms from this measurement.

2.5.1 Fermi Dirac Distribution and Carrier Concentration in Semiconductor

Temperature-dependent conductivity and Hall measurements are very important in the electrical characterization of semiconductor. In semiconductor materials, theoretically there are no charge carriers at 0 K. As the temperature of a semiconductor is raised from 0 K, some electrons in the valance band receive

thermal energy and are excited to the conduction band. This process results in accommodation of some electrons in the conduction band and some holes remain in the valance band which are called electron-hole pairs (EHP).

A pure semiconductor crystal which contain practically no extraneous impurities is called *intrinsic* semiconductor. At higher temperatures electron-hole pairs are generated and EHPs are the only charge carriers in intrinsic materials. It is possible to create carriers in semiconductor by purposely introducing impurities into the crystal. A small number of impurity atoms produce a large effect on the electrical properties of semiconductors. This process, called *doping*, is the most common technique for varying the electrical end optical properties of semiconductor as we discussed in previous sections. There are two types of semiconductors, namely, n-type (charge carriers are mostly electron) and p-type (charge carriers are mostly holes). Materials having properties due to added impurities are called *extrinsic* semiconductors.

Electron in a solid obey Fermi-Dirac statistics and the probability of occupancy for a state of energy E at thermal equilibrium is given as;

$$f(E) = \frac{1}{1 + e^{(E-E_f)/kT}} \tag{2.2}$$

where E_f is the Fermi energy level. If density of available state in the energy interval E and $E+dE$ is $N(E)dE$, then the density of electrons in the conduction band can be written as;

$$n_0 = \int_{E_c}^{\infty} f(E)N(E)dE \tag{2.3}$$

This integral equation can be reduced to a simpler form as;

$$n_0 = N_c f(E_c) \tag{2.4}$$

where N_c is an effective density of states. That is, N_c represents all the states that are available within the conduction band as if they are located at the conduction band edge.

Effective density of states for the edge of the conduction and valance band are given as [52];

$$N_c = 2(\frac{2\pi m_n kT}{h^2})^{3/2} \tag{2.5}$$

and

$$N_v = 2(\frac{2\pi m_p kT}{h^2})^{3/2}, \tag{2.6}$$

respectively. Assuming that the fermi level E_f lies at least several kT below the conduction band ($(E_f - E_v) > kT$), the Fermi function can be written as;

$$f(E) \cong e^{-(E_c - E_f)/kT} \tag{2.7}$$

Then using Eqn.2.4, the electron concentration in the conduction band is

$$n_0 = N_c e^{-(E_c - E_f)/kT}. \tag{2.8}$$

By similar arguments, the hole concentration in the valance band is

$$p_0 = N_v e^{-(E_f - E_v)/kT}. \tag{2.9}$$

These electron and hole concentrations (2.8) and (2.9) are valid for intrinsic and extrinsic materials, provided that thermal equilibrium is maintained. For intrinsic materials, E_f lies at the same intrinsic level E_i near the middle of the band gap and the intrinsic electron and hole concentrations are [52];

$$n_i = N_c e^{-(E_c - E_i)/kT} \tag{2.10}$$

and

$$p_i = N_v e^{-(E_i - E_v)/kT}, \tag{2.11}$$

respectively.

The product of n_0 and p_0 at equilibrium is a constant for a particular material and temperature and it can be written conveniently as [1];

$$n_0 p_0 = n_i^2. \tag{2.12}$$

2.5.2 Electrical Conductivity

Electrical conductivity in an insulator or semiconductor can result only electrons (and the holes remaining behind in the valance band) which are excited from the filled valance band to the higher empty conduction band. The conductivity of a semiconductor σ is given by [53]

$$\sigma = q(\mu_n n_i + \mu_p p_i) \tag{2.13}$$

where q is the electronic charge, n_i and p_i are the intrinsic density of free electrons and holes, and μ_n and μ_p are the electron and hole mobility, respectively. If we consider an n-type semiconductor and substituting the electron concentrations

Eqn. 2.10 into Eqn. 2.13, we obtain

$$\sigma = N_c q \mu e^{-(E_c - E_i)/kT} \tag{2.14}$$

where μ is the electron mobility. From Eqn.2.5 we see that $N_c \alpha T^{3/2}$. There is also variation of μ with T. If the only effect on μ arises from interaction with crystal phonon, then according to theory in which scattering at low temperatures leads to a mobility variation as $\mu \alpha T^{-3/2}$ [54]. Thus, the conductivity expression can be written as;

$$\sigma = C e^{-(E_c - E_i)/kT} \tag{2.15}$$

where C is constant. If $\ln\sigma$ is plotted against $1/T$, the resultant curve will have a slope which permit the calculations of activation energies. The conductivity as a function of temperature is physically determined by excitation from valance to conduction band and also by the thermal raising of electrons from levels in the forbidden gap to the conduction band, and the capture of free electrons by free levels [52].

2.5.3 Hopping and Variable-Range Hopping

Another conduction mechanism is thermally activated *hopping* in which an electron from a state below the fermi level jumps to an another state above the Fermi level. This form of conduction is predominant in highly disordered materials at low temperatures. The probability of hopping (P) per unit time is the product of the Boltzmann factor [exp $(-W/kT)$], maximum phonon frequency ($\nu_{ph} = 10^{12} - 10^{13} s^{-1}$) and a jumping probability factor of electron from one state

to another [55]. Therefore, the probability of hopping is

$$P = \nu_{ph} exp[-2\alpha R - \frac{W \pm eRF}{kT}] \tag{2.16}$$

where R is the average hopping distance, W is the spacing between states near the Fermi level, F is the electric field and α is the quantity that represents the rate of fall-off of the wave function [55]. The current in this highly disordered medium is

$$J = 2eRkTN(E_f)\nu_{ph} exp(-2\alpha R - \frac{W}{kT}) sinh(\frac{eRF}{kT}). \tag{2.17}$$

For weak fields, $eRF << kT$, the conductivity is

$$\sigma = \frac{J}{F} = 2e^2R^2\nu_{ph}N(E_f) exp(-2\alpha R - \frac{W \pm eRF}{kT}) \tag{2.18}$$

where $e^2R^2\nu_{ph}N(E_f)$ is the pre-exponential constant (σ_{ho}) for hopping conduction. If $\alpha R > 1$ and $W > kT$, the variable range hopping is always to be expected. In this transport mechanism, the hopping distance R increases with decreasing temperature. This behavior was first pointed out by Mott and he gave the conductivity-temperature relation as $\sigma \sim exp(-T_o/T)^{1/4}$ at lover temperatures for highly disordered materials [55]. Thus, two possible mechanisms for conduction at high and low temperatures can be written as;

$$\sigma = \sigma_o exp(-\Delta E/kT) + \sigma_{ho} exp[-(T_o/T)^{1/4}] \tag{2.19}$$

where $T_o = 16\alpha^3/kN(E_f)$ is the degree of disorder. The average energy spacing between states near the Fermi level is

$$W = \frac{3}{4\pi R^3 N(E_f)} \tag{2.20}$$

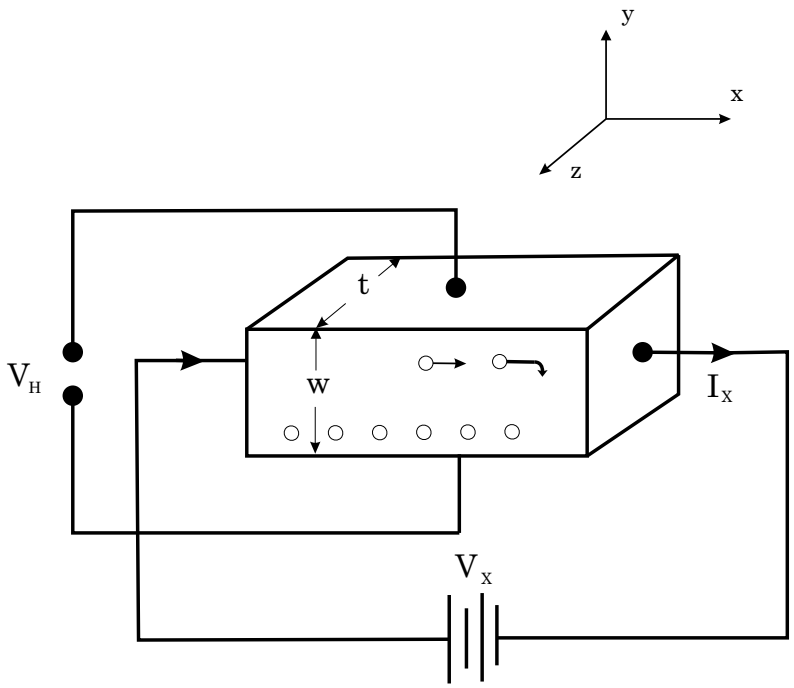

Figure 2.1: The Hall Effect.

and the hopping distance is

$$R = [\frac{9}{8\pi\alpha N(E_f)kT}]^{1/4}. \tag{2.21}$$

2.5.4 Hall Effect

In 1879, E. H. Hall discovered that a potential difference was developed in a material carrying a current in the presence of a magnetic field. Electrical conductivity and Hall coefficient can be measured using the circuit arrangement shown in Fig.2.1

The basic physical principle underlying the Hall effect is the Lorentz force. When an electron moves along a direction perpendicular to an applied magnetic field, it experiences a force acting normal to both directions and moves in response

to this force. If a magnetic field applied to a conductor perpendicular to the current flow directions an electric field perpendicular to both the magnetic filed and the current is produced so that a potential difference V_H is established within the material as shown in Fig.2.1 [54]. For a p-type, bar-shaped semiconductor, the total force on a single hole due to the electric and magnetic field is;

$$\mathbf{F} = q[\mathbf{E} + \mathbf{V} \times \mathbf{B}]. \tag{2.22}$$

We assume that a constant current I flows in the x-direction and a magnetic field B is applied in the z-direction. The current is given by;

$$I_x = qwtpV_x \tag{2.23}$$

where, p is the hole concentration, V_x is the drift velocity, w and t are width and thickness of the material, respectively. Holes experienced to the Lorentz force are deflected to the bottom of the sample, as indicated in Fig.2.1. In the y-direction, there is no net force on the holes and therefore $F_y = 0$. Combining Eqn.2.22 and 2.23, the electric field can be written as;

$$E_y = -\frac{B_z I_x}{qwtp}. \tag{2.24}$$

Thus, the Hall voltage V_H produced by the electric field in the y-direction

$$V_H = \frac{B_z I_x}{qtp}. \tag{2.25}$$

Hall voltage is proportional to the product of the current density and the magnetic flux density. The proportionality constant $R_H = r/qp$ is called the *Hall coefficient* where r is the scattering factor. A measurement of the Hall voltage for a known

current and magnetic field yields the hole concentration;

$$p = \frac{1}{qR_H}. \tag{2.26}$$

A similar derivation for n-type sample gives the electron concentration as;

$$n = -\frac{1}{qR_H}. \tag{2.27}$$

In order to determine both the mobility μ and the carrier concentration, a combination of a resistivity measurement and a Hall measurement is needed. The Hall mobility μ_H is defined by [54];

$$\mu_H = |R_H|\sigma. \tag{2.28}$$

Measurements of the Hall coefficient and the resistivity over a range of temperatures are extremely useful in the analysis of semiconductor materials because they give the carrier concentration, the mobility and also information about scattering mechanism.

2.5.5 Space-Charge-Limited Currents

Space-Charge-Limited current (SCLC) measurements have been a very useful tool for investigating the impurity level in solids. The study of the current-voltage characteristics gives information about the position of trapping states and their spatial density in the forbidden gap. In this method, an external field is applied into a crystal through an ohmic contact and the current passing through these contact is measured. When the material contains traps, a large fraction of injected space-charge condenses onto the traps. Therefore, only a small fraction of the

charge drawn into the material by the applied voltage contributes to the current conduction. If the field is large enough, the traps are saturated and electrons will be injected into the bulk of the material to form a current that is limited by Space-charge considerations [56].

In order to determine the total trap density and the location of trapping levels, the variation of current as a function of applied electric field to the material is measured. The trap parameters can be evaluated by means of a suitable method. The choosing of the method to analyze depends on the relation between current and voltage.

When a single set of traps are present in the forbidden gap of a material, the trap density and position can be determined according to the model proposed by Mathur and Dahiya [57]. According to this theory, the I-V characteristic shows an ohmic behavior at low voltage values. This region is followed by a superlinear region for increasing voltage. In this region, the current density is given by the relation;

$$J_s = (\frac{2l+1}{l+1})^{l+1}(\frac{l}{1+l})^{l}(\frac{\epsilon}{N_t})e^{(1-l)}\mu_e N_c exp(-E_t/kT)\frac{V^{l+1}}{d^{2l+1}} \tag{2.29}$$

where $l = T_t/T$ and T_t is the characteristic temperature of the trap distribution, T is the absolute temperature, ϵ is the static dielectric constant, μ_e is the electron mobility parallel to the c-axis, d is the distance between the electrodes, N_c is the effective density of states in the conduction band, V is the applied voltage, N_t is the total concentration of traps, and E_t is the depth of the traps below the bottom of the conduction band. In the square region(l=2), the current density

is described as,

$$J = \frac{9}{8}\frac{S\epsilon\mu_e\theta V^2}{d^3} \tag{2.30}$$

where S is the area of the contacts and θ is the ratio between the free electron density n and the trapped electron density n_t, and given as;

$$\theta = \frac{N_c}{\beta N_t} exp(-E_t/kT) \tag{2.31}$$

where β is the degeneracy factor. Following the superlinear region, the current rises very abruptly and this vertical region is called trap-filled limit (TFL). This is because the complete filling of trapping levels occurs and starts the voltage V_{TFL} which is given by;

$$V_{TFL} = \frac{ed^2N_t}{2\epsilon}. \tag{2.32}$$

The trap density can be evaluated from the Eqn.2.32 using the experimental value of V_{TFL}. Trap position E_t can be determined by the help of Eqn.2.30 and Eqn.2.31.

In some cases, especially in layered semiconductors, it is difficult to measure the transport properties along the c-axis. Therefore, in order to determine the trap level E_t, the I_{TFL} is measured as a function of temperature at a fixed voltage. The energy level E_t can be obtained from the slope of $\ln(JT^{-3/2})$ versus $1/kT$. The slope of this straight line gives E_t [33]. Another reliable technique for obtaining E_t is to measure the θ as a function of temperature in the superlinear region. Then plot of ln θ versus 1/kT will be a straight line and whose slope will give the trap position. The intercept of this plot at is $\ln N_c/\beta N_t$ and from its value, the trap density N_t can be calculated.

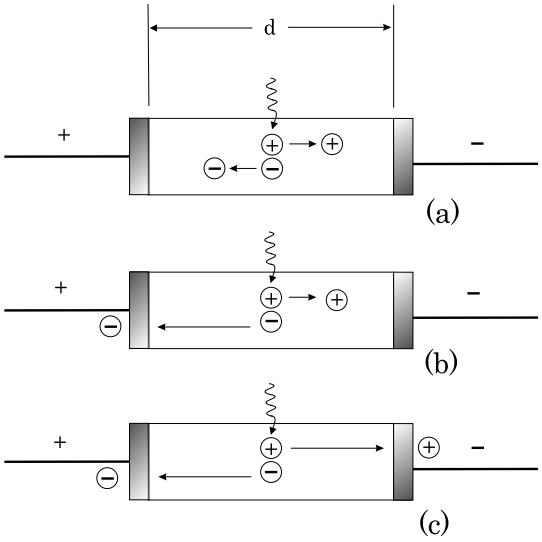

Figure 2.2: Photoconductivity process depending on the range of applied field.

2.6 Photoconductivity Processes

2.6.1 General Mechanism

The conductivity of an insulator or semiconductor was expressed in Eqn.2.13. When excess electrons and/or holes are created in a semiconductor, it causes an increase in the conductivity of the sample. If the excess carriers arise from optical excitation, the resulting increase in conductivity is called *photoconductivity*. This important effect helps the analysis of semiconductor materials and operation of several type of devices [52].

As given in Bube [52], Fig.2.2 shows the schematic representation of charge transport by electrons and holes for an illuminated photoconductor. If the applied field is low, both carriers are trapped in the crystals and they can not reach to the electrodes. In the low applied field, the photocurrent varies linearly with field and the gain is much less than unity (Fig.2.2-a). As the field increases, carriers

with higher mobility can arrive at the electrodes before being trapped, and the gain will be between an-half and one (Fig.2.2-b). Finally, both carriers can be drawn out before they are trapped when the field reaches to a certain value so that the photocurrent saturates. In this case, the gain is unity (Fig.2.2-c).

2.6.2 Recombination Kinetics

Let us consider the case that the light is falling on a homogenous material in which there is only one-carrier transport in the semiconductor. The photo-excitation may change both the carrier density n and the carrier mobility μ then the total conductivity can be given as;

$$\sigma_L = \sigma_o + \Delta\sigma = q(n_o + \Delta n)(\mu_o + \Delta\mu) \tag{2.33}$$

where Δn and $\Delta\mu$ are the increases in the carrier density and the mobility, and $\sigma_o = n_o q \mu_o$ is the dark conductivity. The increase in the conductivity can be written as;

$$\Delta\sigma = q\mu_o \Delta n + (n_o + \Delta n) q \Delta\mu. \tag{2.34}$$

The change in the carrier density can be written in terms of photo-excitation rate, ϕ $(m^{-3}s - 1)$ and the electron lifetime τ_n as $\Delta n = \phi\tau_n$, then the change in the conductivity is

$$\Delta\sigma = q\mu_0\tau_n\phi + nq\Delta\mu \tag{2.35}$$

In Eqn.2.35, for constant lifetime, the photoconductivity is proportional to ϕ and the change is

$$\Delta\sigma = q\mu_0\tau_n\phi \tag{2.36}$$

In this case, the slope log-log of $\Delta\sigma$ vs ϕ gives 1.

If the lifetime is a function of ϕ, then the change in the photoconductivity can be written as;

$$\Delta\sigma = q\mu_0\tau_n(\phi)\phi \tag{2.37}$$

If τ_n varies as ϕ^{n-1}, than $\Delta\sigma$ varies as ϕ^n and if $n < 1$, the lifetime decrease with increasing excitation rate and the behavior is said *sublinear*.

The values of n can be calculated from photoconductivity-light intensity dependence and it determines the recombination mechanisms within the material of study. If $0.50 < n < 1.0$, the recombination is dominated by a single type of imperfection level. One-center recombination model can explain this dependence and the variation obeys the power law as $\Delta n \propto \phi^n$. The $n = 0.50$ regime corresponds to *bimolecular recombination* and in this case the lifetime decrease with increasing photo-excitation rate. The presence of the traps increases as the n changes from 0.5 to 1.0, and $n = 1.0$ regime corresponds to *monomolecular recombination* in which the lifetime is constant and controlled by dark properties of the semiconductor [58]. Experimentally, a wide variety of values of n are observed with values between 0.50 and 1.0, as well as values larger than 1.0. A model has been developed for such a possibility in which $n = 0.50$ is characteristic of bimolecular recombination at the surface, and $n = 1.0$ regime is characteristic of monomolecular recombination in the bulk.

If $n > 1$, the lifetime increases with increasing excitation rate, and the behavior is said to be *superlinear*. In this case, the incorporation of additional imperfections

leads to a larger lifetime for one of the carriers than was previously present, i.e., the material is becoming more photosensitive with increasing photo-excitation intensities [58].

2.6.3 Partly Compensated Impurities (Single Donor-Single Acceptor Model)

Doping of semiconductor material by different impurities is a simple and effective way to control the electrical properties. Semiconductor can be doped either by donor atom which makes the material n-type or by acceptor atom which makes the material p-type. In real cases, the semiconductor materials have intrinsically both donor and acceptor atoms.

Assuming that a semiconductor contains both donors with density N_d and acceptors with density N_a, and if $N_d > N_a$ the material is n-type. In such a semiconductor, an acceptor state may be filled with a valance band electron and the resulted hole in the valance band is filled by recombination with one of the conduction band electrons. If all the levels of the acceptor atoms were filled then the electron concentration in the conduction band would reduce to a value $N_d - N_a$ instead of N_d. This process is called *compensation*. In such process, the material must be electrically neutral (Space-charge neutrality). If the material is doped n-type ($n_0 \gg p_o$) and all the impurities are ionized, the electron concentration approximately is;

$$n_o = (N_d - N_a). \tag{2.38}$$

The carrier concentration obtained from Hall effect measurements can be used

to extract additional information [59]. In a realistic case, a semiconductor contains both donors and acceptors. Let us consider an n-type semiconductor of doping concentration N_a compensated with donors of concentration N_d. A donor is electrically neutral if it has an electron trapped. For a non-degenerate semiconductor, as a result of compensation process, the number of electrons remaining in the donor level E_d or the density of neutral donor are given as;

$$N_{dn} = \frac{N_d}{1 + \beta exp[(E_c - E_d - \phi)/kT]} \tag{2.39}$$

where β is the spin degeneracy and since the level can be occupied by an electron in two ways, $\beta = \frac{1}{2}$. When the impurity is an acceptor center, the spin degeneracy is $\beta = 2$. This is because the absence of electron can be described in two ways. When the compensation is occurred, the density of ionized donors (N_{di}) is equal to $N_d - N_{dn}$. Remembering the charge neutrality of a semiconductor, the number of ionized donors is also equal to $(n_o + N_a)$. Therefore, we can write;

$$n_o + N_a = N_d - \frac{N_d}{1 + \beta exp[(E_c - E_d - \phi)/kT]}. \tag{2.40}$$

If we define a dimensionless notation such that $\epsilon_d = [\frac{E_d}{kT}]$ and $\eta = [\frac{\phi - E_c}{kT}]$, for a partly compensated semiconductor we have;

$$n_0 + N_a = N_d[1 + \beta^{-1} exp(\epsilon_d + \eta)]^{-1}. \tag{2.41}$$

It is always possible to find a mutually consistent values of ϵ_d and η. Using the value of n_o and solving Eqn.2.41 by the help of Fermi integral, one can find the

free electron concentration as;

$$n_0 = \frac{2(N_d - N_a)}{[1 + (N_a/\beta N_c)e^{\epsilon_d}] + \sqrt{\{[1 + (N_a/\beta N_c)e^{\epsilon_d}]^2 + (4/\beta N_c)(N_d - N_a)e^{\epsilon_d}\}}} \tag{2.42}$$

In order to analyze the experimental data, Eqn.2.41 can be rearranged as;

$$\frac{n_0(n_0 + N_a)}{(N_d - N_a - n_0)} = \beta N_c exp(-E_d/kT). \tag{2.43}$$

Now our task is to find the values for N_a and N_d which will permit the two sides of Eqn. 2.43 to be equal at all temperatures. $(N_d - N_a)$ can be estimated from the limit of n_0 in the exhaustion range. To calculate the parameters of donor level from the experimental results, the logarithm of the left-hand side of Eqn. 2.43 versus 1/kT is plotted with N_d and N_a as fitting parameters. Then, the method of least squares is applied to find the parameters N_a, N_d and E_d. For a non-degenerate p-type semiconductor, the hole concentration is given by;

$$\frac{p_0(p_0 + N_d)}{(N_a - N_d - p_0)} = \frac{N_v}{\beta} exp(-E_a/kT) \tag{2.44}$$

with $N_v = 4.82 \times 10^{15}(m_h/m_0)^{3/2}T^{3/2}(cm^{-3})$, where E_a is the activation energies of acceptor level, N_a and N_d are the concentrations of the acceptor and donor, respectively.

2.7 Optical Characterization

2.7.1 Absorbtion

The mostly used and the simplest method for a rough examination of the band structure of a semiconductor is to measure the optical transmission or absorbtion

spectrum. In the absorbtion process, photons of known wavelength are directed to the sample and these photons excite an electron from a lower to a higher energy state. Photons with energies greater than the band gap energy are absorbed while photons with energies less than the band gap are transmitted. Therefore, these experiments give an approximate measure of the band gap energy and even sometimes at low temperatures the impurity levels.

The fundamental absorbtion refers to band-to-band transitions. In this process, a photon with energy $h\nu \geq E_g$ can be absorbed in a semiconductor and causes an excitation of an electron from the valance band to the conduction band. The absorbtion coefficient is given by;

$$\alpha(h\nu) = A \sum P_{if} n_i n_f \tag{2.45}$$

where A is a constant, P_{if} is the probability of the transitions from the initial to the final state, n_i is the density of electrons in the initial state and n_f is the density of empty final states [60].

The fundamental absorbtion process is strongly affected by whether the band gap is direct or indirect. Therefore, the transitions can be separated into two groups which are direct and indirect transitions as shown in Fig. 2.3.

The *direct transition* is represented by a vertical line on a plot of energy (E) versus momentum (k). These transitions are two type which are *allowed* and *forbidden* direct transitions. In an allowed direct transitions, which are all the momentum-conserving transitions, both conduction and valance band extremes

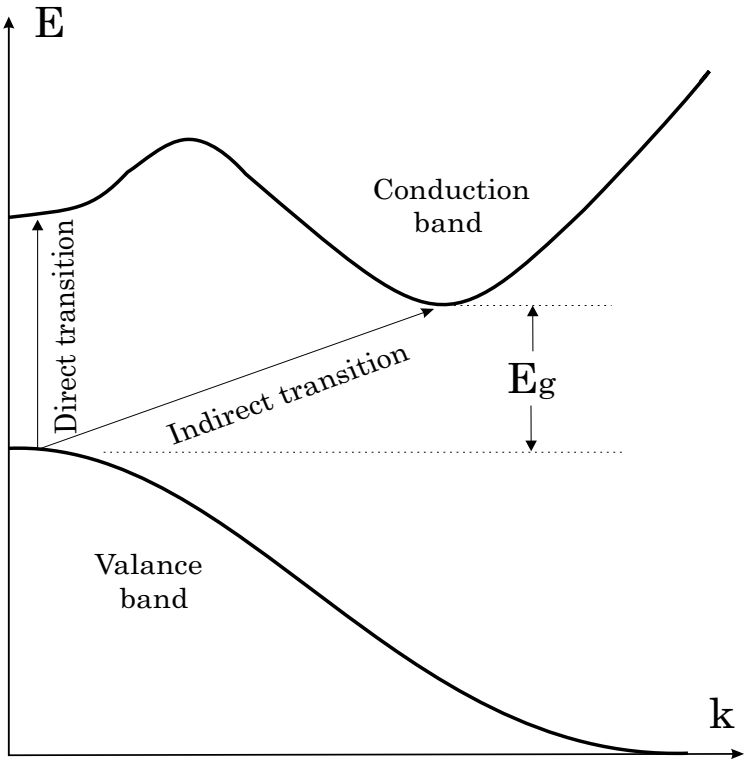

Figure 2.3: Direct and indirect transitions between valance and conduction band.

are located at the same value of k and thus, $\Delta k = 0$. In this transition, every initial state at E_i is associated with a final state E_f such that

$$E_f = h\nu - |E_i| \tag{2.46}$$

and the absorption coefficient for allowed direct transition is given as [61]

$$\alpha(h\nu) = A^*(h\nu - E_g)^{1/2} \tag{2.47}$$

where A^* is given by:

$$A^* \approx \frac{q^2(2\frac{m_h^* m_e^*}{m_h^* + m_e^*})^{3/2}}{nch^2 m_e^*}. \tag{2.48}$$

In some materials, quantum selection rules forbid direct transitions at $k = 0$ but allow them at $k \neq 0$, and generally the transition probability is increasing

with k^2. This means that the transition probability increases proportionately to $(h\nu - E_g)$. Therefore, the absorbtion coefficient for the forbidden direct transition is [61]:

$$\alpha(h\nu) = A^{'}(h\nu - E_g)^{3/2} \tag{2.49}$$

where $A^{'}$ is given by

$$A^{'} \approx \frac{4}{3}\frac{q^2(\frac{m_h^* m_e^*}{m_h^* + m_e^*})^{5/2}}{nch^2 m_e^* m_h^* h\nu}. \tag{2.50}$$

In some materials, the conduction band minimum occurs for different k values from the valance band maximum. This transition is called *indirect transition* and it requires a change in both energy and momentum. Therefore, two-step process is required because the photon cannot provide a change in momentum and momentum is conserved via a phonon interaction. In order to complete the transitions from the initial state E_i to the final state E_f, a photon with energy E_p is either emitted or absorbed with ν_e and ν_a, respectively. These two processes are given by [61]

$$h\nu_e = E_f - E_i + E_p \tag{2.51}$$

and

$$h\nu_a = E_f - E_i - E_p. \tag{2.52}$$

The absorbtion coefficient is proportional to the product of the densities of initial states, final states and the number of interacting phonons. The number of emitted or absorbed phonons is given by Bose-Einstein statistics as;

$$N_p = \frac{1}{[exp(\frac{E_p}{kT}) - 1]}. \tag{2.53}$$

Therefore, in an indirect semiconductor, the absorbtion coefficient for a transition with phonon absorbtion and phonon emission are given respectively by [61]

$$\alpha_a(h\nu) = AN_p(h\nu - E_g - E_p)^2 \tag{2.54}$$

for $h\nu > E_g - E_p$ and

$$\alpha_e(h\nu) = AN_p(h\nu - E_g + E_p)^2 \tag{2.55}$$

for $h\nu > E_g + E_p$.

2.7.2 Photoluminescence

Photoluminescence is a very powerful non-destructive technique for the determination of certain impurities in semiconductors. In this process, the sample is excited with an optical source, typically a laser with $h\nu > E_g$. In optical excitation, a photon is absorbed by the semiconductor, creating an electron-hole pair which then recombines, emitting another photon [53]. This process is *radiative* recombination. For *non-radiative* processes photons are not emitted but the initial photon energy is absorbed by other mechanisms. For good PL output the majority of recombination processes must be radiative. The determination of impurities is easy with this technique, but measurement of the concentration of impurities is rather difficult. In order to obtain the full spectroscopic information about the examined materials, low temperature measurements are necessary. Lower temperatures reduce the thermal line broadening and thermally activated non-radiative recombination processes. Therefore, cooling produces sharper peaks.

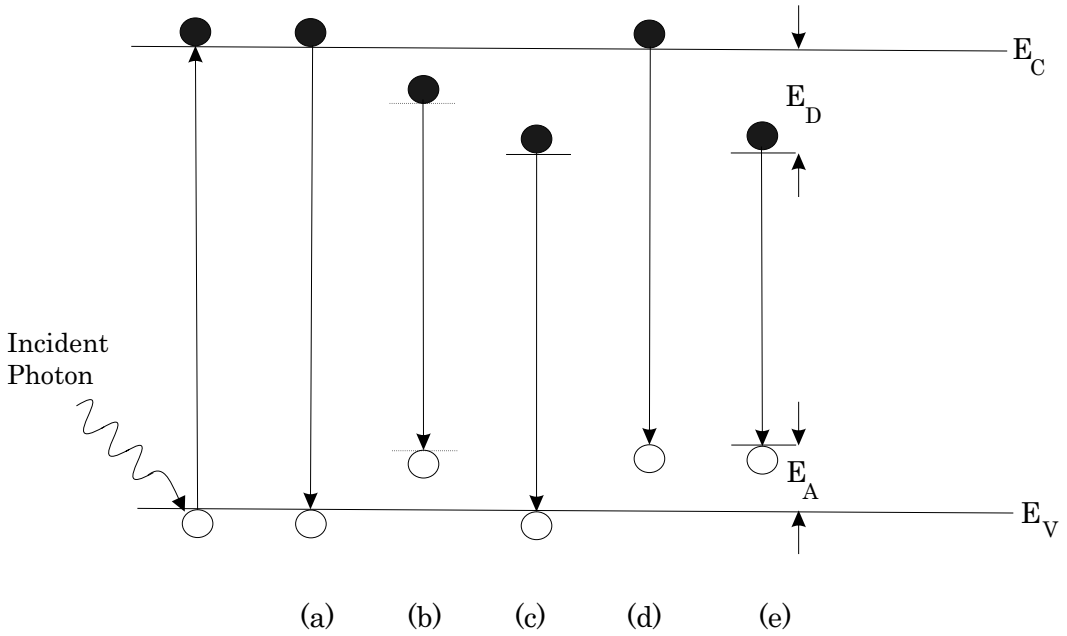

Figure 2.4: Radiative transitions observed with photoluminescence.

If the recombination is radiative, as a result of the return from the final state to the initial state a photon is emitted whose energy gives the difference between the excited and the initial state energies as illustrated in Fig. 2.4. In this figure, five of the most commonly observed PL transitions are shown. The first one is the *band-to band* recombination and dominates at room temperature, Fig. 2.4(a). If the material is sufficiently pure, *Free exciton* is commonly observed as given in Fig. 2.4(b). When a photon generates an EHP, columbic attraction can lead to the formation of an excited state in which an electron and a hole remain bound to each other in a hydrogenlike state. This excited state is referred to as a *free exciton* (FE). The electrons and holes generated by the optical source then recombine, emitting a narrow spectral line. In a direct gap semiconductor, the

energy of the emitted photon is simply

$$h\nu = E_g - E_x \tag{2.56}$$

where E_x is the excitonic energy. In an indirect-gap semiconductor, momentum conservation requires that a phonon to be emitted to complete the transitions. Then the energy of the emitted photon is

$$h\nu = E_g - E_x - E_p \tag{2.57}$$

where E_p is the phonon energy.

In the presence of the impurities, *Bound exciton* (BE) may be observed. A free hole can combine with a neutral donor to form a positively charged excitonic ion and similarly a free electron can recombine with a hole on a neutral acceptor as shown in Fig. 2.4(c) and (d). When these excitons recombine, their emission is characterized by a narrow spectral width at a lower photon energy than that of the free exciton [61]. Often, both free and bound excitons occur simultaneously in the same material, in which case each can be identified by its energy and line width. Bound exciton recombination dominates over free exciton recombination for less pure material. The full width at half maximum (FWHM) for BE transitions are typically less than or equal to $kT/2$ and resemble slightly broadened delta functions. This distinguishes them from FE which are usually a few kT wide.

When both donor and acceptor impurities are present in a semiconductor, the well-known *donor-acceptor* (D-A) recombination may occure. In this case, an electron on a neutral donor can recombine with a hole on a neutral acceptor

as illustrated in Fig. 2.4(e). Columbic interaction between donor and acceptor modifies the binding energies and therefore the emission line has an energy;

$$h\nu = E_g - (E_A + E_D) + \frac{q^2}{\epsilon r} \tag{2.58}$$

where r is the distance between donor and acceptor.

Besides the radiative recombination, an electron-hole can recombine nonradiatively which results Auger effect, surface recombination, and phonon emission. In the Auger effect, the energy resulted from the recombination process absorbed by another electron which then dissipates this energy by emitting phonons. Surface recombination may occur in a semiconductor in which there is a continuous distribution of states at the surface of a material. In these materials, when electron and holes are within a diffusion length, they will recombine nonradiatively through a continuum of states [61].

CHAPTER 3

EXPERIMENTAL TECHNIQUES

3.1 Crystal Growth

3.1.1 Preparation of Crucible for Crystal Growth

The most common techniques used to obtain large single crystals are Bridgman-Stockbarger method. The first step of this technique is to choose a suitable growth ampoule, which is called crucible, considering the thermal expansion coefficient and melting point of the crystal to be grown. The most desirable characteristics of a crucible is that its presence should not contaminate the grown material. Therefore, the melting point of the crucible must be considerably higher so that the ampoule material does not practically reacts with the melt and solid phases of the grown crystal. The crucible should have a smaller coefficient of thermal expansion than the grown crystals. It is also desirable that the crucible should have smaller thermal conductivity than the material inside so that the solid-liquid interface isotherm would have more suitable shape to grow better crystals. That is, it helps to obtain a desired thermal field within the solid and melt phases of the material. Considering these facts, for most materials quartz ampoules are chosen as crucible for growth of many crystals having melting temperature well below the melting point of quartz [49].

The crucibles employed had dimensions 10-16 mm internal diameter and 100 mm overall length with 1.5 mm wall thickness. The bottom of the crucibles were conical to encourage spontaneous nucleation and propagation of a single crystal. The crucible materials is usually contaminated by surface dust, grease and inorganic chemicals. These must be removed by appropriate cleaning procedures. Dust and grease are removed by brushing with detergent and hot water. Then the growth ampoules were cleaned chemically using the procedure; 4 hours in a 40 % HNO_3 bath to remove metallic impurities on the surface; cleaning with detergent in an ultrasonic bath to remove the oil on the surface; rinsed with distilled water in ultrasonic cleaner and for an half an hour put in isopropyl alcohol. In order to outgas the remaining impurities inside the crucible, they were heated under vacuum up to 1050 ^oC. After the outgassing process, the ampoules were cleaned again with detergent in an ultrasonic bath, rinsed with distilled water and dried [9, 17, 62].

3.1.2 Material Preparation and Growth Process

Stoichiometric quantities of Gallium and Selenium of $4N_s$ purity were used for synthesis of the compound. The initial charge of 10 to 12 grams of the compound was prepared by the direct synthesis of the elements. After a chemical cleaning treatment of a few minutes in acidic bath, these elements were loaded to a cleaned crucible. The ampoules were evacuated and sealed at a pressure of 10^{-5} torr. Before the growth of GaSe crystals, the constituent elements were reacted to synthesize in the constant temperature zone of a Lindberg laboratory

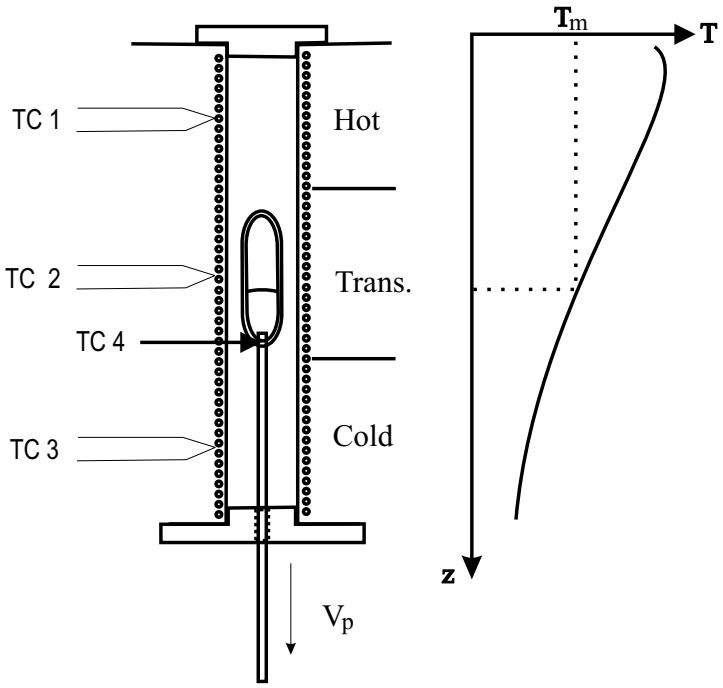

Figure 3.1: Furnace part of the growth system and the ideal temperature distribution along the axis of a cylindrical crucible.

furnace. In order to complete the reaction and homogeneity, the charge was slowly heated up to 1050^oC (over the melting point) and by shaking frequently kept at this temperature for 12 h. The heating process was carefully carried out to avoid the explosion of the loaded ampoule because of the high vapor pressure of the Selenium. After synthesis, the furnace was slowly cooled to the room temperature.

GaSe single crystals used in this study were grown from the melt with a Crystalox MSD-4000 model 3-zone Vertical Bridgman-Stockbarger system in our Crystal Growth Laboratory of Physics Department. Fig. 3.1 shows a schematic diagram of furnace of the growth system with a pointed bottom crucible and the

temperature profile along the furnace. The furnace tube includes three independent heating zones, each 150 mm long, namely the upper zone, adiabatic zone and lower zone. To control the temperature inside the furnace, thermocouples are provided adjacent to the center point of each zone. The temperature of each zones are independently controlled by a Eurotherm Type 902P programmable controllers and kept constant within an accuracy of $\pm 0.1^{o}C$. The top of the furnace is closed using a ceramic plug that are made from coated ceramic fiber insulation. There are five thermocouples in the furnace. Three of them measure the three separate zones temperature and fourth thermocouple placed at the tip of the crucible. There is also a thermocouple for alarm to take care of the overheating, in which case the whole system shuts down automatically with an alarm light. Crucible Translation Unit (CRT), is mounted under the furnace worktop. The loaded crucible is raised or lowered in desired speed by the help of crucible translation unit [63].

Prepared and synthesized growth ampoule was placed to the upper part of the Bridgman furnace. Then, GaSe compound was allowed to crystallize by moving the ampoule from the hot zone toward cold at a temperature gradient of 8^{o}C/cm, with the lowering rates 0.5 and 1.0 mm/h. For a typical run, the temperature gradient inside the furnace along the furnace axis is illustrated in Fig.3.2. The temperature settings of each zone were 1100, 850 and 700 ^{o}C for top zone, middle zone and bottom zone, respectively. As mentioned above, an axial thermocouple was provided to monitor the temperature close to the tip of the crucible. The growth time was nearly 144 hours at a lowering rate of 1 mm/h.

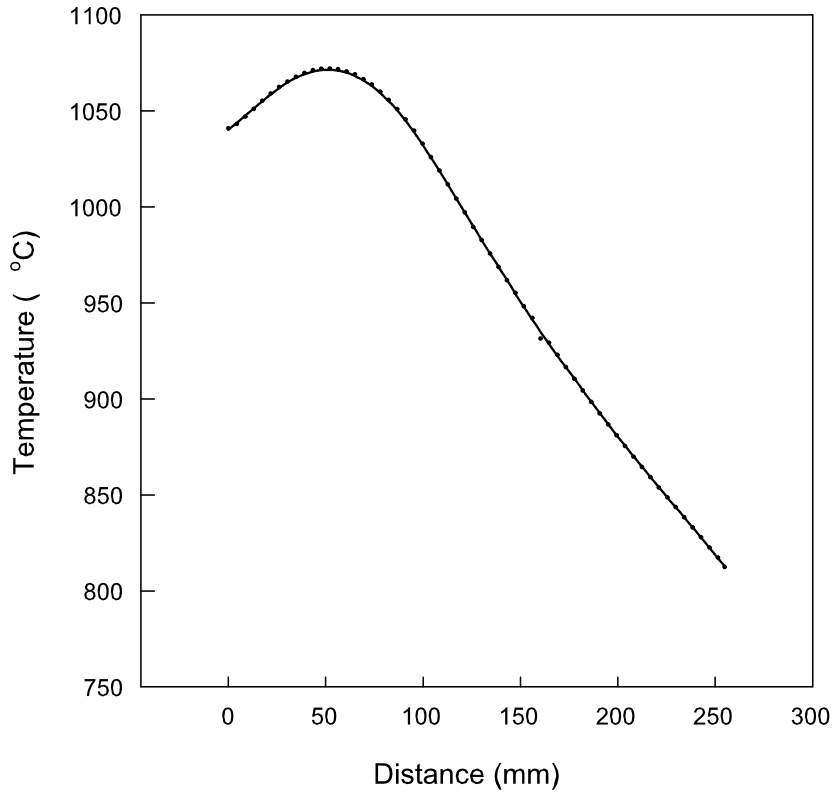

Figure 3.2: A typical temperature profile for growth of compound GaSe using a three-zone B-S furnace.

Surface morphology and stoichiometry of the grown crystal were examined with a JSM 6400 scanning electron microscope equipped with EDAX in the Department of Metallurgical and Materials Engineering in METU and it was observed that the resulting ingot was stoichiometric and the surfaces of the peeled layers were perfect planes.

3.2 Doping and Annealing Processes

Ion implantation is the introduction of ionized atoms onto the surface layer of a solid substrate by bombardment with ions in the keV to Mev energy range. The advantage of this technique is the ability of controlling the concentration

of implanted atoms. The depth distribution of the dopant atoms can also be controlled in the ion implantation technique. The drawback of this technique is that during the implantation, the bombarded substrate may be damaged due to collisions between implanted atoms and lattice atoms. Therefore, in order to remove the lattice damage created during the implantation and to activate the implanted atoms the bombarded substrate should be annealed.

In this study, the implantation was carried out with a Varian Model 200-DF4 type implanter in METU Physics Department. It has a gas box which contains desired impurities. By the ionization of this source, the desired impurity was extracted into the acceleration tube in which the ions were accelerated to a specified kinetic energy. In order to select only the ion species of interest and rejects other species, an analyzer was used. The ion beam was focused to the target and using a scanning system the target was uniformly bombarded.

For the N-implantations, four samples were prepared by cleaving from the ingot along the layers with a razor blade. Typical sample dimensions and the thickness were 4x4 mm^2 and 300 μm respectively. The surface of the samples perpendicular to the c-axis was then bombarded by nitrogen ion beam of about 60 keV and 30 keV to doses of 6×10^{15} ions/cm^2 each. For the Si-implantation, the sample surface perpendicular to the c-axis was bombarded by Si-ion beam of about 100 keV to doses of 1×10^{16} ions/cm^2 at room temperature.

The distribution of the implanted atom was estimated by TRIM (the Transport of Ions in Matter) calculation [64]. These distributions of the implanted impurities showed a gaussian shape through a projected range (R_p) which increase

with increasing implantation energy. By performing implantations at different energies, it is possible to obtain the desired impurity distribution and uniformly doped regions.

After doping, annealing was performed in argon medium for the implanted samples at temperatures 500, 600, 700 and 850 ^oC, for 20 minutes, to possibly remove the damage induced by implantation and also to activate nitrogen related doping centers. As-grown samples were also annealed at these temperatures in order to compare with the results of the implanted and annealed samples.

3.3 Electrical Measurements

The temperature dependent electrical resistivity and Hall-Effect measurements by using the conventional four-point direct current Van der Pauw method [65] were carried out between 100 and 320 K under vacuum in a closed cycle cryogenics helium cryostat using Lake-shore DRC-91C temperature controller. A Keithley 220 programmable constant current source and Keithley 619 electrometer were used in the measurements. A constant magnetic field of 0.97 T was applied parallel to the c-axis using Magnion model FFC-4D magnet during Hall-effect measurements. The schematic representation used in the measurements of electrical conductivity and Hall coefficient is shown in Fig. 3.3.

Electrical contacts for resistivity and Hall effect measurements were made with indium by using Nanotech thermal evaporation system in a vacuum of 10^{-5} torr using suitable masks. Following to the metallic evaporation a slight diffusion was carried out at 200^oC in order to improve the ohmicity of the contacts. Electrodes

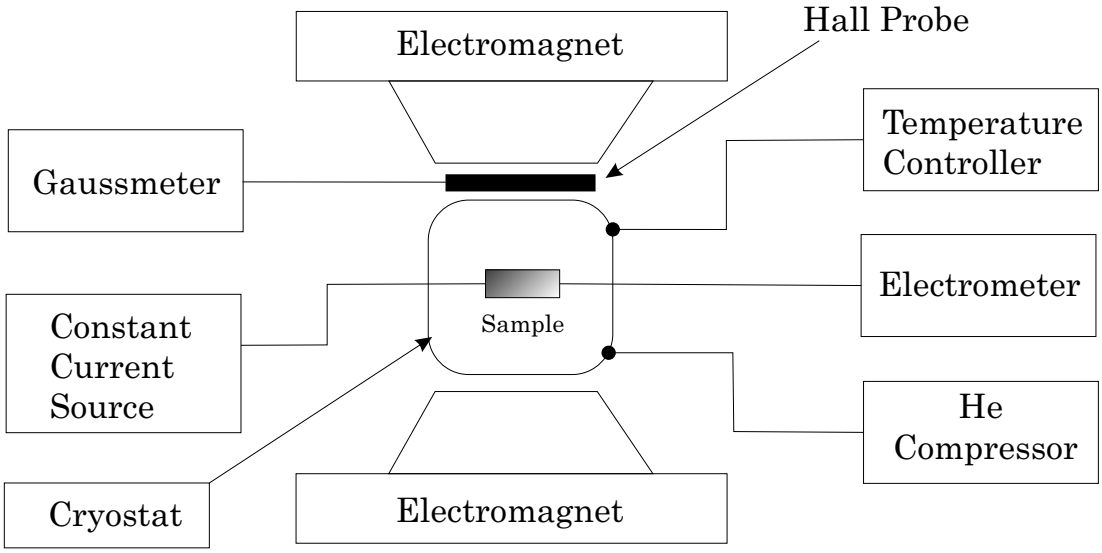

Figure 3.3: Schematic diagram of the Hall system.

were attached to contact region with silver paint. The ohmic behavior of the contacts was confirmed by the linear variations of the I-V characteristic, which is independent of the reversal of the applied bias in working current range. Fig.3.4 shows the sample connections used for taking transport data in the resistivity and Hall effect measurements. For the resistivity calculations, the current through the contacts 3 and 4, the voltage between 1 and 2 are measured by reversing the current. In order to correct for the geometry of the sample, it is necessary to interchange the current and voltage probe for a square specimen. Therefore, a second measurement is taken in which the current through 2 and 3, the voltage between 1 and 4 are recorded. Thus, the resistivity, ρ, is calculated as follow [66];

$$\rho = \frac{\pi t}{ln2}(\frac{R_1 + R_2}{2})f(\frac{R_1}{R_2}) \tag{3.1}$$

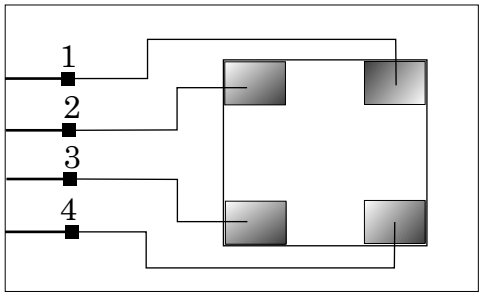

Figure 3.4: An illustration of sample geometry with contacts at each corner.

where t is the sample thickness, R_1 and R_2 are the resistance defined for the first and second positions of the contacts, respectively and $f(\frac{R_1}{R_2})$ is a correction factor depending on the ratio R_1 and R_2 [67].

In order to determine the Hall coefficient, a direct current was passed through contacts between 1 and 3 and the voltage was measured with a high impedance electrometer between contacts 2 and 4. The error which may be introduced by the thermoelectric effects was eliminated by reversing the current, taking a second reading and averaging the pair. It will usually be found that in the absence of a magnetic field there is a voltage between 2 and 4 owing to their alignment being imperfect [54]. This was eliminated by reversing the magnetic field and measuring the potential between 2 and 4 again. Averaging these four readings considerably reduces all random errors. Thus, the Hall coefficient has been calculated by using the relation;

$$R_H = \frac{t}{B}(\Delta R_a + \Delta R_b) \tag{3.2}$$

where B is magnetic field, ΔR_a and ΔR_b is the difference of electrical resistance values with and without the magnetic field defined for the first and second positions of the contacts, respectively and t is thickness of the sample.

3.4 Photoconductivity Measurements

Photoelectric properties of undoped and implanted samples for different illumination intensities, bias voltages and wavelengths were carried out in the temperature range 100-400 K under vacuum of about 10^{-3} Torr. The temperature was stabilized and controlled by a closed cycle helium cryostat and a Lake-shore DRC-91C temperature controller. For intensity and voltage dependencies, 100-Watt Halogen lamp was used and the light was focused onto the sample making sure that the region between two electrodes was fully illuminated. The illumination intensity of the lamp was changed by applying the current through the lamp in between 50 and 100 mA. ILFord 1700 Radiometer was used to determine the illumination intensity values for the lamp at different applied currents. For the light intensity dependency, a constant voltage was applied between the electrodes which was supplied by a Hichkok Model 5056 power supply. The schematic representation of photoconductivity measurements for an illuminated sample was illustrated in Fig.3.5.

Furthermore, for the spectral analysis, an MS 257 monochromator was used and the photocurrent was measured while varying the wavelength from 450 to 800 nm in steps of 5 nm. Light incidence was perpendicular to the crystal layers and applied electric field perpendicular to the c-axis. All measurements were

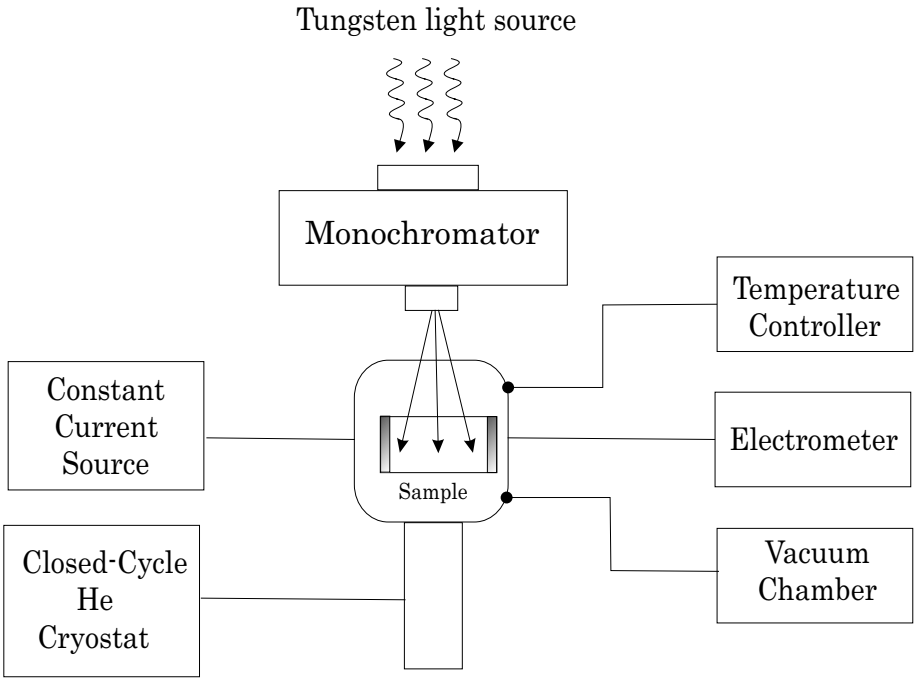

Figure 3.5: Schematic diagram of the photoconductivity measurements system.

taken along the layers and the net photocurrent was obtained by subtracting dark current from the measured photocurrent in the presence of light.

3.5 Photoluminescence Measurements

In this section, a description of the techniques and apparatus that we used for photoluminescence (PL) measurements are summarized. The main purpose of the PL measurement in this study is to investigate the optical properties of the as-grown, as-implanted and implanted and annealed GaSe single crystal.

The experimental setup that we constructed is illustrated in Fig.3.6. The investigated samples were cleaved from the ingot parallel to the layer which was perpendicular to the c-axis. The typical sample dimensions was about of 1 cm^2

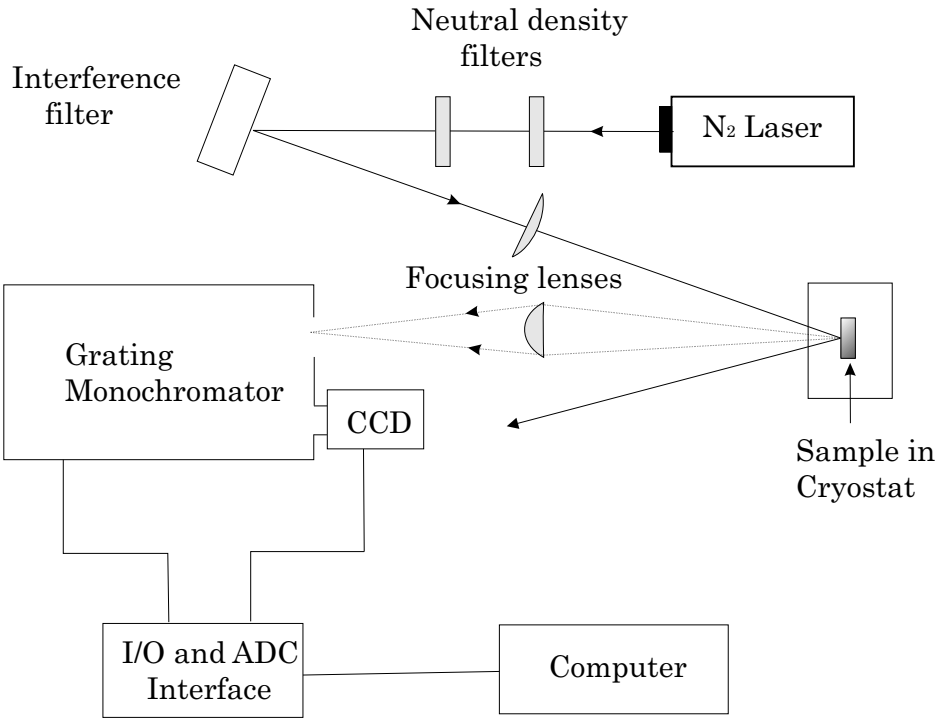

Figure 3.6: Schematic Diagram of the PL System.

area and 0.1 to 0.5 mm of thickness. The crystals were mounted on the cold finger of the cryostat by using thermal compound and excited using the 337 nm line of a Nitrogen pulsed laser. The energy of the photon corresponding to the wavelength 337 nm (3.7 eV) is higher than the band gap of GaSe crystal, satisfying the necessary condition for the PL measurements. The typical average laser excitation intensity was about $7mW/cm^2$. The photons emitted from the samples are collected and analyzed with a monochromator and a CCD detector. The PL signals passes through a grating in the monochromator which selects a wavelength to transmit to the detector. In the PL measurements, a MS 257 with a 1200 groove/mm grating was used. It covers from the visible to the

near infrared ranges with an energy resolution of approximately 1 meV. A CCD (Charge Couple Device) camera was used as detector and the PL output was send to the computer. The best PL spectra resulted from the samples held below room temperature. Therefore, the dependence of the photoluminescence spectra on the temperature was investigated using a cryogenics closed-cycle He cryostat. The temperature was monitored and set from 20 to 300 K with an accuracy $\pm 0.1K$.

CHAPTER 4

RESULTS AND DISCUSSIONS

4.1 Crystal Growth and Structural Analysis

After having completed the growing process, several ingots of GaSe single crystal with no cracks having a diameter of nearly 16 mm and length 20 to 50 mm were obtained successfully. The crystals were optically clear with dark red color and could be cleaved easily. The c-axis of the grown crystals were perpendicular to the ampoule axis for all ingots. X-ray powder measurements were carried out to identify the crystal structure using CuK_α radiation ($\lambda = 1.54059$ A^o) in the scan range of $2\theta = 5^o - 80^o$. 2 θ values were used in TREOR90 which is a trial-and-error program for indexing of unknown patterns. The program contains separate routines for cubic, tetragonal, hexagonal, orthorhombic, monoclinic and triclinic symmetries [68]. The data quality is the most important point to obtain satisfactory results. We applied the program using the data of many well known structures given in JCPDS files and obtained exactly the same structures and the lattice parameters as given in these files [69].

Fig.4.1 shows the XRD patterns of as-grown and annealed at 600 ^{o}C GaSe samples, respectively. As one can see from these figures, the peak positions of the annealed sample agree with the as-grown sample but the intensities of the

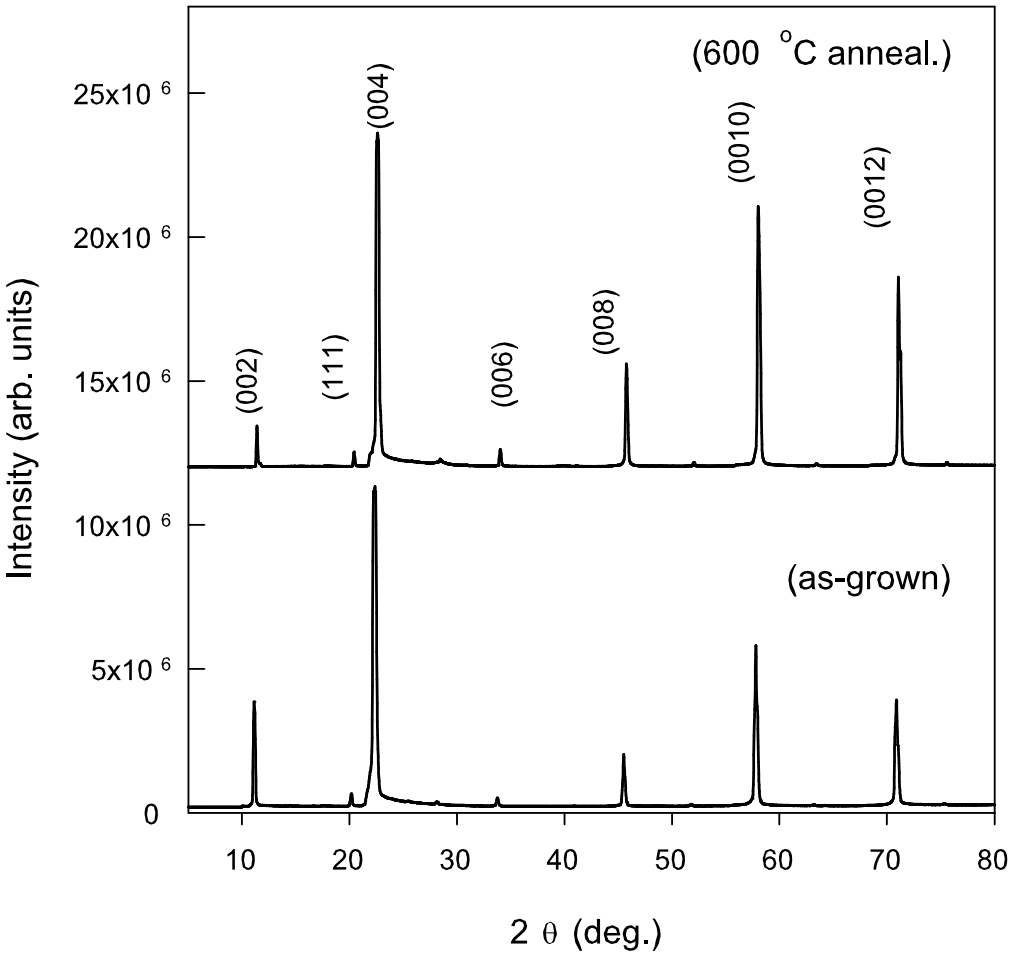

Figure 4.1: X-ray diffraction patterns of as-grown and 600 ^{o}C annealed GaSe samples.

peaks increase with annealing. The orientation of as-grown and annealed samples shows that there is a preferred orientation along the c-axis with the direction of (004) plane. The peak intensity along the direction of this plane is increasing with annealing. This is the indication of increasing crystallinity and decreasing structural disorder with post annealing. The observed reflection peaks of x-ray spectra can be attributed to the typical (00l) lines of the hexagonal structure of GaSe. The c-axis of these samples seems to be preferentially oriented parallel to

the layer plane [70].

In order to identify the structure and reflection indices of the grown crystals, 2θ values obtained from the XRD measurements were used in TREOR90. The structure of the Bridgman grown GaSe crystals were reported in hexagonal or rhombohedral modifications with lattice parameters a=3.75A^o and c=15.95A^o [3, 71]. Although our peak positions resemble to those of the diffraction results reported in literature, we could not obtain the hexagonal structure with proposed lattice parameters from the TREOR90 calculations. To compare our results with literature and also to check the accuracy of the indexing program, we applied the TREOR90 program to the θ values, which were given by Anis [3] for GaSe. We could not obtain the hexagonal structure as they proposed, without changing D1 and D2 parameters, which are the parameters for the indexing accuracy of the program. The program uses the default values D1=0.0002 and D2=0.0004 unless new values are assigned for them. Assigning larger values for D1 and D2 reduces the indexing accuracy of the program. Setting these parameters as D1=0.0004 and D2=0.0008, the proposed structure and lattice parameters given by Anis [3] were obtained. For these values of D1 and D2, another possible solution was also obtained as orthorhombic.

For our as-grown GaSe samples, both using the new D1 and D2 values given above and the default more accurate values of the program resulted in the same tetragonal structure with lattice parameters a=6.47A^o and c=15.93A^o. Another possible result obtained from the TREOR90 program was hexagonal structure with lattice parameters a=6.11A^o and c=7.97A^o. For the annealed sample the

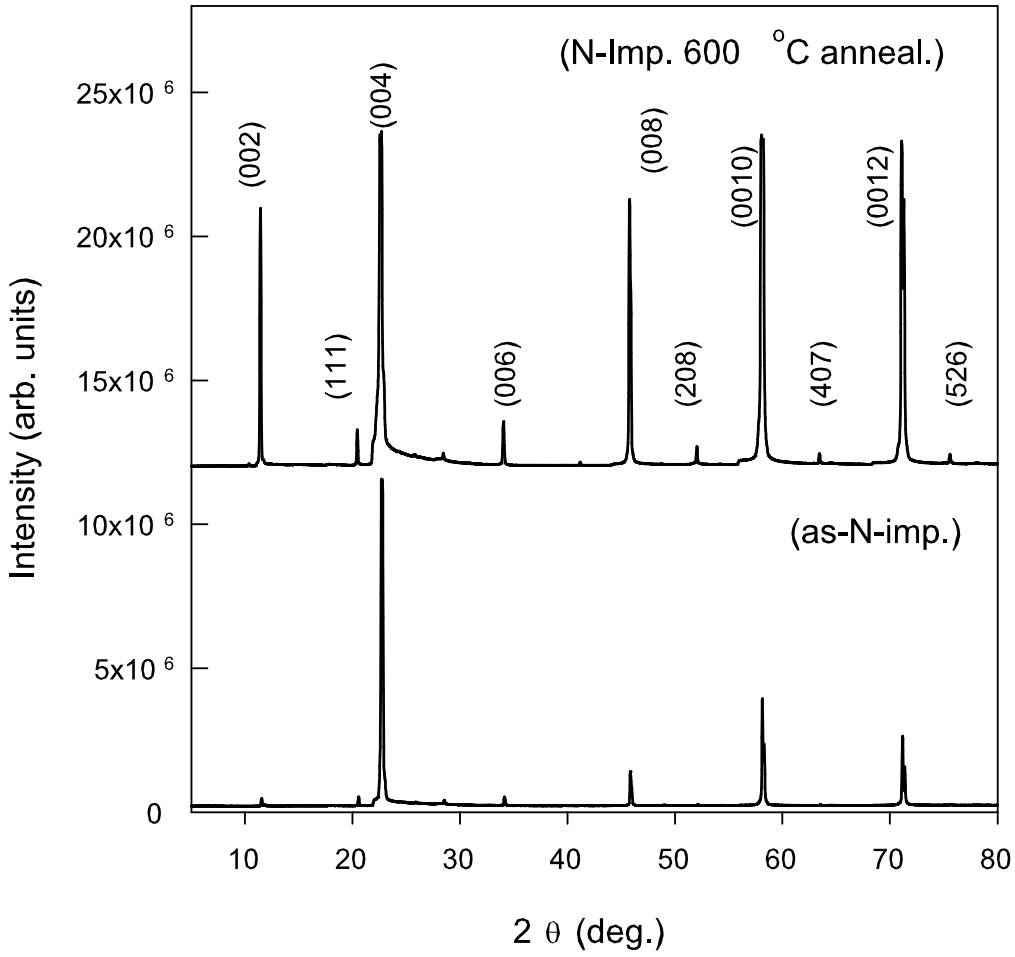

Figure 4.2: X-ray diffraction patterns of N-implanted and 600 ^{o}C annealed GaSe sample.

structure was hexagonal with lattice parameters $a = 6.16A^o$ and $c = 23.29A^o$. The relative intensities, crystal structure and lattice parameters of the observed reflections from the as-grown GaSe sample are given in Table 4.1. The Miller indices for the intense peak are in agreement with literature given for as-grown GaSe single crystal [3, 71]. The differences between our result and Anis's may steam from the impurity in GaSe or growth conditions. The accuracy of TREOR90 is another parameter, which may be effective in obtaining the results. However,

Table 4.1: The TREOR90 outputs from the X-ray diffraction measurements of as-grown GaSe sample

Structure:Tetragonal Unit cell volume=668.05 $\AA^3$ a=6.47 $\AA$ b=6.47 $\AA$ c=15.93 $\AA$	parameters			
h k l	2 θ obs.	2 θ cal.	d	Intens.
0 0 2	11.10	11.09	7.96	32
1 1 1	20.12	20.16	4.41	4
0 0 4	22.28	22.29	3.98	100
2 0 1	28.14	28.10	3.17	3
0 0 6	33.80	33.72	2.65	6
2 2 2	40.94	40.99	2.20	1
0 0 8	45.52	45.50	1.99	16
3 0 5	51.08	51.07	1.78	1
0 0 10	57.82	57.81	1.59	50
- - -	63.22	-	1.46	1
0 0 12	70.88	70.91	1.33	33
3 2 9	75.34	75.32	1.26	1

we should mention that the data and the structure of GaSe is inadequate and unreliable as stated in JCPDS files [69]. Therefore, we believe that a detailed experimental and theoretical analysis should be carried out to clarify the structure and the phases of GaSe.

Fig.4.2 shows the XRD patterns of N-implanted and N-implanted and annealed at 600 ^{o}C samples, respectively. We found that the structure was hexagonal for N-implanted and N-implanted and annealed samples. The values of the lattice parameters were found to be a=9.33 A^o, c=15.27 A^o and a=15.20 A^o, c=4.60 A^o, respectively for as-implanted and N-implanted and annealed at 600 ^{o}C samples. As we mentioned above all these results must be repeated using the data for different samples from different ingots and using different programs in

order to reach meaningful conclusions about the structure of GaSe. Note that x-ray measurements that we carried out for a sample taken from the laboratories of Azerbaijan Academy of Science gave similar results.

4.2 Electrical Conductivity

In order to deduce the conduction mechanisms and identify the impurity levels, the temperature dependence of dark electrical conductivity measurements perpendicular and along to the c-axis were carried out in the temperature regions of 100-450 K. Electrical contacts for resistivity and Hall effect measurements were made as described in Chapter 3. The ohmic behavior of the contacts were confirmed by the linear variations of the I-V characteristic, which is independent of the reversal of the applied bias in working current range.

All the as-grown GaSe samples studied here exhibited p-type conduction verified by hot probe techniques and Hall effect. The room temperature resistivity values of undoped (A0) samples along and parallel to the c-axis were found to be around 10^7 Ω-cm, agreeing with the given values in the literature for GaSe grown by Bridgman [22, 72]. Fig.4.3 shows the temperature-dependence conductivity of the GaSe single crystal perpendicular and parallel to the c-axis. In the inset, the conductivity anisotropy was plotted as a function of inverse temperature. In general, the conductivity parallel to the layers decreases exponentially at higher rates with decreasing ambient temperature above 200 K but below which at a slower rates. The electrical conductivity parallel to the c-axis shows similar behavior with the conductivity variations parallel to the layers up to the temperature 320

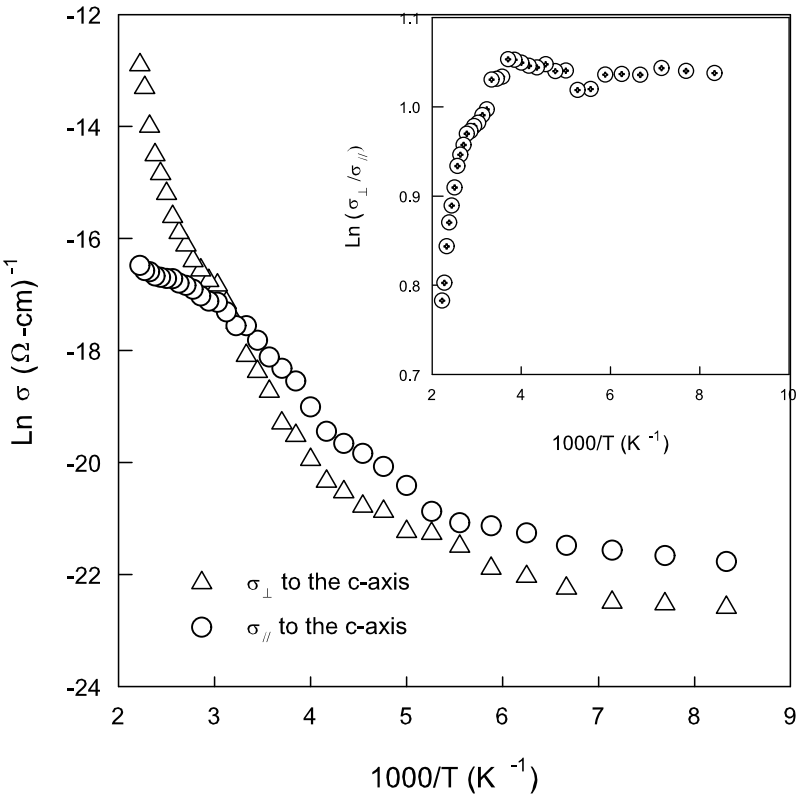

Figure 4.3: The temperature dependent electrical conductivity of as-grown GaSe sample along (○) and perpendicular (△) to the c-axis.

K. Above this temperature, the temperature dependence of the conductivity is weak. The reason of this behavior is probably related to the total ionization of the acceptors. In the studied temperature range, the temperature dependent data was analyzed by using the conductivity expression;

$$\sigma = \frac{\sigma_o}{\sqrt{T}} e^{\frac{-E_\sigma}{kT}} \tag{4.1}$$

where σ_o is the pre-exponential factor, E_σ is the conductivity activation energy and k is Boltzman constant. As seen in Fig.4.3 $\ln(\sigma)$ versus T^{-1} plots show three linear regions with different activation energies (along layers). The depth of the

impurity centers calculated from the electrical conductivity measurements are 44, 243 and 414 meV in the temperature ranges 120-220, 230-320 and 330-450 K, respectively. In general, the first two levels are in agreement with the given values in the literature for GaSe grown by Bridgman method, and are generally attributed to intrinsic acceptor centers, generated by structural defects [22, 72]. These acceptor centers can be explained with the gallium vacancy or the chemical impurity resulted during the growth process. In the high temperature region (in between 330-450 K), the calculated activation energy (414 meV) is larger than the value 310 meV which was observed in crystals grown in silica ampoules without carbon coating [22]. Therefore, this deep level can be explained by the chemical interaction between silica and GaSe.

We also carried out conductivity measurements along the c-axis in the same temperature interval. We observed that the conductivity shows an exponential dependence with the temperature variations up to a critical temperature and above this temperature, it becomes less sensitive to the temperature. The activation energies calculated from the conductivity relation were 68 and 140 meV in the temperature ranges 120-220, and 230-320 K, respectively. In the high temperature region (in between 330-450 K), the activation energy was found to be around 18 meV. As one can deduce from the temperature dependent conductivity results, the values of activation energies in both directions with respect to the c-axis imply that different conduction mechanisms dominate the conduction of the carriers in each direction at different temperature interval, that is the consequence of anisotropic bonding within and between the layers, which result

in different stacking faults and structural disorder in these samples. The relation between the conductivity anisotropy and temperature can be described as $\sigma_{\perp}/\sigma_{//} \sim exp(\triangle E/kT)$, where $\triangle E$ is the barrier hight between the layers. It can be seen from the inset of the Fig.4.3, there is a temperature dependence of conductivity above the high temperature region. The barrier hight $\triangle E/kT$ was found as 20 meV from the conductivity ratio. Such a temperature dependence was observed by Schmid et al. and they found this barrier hight as 30 meV [24]. In contrast to these results, Augelli et al. reported that $\sigma_{\perp}/\sigma_{//}$ is temperature independent [23].

To decrease the resistivity and see the effect of doping on the GaSe crystals, doping process were carried out using the ion implantation technique, the grown crystals were bombarded by N- and Si-atoms. The ion profiles obtained from N-implanted GaSe by TRIM calculations (6×10^{15} ions/cm^2, 30-60 keV) are shown in Fig4.4. After doping, as mentioned in Chapter 3 the annealing was performed in argon medium for the three of the samples at various temperatures, for 20 minutes, to possibly remove the damage induced by implantation and also to activate N and Si related doping centers. In order to determine the doping effect on conduction, the temperature-dependent electrical conductivity measurements were carried out for N- and Si-implanted and annealed samples.

All the implanted GaSe samples studied here exhibited p-type conduction verified by hot probe techniques and Hall effect measurements. Although the room temperature resistivity values of undoped (A0) sample were found to be around 10^7 Ω-cm, the resistivities at room temperature for N-implanted (A1)

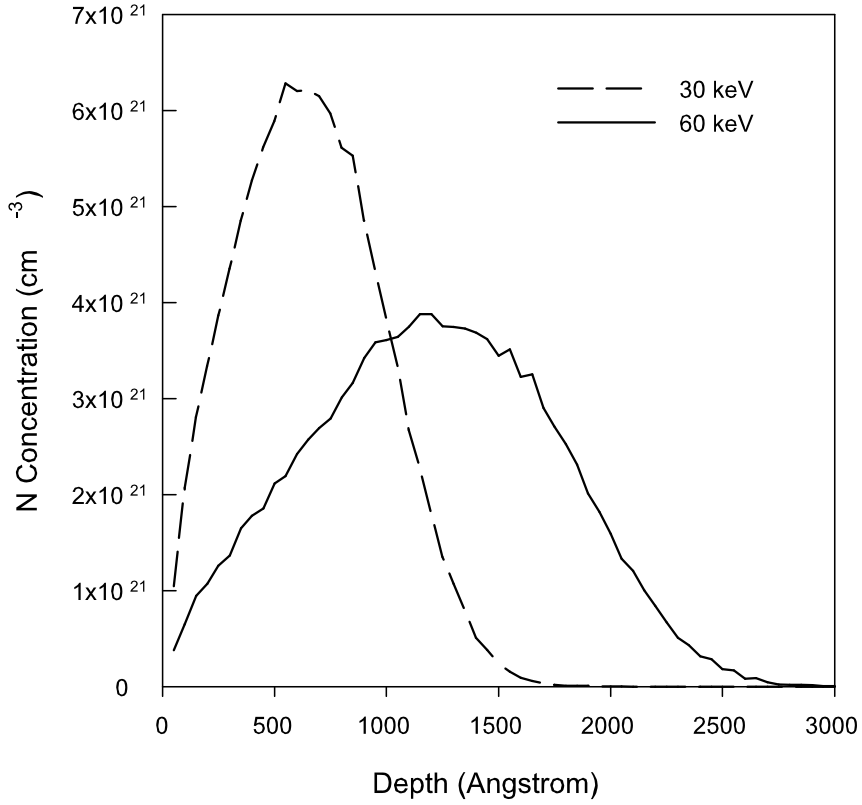

Figure 4.4: Distributions of N-implanted impurities in GaSe obtained by TRIM calculations (for a dose of 6×10^{15} ions/cm^2).

and annealed samples at 500 ^{O}C (A2) and 700 ^{O}C (A3) were reduced down to the values 9×10^{5} Ω-cm, 3.6×10^{4} Ω-cm and 5.6×10^{3} Ω-cm, respectively. As seen from Table 4.1, doping with nitrogen by ion implantation reduced the resistivity of GaSe single crystal three orders of magnitudes, and this is consistent with what was observed by chemical doping techniques [45]. The temperature dependent conductivity of N-implanted samples were measured in the range of 100-320 K. Fig.4.5 shows the temperature variations of the four samples, which are as-grown (A0), N-implanted (A1), N-implanted and annealed at 500 ^{o}C (A2)

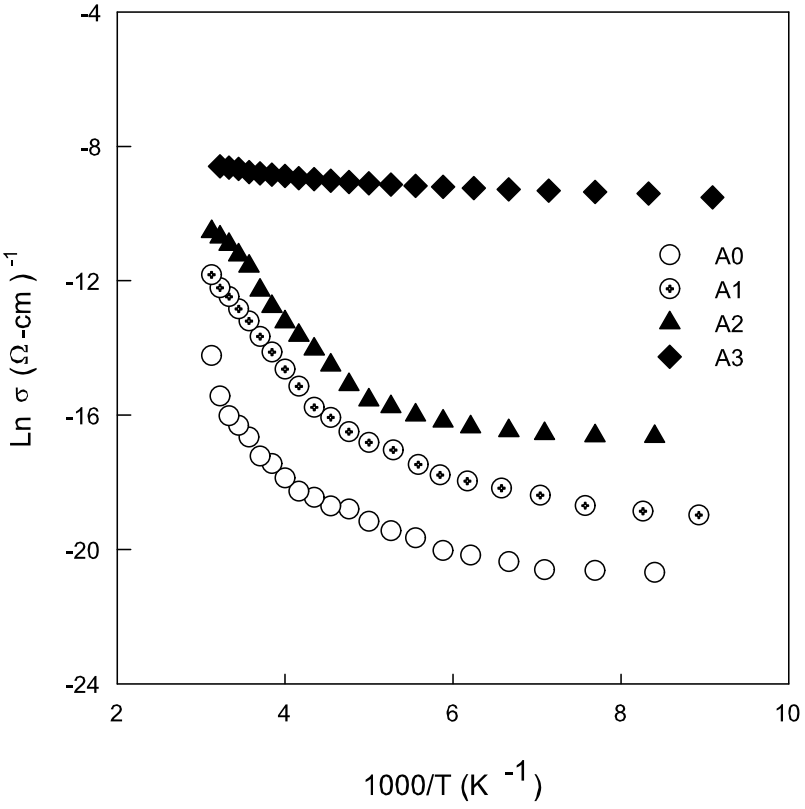

Figure 4.5: The temperature dependent conductivity of as-grown (A0), N-implanted (A1) and annealed at 500 ^{o}C (A2) and at 700 ^{o}C (A3) samples.

and 700 ^oC (A3). The temperature dependent conductivity measurements of the sample annealed at 850 ^oC did not yield consequential results, probably due to loss of crystallinity and structural deformations of the sample at high annealing temperatures.

In general, the conductivity decreases exponentially at higher rates with decreasing ambient temperature above 190 K but below which at a slower rates. The variation of the temperature dependent conductivity decreases with increasing annealing temperature, and becomes less sensitive to the temperature for the

sample annealed at 700 ^oC. In the studied temperature range, the temperature dependent data was analyzed by using the conductivity expression Eqn. 4.1. As seen in Fig.4.5 lnσ versus T^{-1} plots show two linear regions with different activation energies. In the high temperature region (in between 200-320 K), the activation energies of A0, A1 and A2 lie in the range of 252-269 meV. In the low temperature range (in between 100-190 K), activation energies of these samples vary in the range of 33-66 meV. However, sample implanted and annealed at 700^oC (A3) has quite low activation energies with the values 26 and 8 meV, in the high and low temperature regions, respectively. The slowly varying conductivity of A3 with absolute temperature indicates that high annealing temperature of nitrogen implanted GaSe crystals increases the structural deformations within the crystal as will be discussed below.

In addition to the nitrogen implantation, the samples were also bombarded in the direction parallel to c-axis by Si-ion beam of about 100 keV to doses of 1×10^{16} ions/cm^2 at room temperature. The effects of Si-implantation with annealing at 500 and 600 ^oC on the electrical properties have been studied by carrying out the temperature dependent conductivity measurements. The temperature dependent electrical conductivity measurements for all samples were carried out in the temperature range of 100-320 K. In the conductivity calculations of the implanted samples, the thickness of the layer was taken as 3 μm, since the distribution of implanted Si atoms was accepted to be homogeneous from the surface to 3 μm depth as estimated from TRIM calculation [47, 64]. The calculated values of

dark conductivities of four samples were plotted as a function of inverse temperature in Fig.4.6, in which B0, B1, B2 and B3 represent as-grown, Si-implanted, Si-implanted and annealed at 500, and 600 ^oC samples, respectively. As seen from Fig.4.6 and Table 1, the room temperature resistivity values of as-grown samples were found to be around 10^7 (Ω-cm). However, the resistivity values of Si-implanted and annealed samples at 500 and 600 ^oC following to the implantation decreased to 2.9×10^5 , 3.6×10^4 and 7.7×10^2 (Ω-cm), respectively. We also annealed one of the as-grown samples at 500 ^oC and no appreciable changes were observed in the room temperature and temperature dependent conductivity values as compared to the as-grown samples. The rise of room temperature conductivity values shows that the Si-implantation into GaSe single crystals together with the annealing has a pronounced effect on the conductivity values. Therefore, we attributed this effect to the Si-induced modification and doping of the semiconductor [73].

The variations of the dark conductivity with temperature show exponential behavior for all the samples, with different activation energy and yield two temperature regions in the studied temperature range. At high temperature region between 200 and 320 K, the calculated values of activation energies from the slopes of the plots are around 243, 158, 147 and 37 meV for the samples B0, B1, B2 and B3, respectively. At the low temperature region between 100 and 200 K, the activation energies of the same samples are found to be around 74, 47, 46 and 14 meV. As it can be seen from these values of activation energies and Fig.4.6,

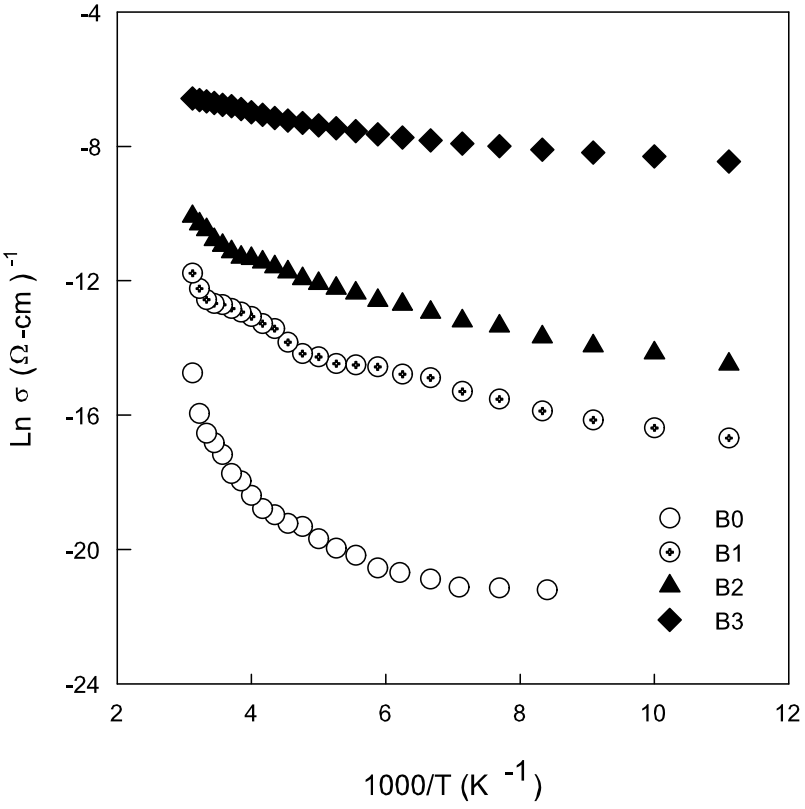

Figure 4.6: The temperature dependent conductivity of as-grown (B0), Si-implanted (B1) and annealed at 500 ^{o}C (B2) and at 600 ^{o}C (B3) samples.

the annealing of the implanted samples increases the conductivity and weakens the temperature dependence. At 600 ^oC and above annealing temperature, the absence of exponential dependence may be attributed defective degenerate structure produced by diffusion of the implanted Si-atoms. The similar behavior with approximately the same conductivity activation energies was observed in our N-implanted GaSe measurements [5], in which the slowly varying conductivity with absolute temperature at high annealing temperature (around 700 ^oC) was attributed to the result of increasing structural deformation and stacking fault within the crystal and due to shallow nature of N-induced defects with increasing

temperature. Almost the same activation energies were observed around 0.14 and 0.04 eV from the measurements of Hall effect and deep-level transient spectroscopy made on Cu doped GaSe by Shigetomi et al. They stated that these levels to be acceptor levels located above valance band, which were associated with defects or defect complexes produced by doping of Cu [38]. One can see from Table 4.4 that upon annealing there is a large decrease in the conductivity activation energies compared to as-grown and implanted samples. This decrease can be related with the implantation induced defects and it is associated with the fact that as the annealing temperature increases Si-related states become electrically active.

The weak temperature dependence of the dark conductivity with small activation energy at low temperature region shows that the conduction mechanism is possibly dominated by Mott's hopping instead of thermal excitation [55]. Therefore, in the studied temperature region, the conductivity might be written as;

$$\sigma = \sigma_b + \sigma_h = \sigma_0 exp(\triangle E/kT) + \sigma_{h0} exp[-(T_0/T)^{1/4}] \tag{4.2}$$

where, $T_0 = 16\gamma^3/kN(E_f)$ is the degree of disorder, $\sigma_{h0} = e^2R^2\nu_{ph}N(E_f)$ is the pre-exponential constant for hopping conduction, k is the Boltzman constant, $N(E_f)$ is the density of localized states at the Fermi level and ν_{ph} is the phonon frequency (10^{12} Hz, typically). In the low temperature region, $Ln\sigma$ was plotted as a function of $T^{-1/4}$ in Fig.4.7, for the samples B1, B2 and B3. From the slopes and the intercepts of these linear plots, Mott's parameters, i.e. T_o, $N(E_f)$, the decay constant γ, average hopping range (R) and average hopping energy (W)

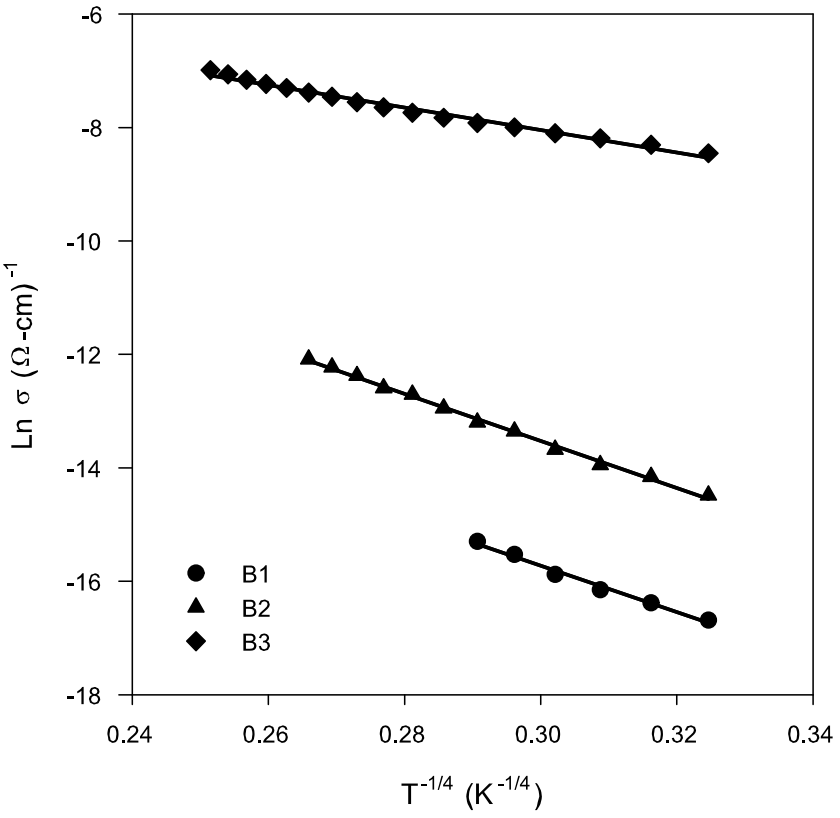

Figure 4.7: Ln σ-$T^{-1/4}$ variations for Si-implanted (B1) and annealed at 500 ^{o}C (B2) and at 600 ^{o}C (B3) samples.

were calculated using the expressions given by Paul and Mitra [74] and listed in Table 4.2. The calculated values of the product γR and W satisfy Mott's requirements ($\gamma R > 1, W > kT$). Thus, at low temperature region, variable range hopping mechanism provides the conduction of carrier in these samples. Similar conduction mechanism following implantation was reported for TiO_2 [75]. As seen in Fig.4.7, as the annealing temperature increases, the upper limit of hopping mechanism moves towards the higher temperatures. This extension is also accompanied by comparatively small increase in the conductivity toward high

Table 4.2: Summary of the Mott's parameters and activation energies of Si-implanted GaSe.

Sample No	B0	B1	B2	*B*3
$\rho_{300K}(\Omega - cm)$	$9.0x10^6$	$2.9x10^5$	$3.6x10^4$	$7.7x10^2$
$E_\sigma(meV) T > 200K$	243	158	147	37
$E_\sigma(meV) T < 200K$	74	47	46	14
$T_o(K)$	–	$1.6x10^7$	$3.2x10^6$	$1.6x10^5$
$\alpha(cm^{-1})$	–	$1.1x10^5$	$4.9x10^4$	$3.1x10^3$
$R(cm)$	–	$6.1x10^{-5}$	$9.2x10^{-5}$	$6.6x10^{-4}$
$W(meV)$	–	54	40	20
αR	–	7.3	4.8	2.2
$N(E_f)(cm^{-3}eV^{-1})$	–	$2.0x10^{13}$	$7.9x10^{12}$	$4.1x10^{10}$

temperature region. This behavior is related to the distribution of Si-induced defect states around the Fermi level which becomes electrically active so as to participate in hopping process.

4.3 Carrier Concentration and Hall Mobility

The temperature dependent Hall mobility of the as-grown, N-and Si- implanted GaSe samples were measured by using van der Pauw method [65]. The Hall coefficient R_H was calculated by using the expression;

$$R_H = \frac{t}{B}(\Delta R_a + \Delta R_b), \tag{4.3}$$

where B is magnetic field, ΔR_a and ΔR_b is the difference of electrical resistance values with and without the magnetic field, respectively and t is thickness. The free carrier (hole) concentration was determined from the Hall coefficient by using the relation $p = r/qR_H$, with the Hall factor (r) of unity, where q is the electronic

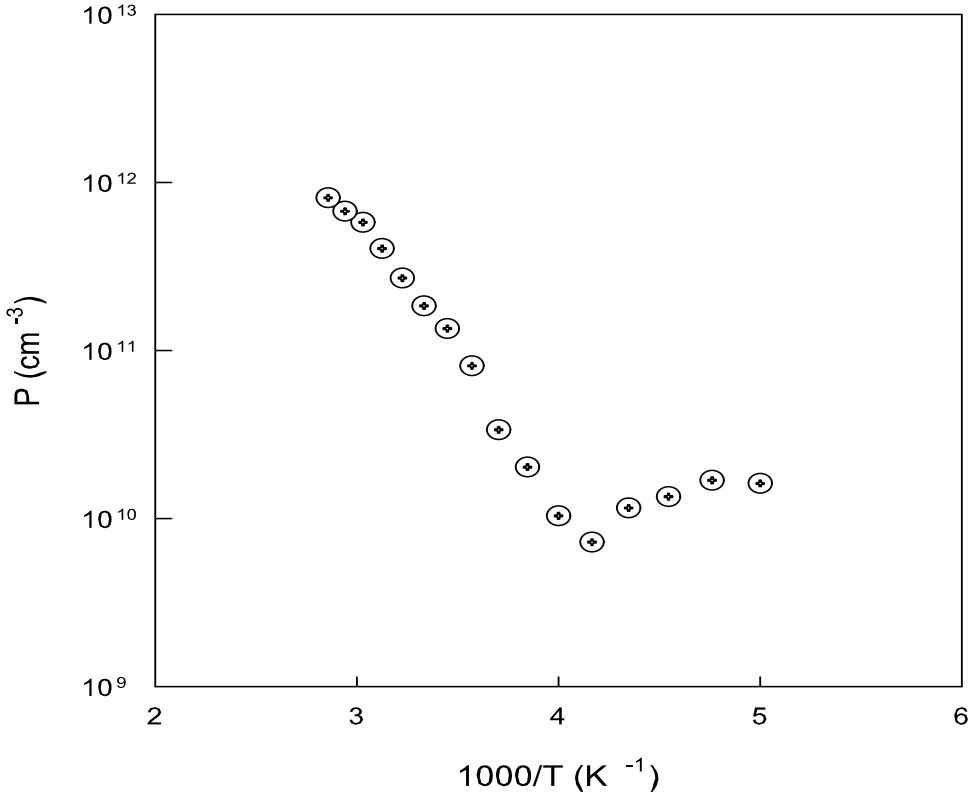

Figure 4.8: The temperature dependent hole density of as-grown GaSe samples.

charge. Fig.4.8 shows the hole concentration (p) as a function of reciprocal temperature for as-grown GaSe single crystal. Hole concentrations (p) for as-grown sample decreases with decreasing temperature in between 350-240 K. Below this temperature, no significant variation with the temperature was observed.

In order to determine the effect of N- and Si-implantation on carrier concentration, the Hall measurements were carried out on implanted and annealed samples. Using the estimated distribution of the implanted N- and Si-atoms by TRIM calculation, it was obtained that the implanted region has a uniform N- and Si- concentration with a thickness 3 μm [64]. This value was used in Eqn.4.3

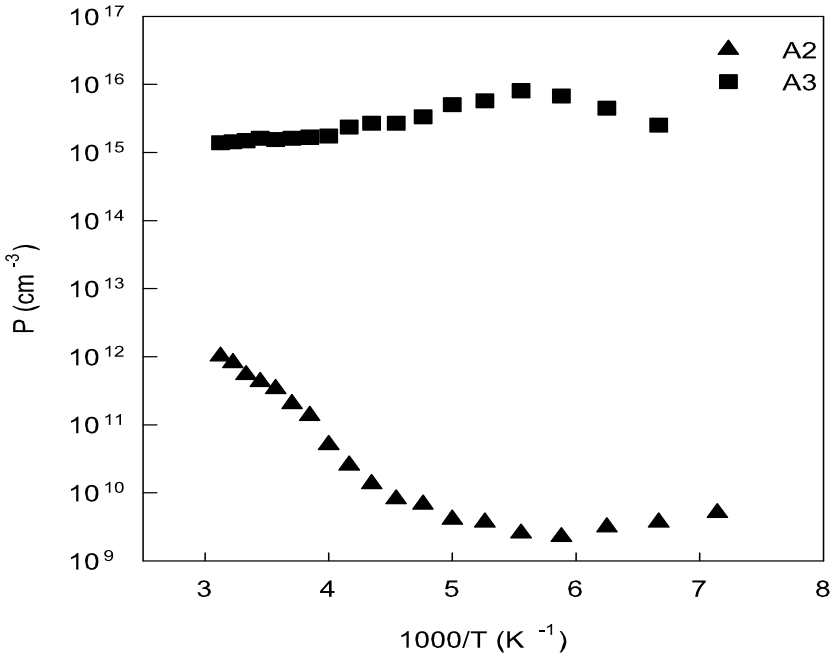

Figure 4.9: The temperature dependent hole density of N-implanted and annealed at 500 ^{o}C (A2) and at 700 ^{o}C (A3) samples.

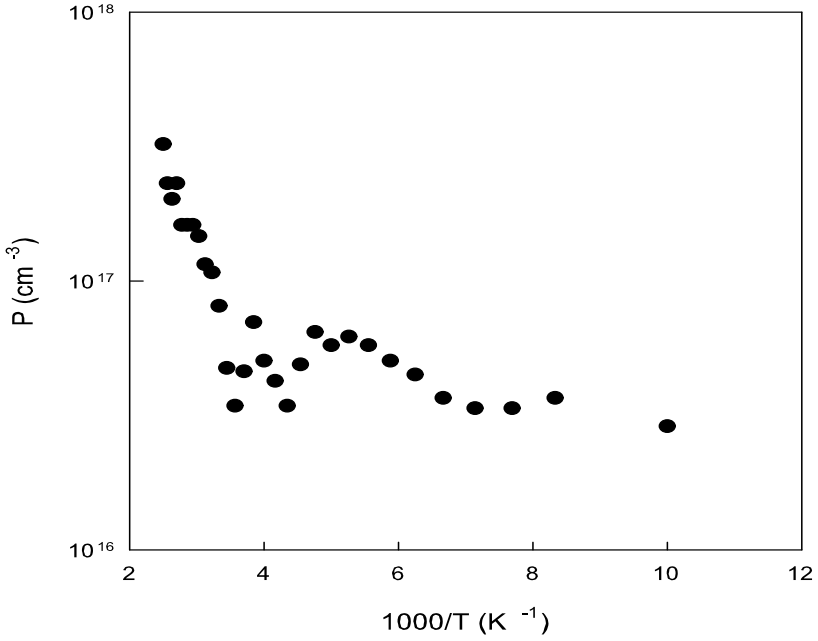

Figure 4.10: The temperature dependent hole density of Si-implanted and annealed at 500 ^{o}C (B2) sample.

to find the Hall coefficient. Fig.4.9 shows the hole concentration (p) as a function of reciprocal temperature for two different annealed samples A2 and A3. Hole concentrations for A2 drastically decrease with decreasing temperature. For A3, the hole concentration increases to the order of 10^{16} cm^{-3} but no significant variation with the temperature was observed. Fig.4.10 shows the behavior of hole concentration as a function of reciprocal temperature in Si-implanted and annealed at 500 ^{o}C GaSe. From this figure we see that post annealing after the Si-implantation leads to an effective increasing of hole concentration. The hole concentration decreases slowly up to room temperature and below this temperature no temperature variation was observed.

We consider that as-grown, N- and Si-implanted and annealed samples behave as partly compensated p-type semiconductor. Therefore, in order to obtain information about impurity concentration and acceptor ionization energy in these samples, temperature dependence of the carrier concentration was analyzed using the single donor-single acceptor model, assuming the usual three-dimensional expression for the density of states [59]. According to this model, the temperature dependence of carrier concentration (p) is given in Eq.2.44 with $N_v = 4.82\times10^{15}$ $T^{3/2}$ $(m_h^*/m_o)^{3/2}$ (cm^{-3}). In this equation, E_a is the ionization energy of the acceptor level, k is the Boltzman constant, N_a and N_d are the concentrations of the acceptor and donor, respectively. The hole effective mass ratio of m_h^*/m_o= 0.5 and the degeneracy factor $\beta = 2$ were used in the equation for p-GaSe [42]. To calculate the parameters N_a, N_d and E_a from the experimental p values, we have fitted Eq.2.44 to the measured hole concentration. The logarithm of the left-hand

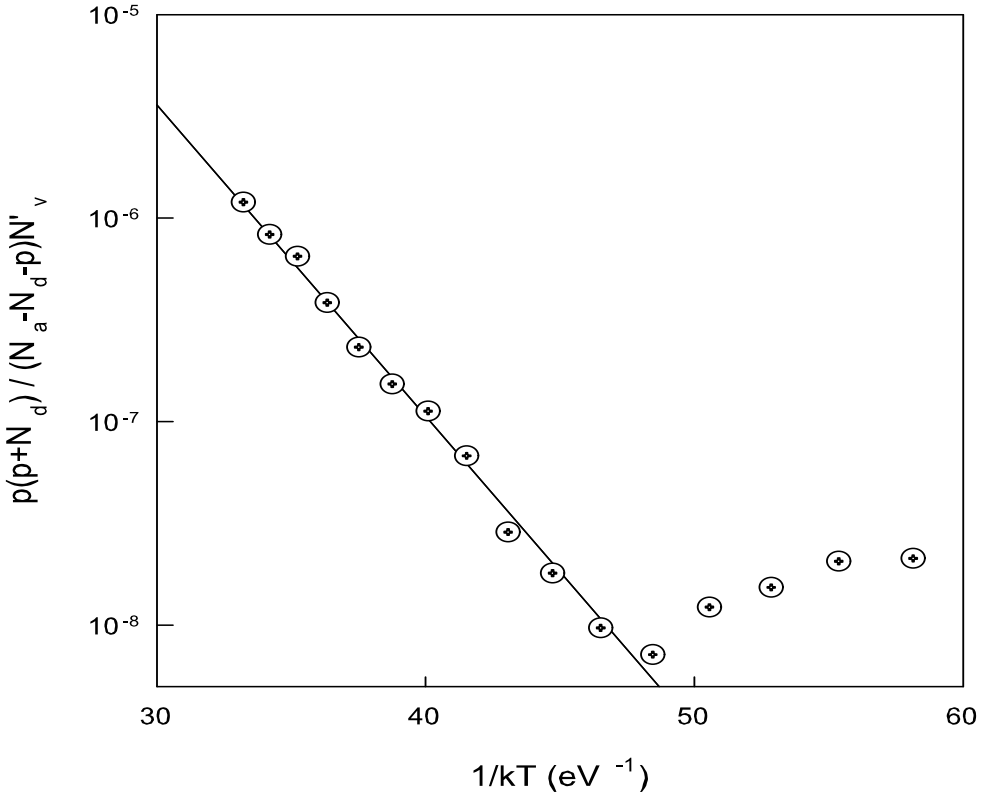

Figure 4.11: Single donor-Single acceptor model analysis of the experimental data for as-grown GaSe sample.

side of Eq.2.44 versus $1/kT$ was plotted with N_a and N_d as fitting parameters. This plot results in a straight line only for the correct values of N_a and N_d.

Fig.4.11 represents the best fits obtained for the as-grown sample shown in Fig.4.8. Acceptor activation energy for as-grown sample was determined as 350 meV from the slope and the concentrations were found to be 1.0×10^{14} and $8.6 \times 10^{12} cm^{-3}$ for N_a and N_d, respectively. The values of N_a and N_d were reported about 10^{16} and 10^{12} cm^{-3}, respectively with an 230 meV activation energy for undoped GaSe crystals [23, 22]. The obtained activation energy from the SDSA analyze is greater than those previously reported, but such a deep levels

were observed in crystals which were grown by uncoated crucibles. Therefore, this deep level may be associated with chemical impurities resulting from the interaction between crucible material and GaSe [22].

Fig.4.12 and 4.13 show the Single donor-Single acceptor model analysis of the experimental data reported in Fig.4.9 and 4.10 for the N- and Si-implanted samples. The values of E_a, N_a and N_d obtained from this fitting procedure are also reported in Table 4.3. Acceptor activation energy for N-implanted sample was determined as 450 meV from the slope and the concentrations were found to be 1.0×10^{13} and $3.5 \times 10^{10} cm^{-3}$ for N_a and N_d, respectively. The calculated values of E_a=450 meV from the slope of the straight line suggests that there is deep acceptor energy level above the valance band originating from the variation of N-induced defects upon annealing. This value is slightly larger than the value (350 meV) obtained for chemically doped samples by Sanchez at al [45]. Nitrogen implantation to GaSe crystals together with annealing results in stacking faults within the crystals where they act probably as deep acceptor level, like in neutron-transmutation doped InSe crystals, where stacking faults act as deep donor levels [76].

The acceptor and donor concentrations were obtained as 8.4×10^{18} and 3.9×10^{17} cm^{-3} for N_a and N_d, respectively and acceptor ionization energy was determined as 150 meV, from the analysis for the Si-implanted and annealed at 500 ^{o} C sample. As it is seen, while hole concentration N_a and N_d increase with Si-implantation, the ionization energy was decreased. Such a behavior may be associated with the compensation of the previously presented levels by the Si ions and

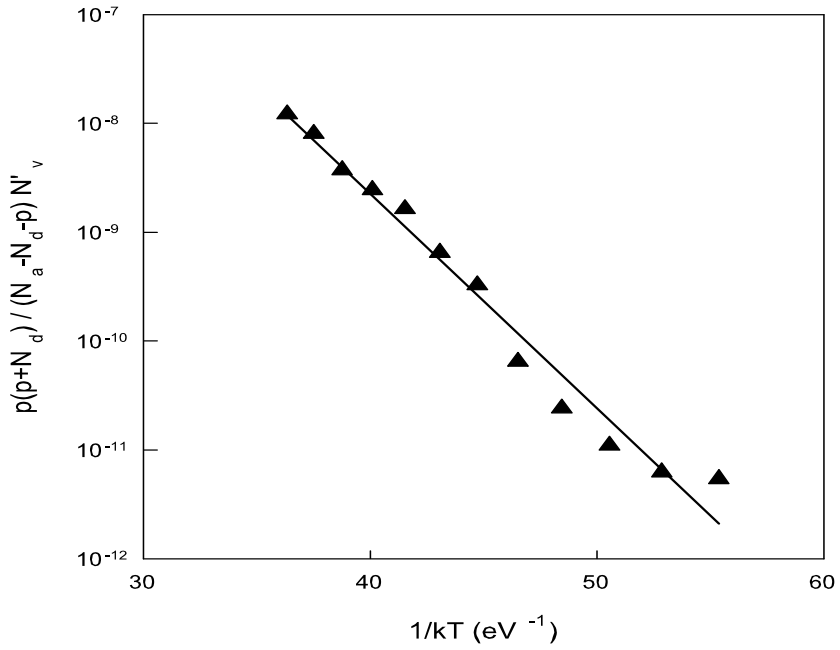

Figure 4.12: Single donor-Single acceptor model analysis of the experimental data for N-implanted and annealed at 500 ^{o}C (A2) sample.

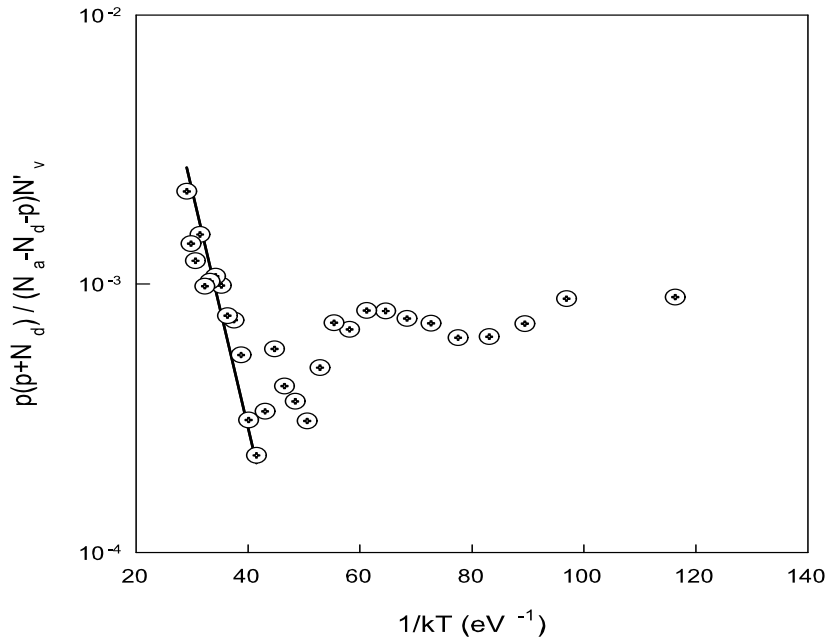

Figure 4.13: Single donor-Single acceptor model analysis of the experimental data for Si-implanted and annealed at 500 ^{o}C (B2) sample.

Table 4.3: The parameters obtained from the single donor-single acceptor model analysis shown in Fig.4.11, 4.12 and 4.13

Sample	$N_a(cm^{-3})$	$N_d(cm^{-3})$	$N_a - N_d(cm^{-3})$	$E_a(meV)$
GaSe(A0)	$1.0x10^{14}$	$8.6x10^{12}$	$9.1x10^{13}$	350
GaSe(A2)	$1.0x10^{13}$	$3.5x10^{10}$	$1.1x10^{12}$	450
GaSe(B2)	$8.4x10^{18}$	$3.9x10^{17}$	$8.0x10^{18}$	150

introducing new impurity levels during implantation process. Similar behavior were reported for GaTe crystals in which Cu doping caused the compensation of existing levels and occurred new impurity levels [77].

By using the experimental R_H and conductivity results, mobility values were determined from $\mu_H = \rho R_H$. Obtained transport parameters for as-grown, N-implanted and implanted-annealed samples from the conductivity and Hall measurements are reported in Table 4.4. In this table electrical parameters for chemically doped GaSe crystal are also given for comparison [45]. The room temperature mobility of the as-grown sample was found as 20 $cm^2/V.s$. Fig.4.14 shows a typical Hall mobility-temperature dependencies. In this figure the mobility, computed from the Hall effect and conductivity data, is plotted as a function of temperature on a Log-Log scale to deduce the dominant scattering mechanism assuming a relation $\mu \propto T^{\pm n}$, where n is the temperature exponent. It can be seen from this figure, at lower temperature the Hall mobility is limited by ionized impurity scattering with $n = 5.4$. In the high temperature region for the same sample, the mobility decreases with increasing temperature according to $\mu \propto T^{-2.7}$. We may therefore assume that at the high temperature above 240 K, the scattering of holes was mainly due to phonon scattering.

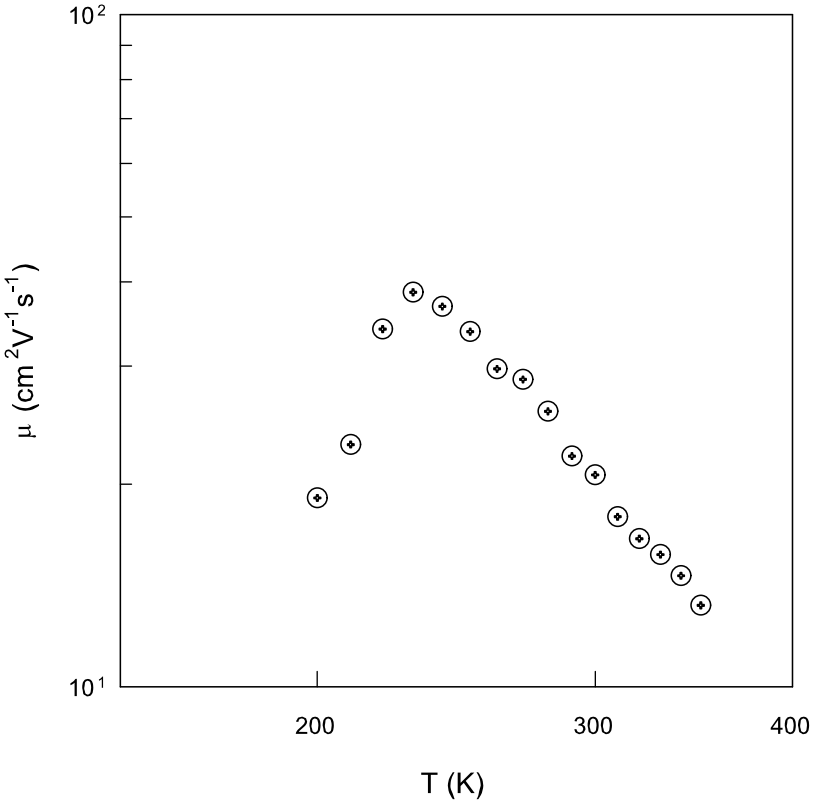

Figure 4.14: Mobility-temperature dependence of the as-grown sample.

In Fig.4.15, the mobility of holes in nitrogen implanted samples is plotted as a function of temperature on a Log-Log scale. The mobilities of the N-implanted and annealed samples (A2 and A3) at room temperature were 52 and 13 $cm^2/V.s$, respectively. The sample annealed at 500 ^oC (A2) exhibits two regions. At low temperature, the mobility increases with temperature reaching a maximum value of 157 $cm^2/V.s$ at around 220 K and obeys the power law $\mu \propto T^{5.0}$ with a quite high n value. This behavior of the mobility is assumed to be due to ionized impurity scattering mechanism. In the high temperature region for the same sample, the mobility decreases with increasing temperature according to $\mu \propto T^{-3.9}$ in

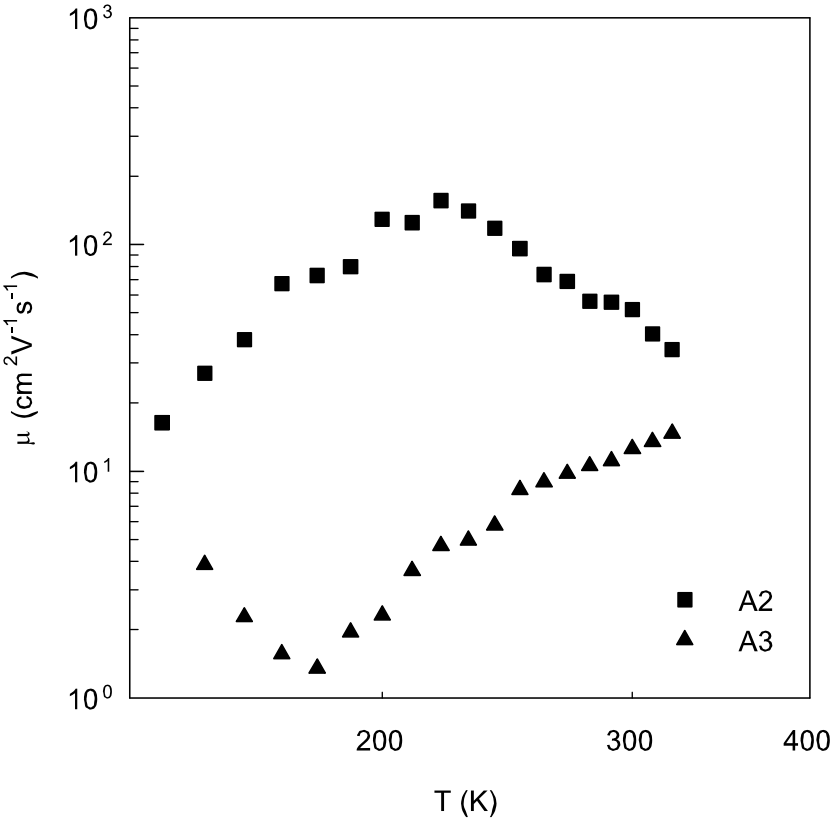

Figure 4.15: Mobility-Temperature dependence of the N-implanted and annealed at 500 ^{o}C (A2) and at 700 ^{o}C (A3) samples.

nitrogen implanted samples. We may therefore assume that at the high temperature above 220 K, the scattering of holes was mainly due to phonon scattering. This unfamiliar mobility-temperature dependence compared to $\mu \propto T^{\pm 3/2}$ is the result of the special form of the density of states in layer structures, such as stacking fault, as observed by [21] in p-type GaSe single crystal. On the other hand, the mobility-temperature dependence of the nitrogen implanted sample annealed at 700 ^oC (A3) shows anomalous behavior compared to the other GaSe samples. In low temperature region, (in between 100-180 K) the mobility decreases with

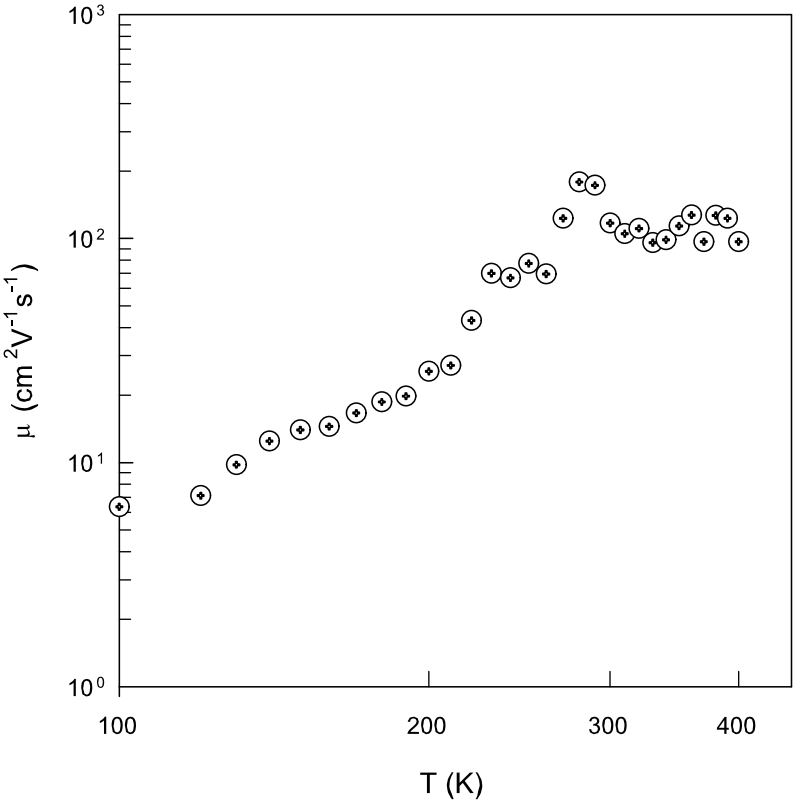

Figure 4.16: Mobility-Temperature dependence of the Si-implanted and annealed at 500 ^{o}C sample (B2).

increasing temperature reaching minimum values at around 180 K with the mobility of 1.4 $cm^2/V.s$ and then increases with increasing temperature. This kind of behavior was reported for a non-stoichiometric p-type InSe single crystal in [78], but in this study, mobility decreases with increasing temperature reaching a zero value, then increases with increasing temperature and the carrier type changes n to p at some critical temperature below 215 K. As mobility approaching the type conversion point, mobility-temperature exponent gets higher values greater than 10. This anomalous change of carrier type in p-InSe is created by interstitial impurities and inter-layer defects which produce two-dimensional accumulation

Table 4.4: Comparison of electrical parameters obtained in this study with chemically doped GaSe crystal study of Sanchez et al.[45]*.

Sample No	*Nitrogen* concent	ρ_{300K} $(\Omega - cm)$	P_{300K} (cm^{-3})	μ_{300K} $cm^2/V.s$	$E_{\sigma 1}$ (meV)	$E_{\sigma 2}$ (meV)
$A0$	*undopped*	$9.0x10^6$	$1.8x10^{11}$	20	269	66
$A1$	$as - imp.$	$2.6x10^5$	—	—	255	46
$A2$	$6.0x10^{15} ion/cm^2$	$3.8x10^4$	$4.0x10^{10}$	357	252	33
$A3$	$6.0x10^{15} ion/cm^2$	$5.6x10^3$	$9.0x10^{12}$	87	26	8
$*$	*Undoped*	$1.0x10^6$	$1.0x10^{11}$	—	—	—
Chemically$*$	0.1%	$1.0x10^4$	$1.0x10^{13}$	—	—	—
Chemically$*$	0.5%	20	$4.0x10^{15}$	37	210	—

layer. In our case, mobility-temperature values for the sample annealed at 700 ^oC did not show any type conversion point, but exhibit the same behavior up to 180 K with higher temperature exponent. Therefore, high values of n may be attributed to the high concentration of the sheet defects especially the stacking faults behaving like a shallow acceptor level in such layered structures. These high values of n may also be the indication of low structural quality of the grown crystal and of the structural deformations created by N atoms at high annealing temperature. PAL et al. observed the same type of anomalous behavior as in our sample A3 and high value for $n\sim$3.3 in their undoped GaTe samples and they attributed this behavior to the presence of interlayer stacking faults [79]. The sheets defects in layered structures might indeed be compensating the lattice scattering mechanisms, increasing the carrier mobility after some critical temperature. So, the mobility-temperature variation might be proposed to be dominated by the structural defects.

Fig.4.16 shows the hole mobility variation versus temperature for Si-implanted and annealed at 500 ^{o}C sample. Like the N-implanted sample (A2), Si-implanted

and annealed at 500 ^{o}C sample obeys the power law $\mu \propto T^n$ with n=3 at low temperatures and the scattering of holes was mainly due to phonon scattering. Above the room temperature, nearly temperature independent mobility variation was observed which can be ascribed to the neutral impurity scattering mechanism.

4.4 Space-Charge-Limited Current measurements

The current-voltage characteristics were carried out with current flowing along the c-axis using samples cleaved from the ingot that were cut in squares of 1 cm^2. The thickness of the samples ranged from 50 to 100 μm along the c-axis. The electrodes were attached to the two sides of the layered sample as sandwich geometry by indium and a slight diffusion was carried out at 200 ^oC in order to improve the ohmicity. At the low voltage values, the I-V characteristics were checked whether it is ohmic or not. It was observed that the behavior was ohmic and showed a symmetrical behavior with respect to the voltage polarity.

Fig.4.17 shows the I-V characteristic of as-grown GaSe single crystal at room temperature. It can be seen from this figure that the I-V variation consists of an ohmic region at low voltages, followed by a square-law region. Then the current starts rising steeply, starting from the voltage value V_{TFL} and followed trap-free square-law region in the investigated voltages range. The relation between applied voltage value and current was of the type $I \propto V^n$, where n is the power exponents for each region and its value is displayed for each quadratic current-voltage regions in the figure. As seen from the figure, ohmic region is followed by quadratic region and trap filled region. This behavior was characterized according

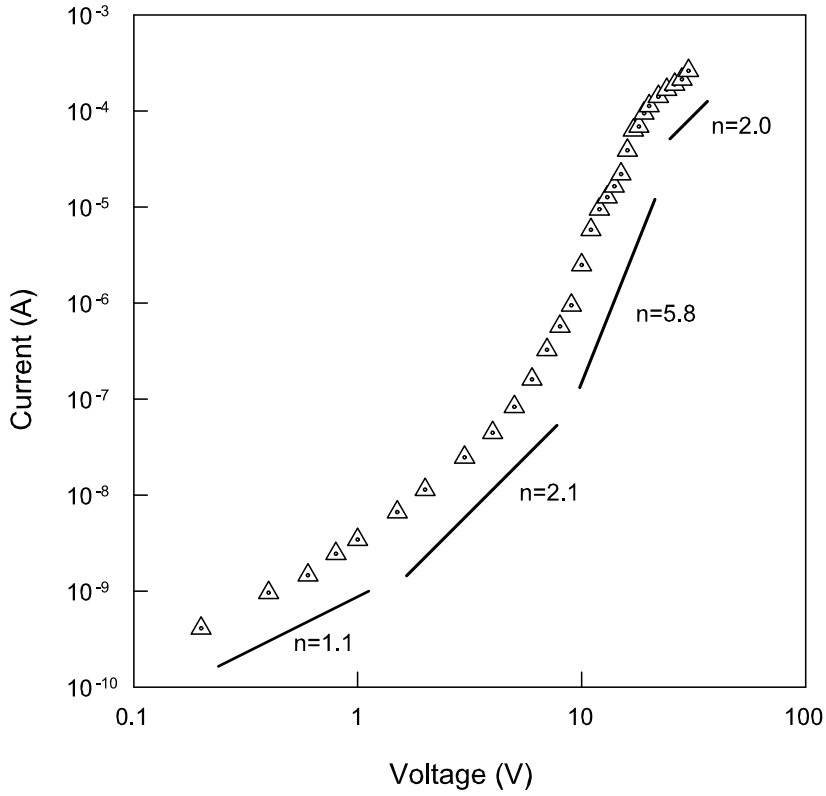

Figure 4.17: The room temperature I-V characteristic of as-grown GaSe sample.

to regional approximation by Lampert and Mark. Therefore, assuming a single set of traps, the analysis of experimental data has been carried out by using the model proposed by Lambert [80]. By using the experimental value of V_{TFL} and the following expression;

$$V_{TFL} = \frac{ed^2 N_t}{2\epsilon}. \tag{4.4}$$

the room temperature trap density N_t has been determined as N_t=5.1×10^{12} cm^{-3}. By using Eqn.2.30 and Eqn.2.31, the deep trap position E_t has been found as 588 meV at room temperature. The obtained trap density and position are in agreement with that obtained by Manfredotti at al. [30]. They found three

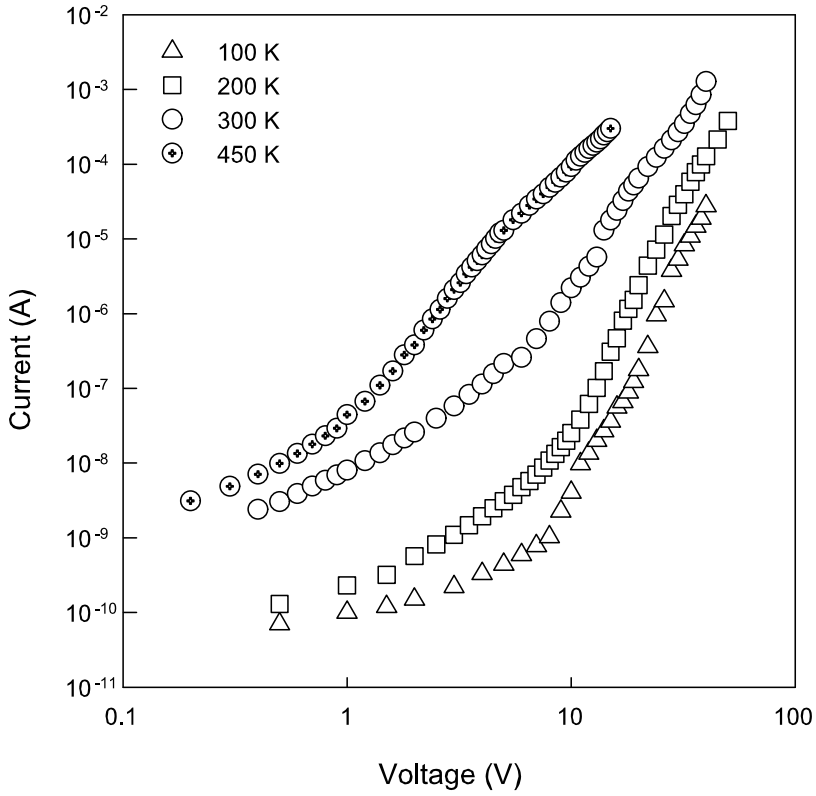

Figure 4.18: I-V characteristic for as-grown GaSe sample at different ambient temperatures.

deep hole traps at 421, 465 and 543 meV above the valance band and with concentrations ranging between 10^{12} and $10^{13} cm^{-3}$.

As seen from Fig.4.18, at each temperature, the current-voltage characteristics shows similar behavior and consists of an ohmic region and a superlinear region followed by a vertical region. In order to determine the trap position E_t, considering the temperature dependence of N_c, $\ln(I_{TFL}T^{-3/2})$ versus 1/kT was plotted at a fixed voltage value. Such a plot at 10 V is shown in Fig.4.19 and the slope of this straight line gives the trap position as $E_t = 240$ meV. The obtained

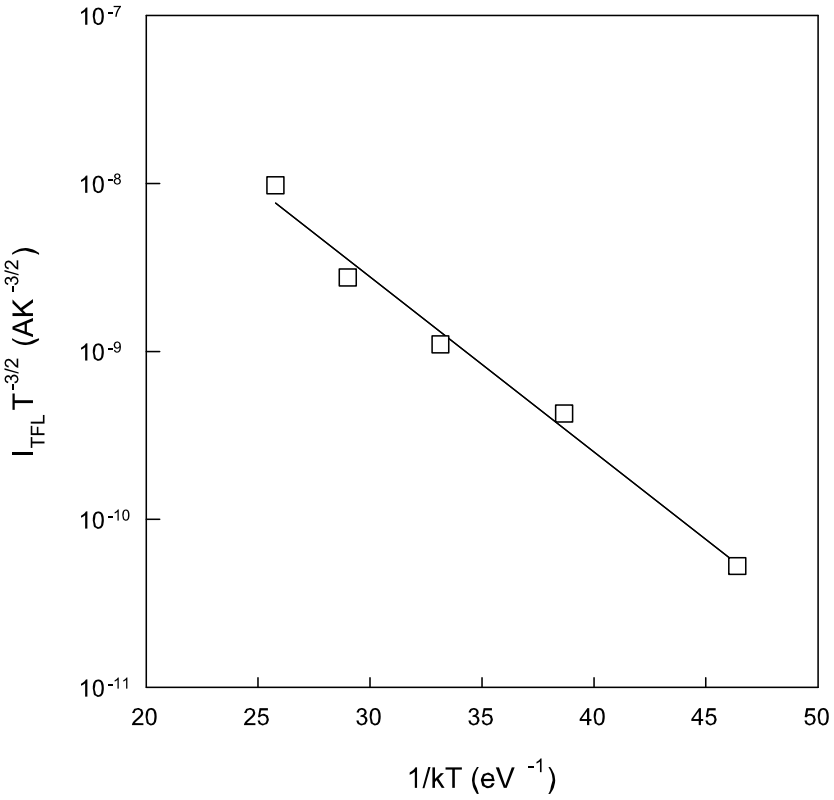

Figure 4.19: $I_{TFL}T^{-3/2}$ versus 1/kT plot at 10 volt.

trap position by SCLC methods is in agreement with the value obtained by conductivity measurements for as-grown GaSe. Anis et al. [81] have reported similar SCLC behavior for undoped GaSe single crystal with 195 meV activation energy.

4.5 Photoconductivity and Spectral Analysis of the as-grown and implanted Samples

To deduce the effect of implantation on the photoconductivity properties, photoconductivity (σ_ϕ) measurements have been carried out as a function of temperature and illumination intensity. Fig.4.20 and Fig.4.21 show the photoconductivity as a function of inverse temperature for unimplanted, N- and Si-implanted and annealed samples under the constant illumination intensity of 55 mW/cm^2 together with the dark conductivity.

As it is seen, the illumination increases the photoconductivity values of unimplanted sample much more than that of implanted and annealed samples. In the studied temperature range, the photocurrent is much higher than the dark current and seems to approach a constant value asymptotically. It should be noted that when the annealing temperature was increased, the photocurrent increases with different activation energies. This implies that the number of thermally generated carriers is smaller than the photo-excited carriers. Therefore, the photoconductivity is governed by trapping or recombination centers above valance band depending on the temperature and illumination intensity [58].

The temperature-dependent photoconductivity measurements have been carried out on N- and Si-implanted samples at different illumination intensities. Fig.4.22 and Fig.4.23 show the variations of the photoconductivity as a function of temperature at different illuminations, namely, 20, 35, 55, 80 and 90 mW/cm^2 for typical N- and Si-implanted samples (N- and Si-implanted and annealed at

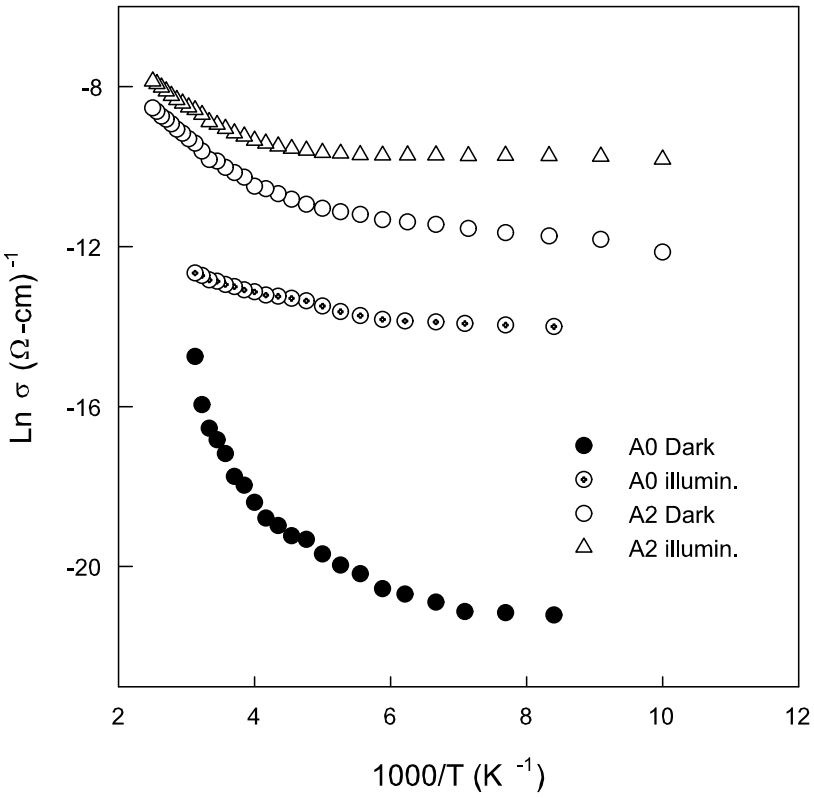

Figure 4.20: The temperature dependent dark conductivity and photoconductivity of as-grown (A0) and N-implanted and annealed at 500 ^{o}C sample (A2) at the constant illumination intensity of 55 mW/cm^2.

500^{o}C) at applied electric field of 50 V/cm. As can be seen from these figures, the photoconductivity increases exponentially with increasing temperature at each illumination intensity, and also increases with increasing illumination intensity at each absolute temperature. It is clear that each plot of Fig.4.22 and Fig.4.23 consists of two different regions above and below 200 K with different activation energies. They were calculated from the slope of $Ln\sigma_\phi$ versus $1/T$ plots.

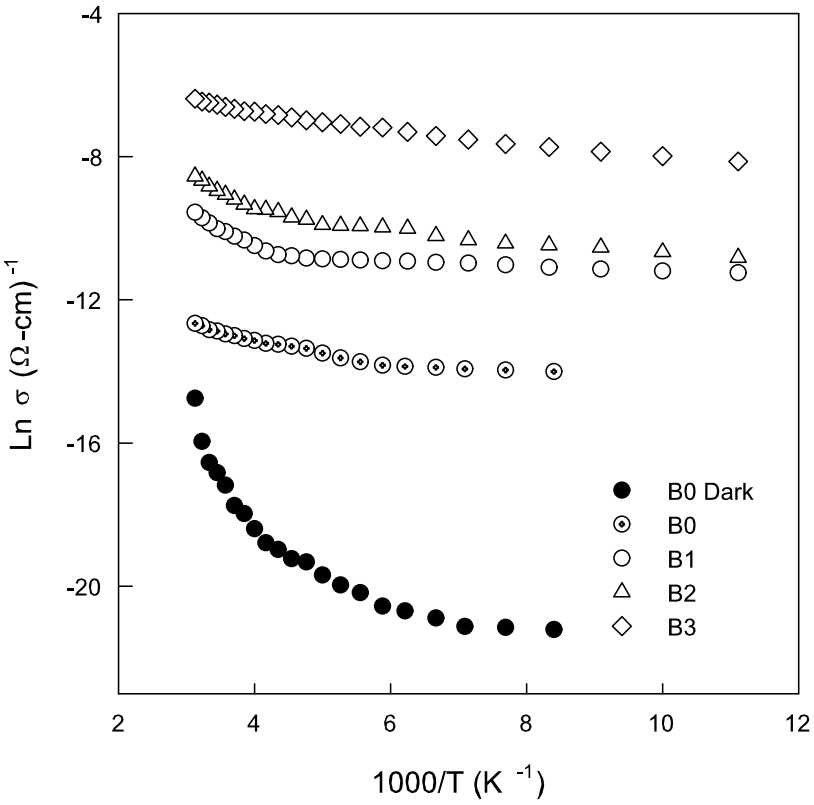

Figure 4.21: The temperature dependent dark conductivity and photoconductivity of as-grown and Si-implanted and annealed samples under the constant illumination intensity.

The ionization energies calculated from the slope of $Ln\sigma_\phi$ versus $1/T$ plots for N-implanted and annealed at 500 ^{o}C sample were 94, 90, 80, 68 and 57 meV for the illumination intensity 20, 35, 55, 80 and 90 mW/cm^2, respectively in the high temperature region. In the low temperature region, the variation of conductivity with temperature is weak and the activation energy decreases from 10 to 2 meV with increasing illumination intensities. For the Si-implanted and annealed at 500 ^{o}C sample, these values were found as 75, 68, 65 and 57 meV

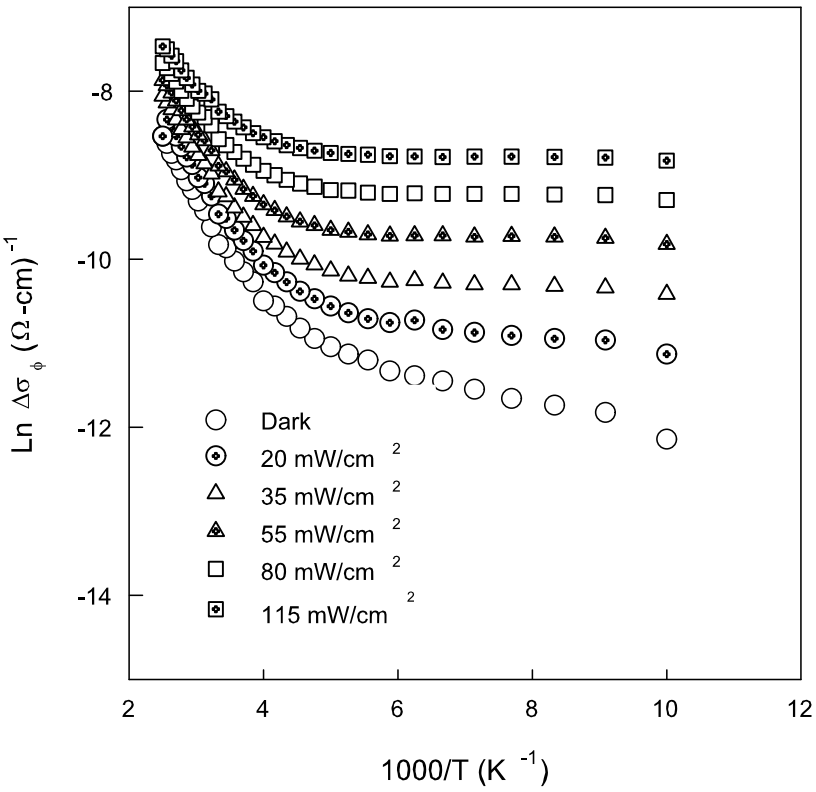

Figure 4.22: The temperature dependent photoconductivity of a typical N-implanted and annealed at 600 ^{o}C sample for different illumination intensities.

in the high temperature region while, in the low temperature region, the temperature dependent photoconductivity is temperature insensitive with nearly 10 meV activation energy for each illumination intensity. This saturation value is an indication of the existence of impurity levels in the implanted samples. As the illumination intensity is increased, the impurity levels produced by the N- and Si-implantation are fully ionized, and this result in almost constant temperature variations of the photoconductivity at high illumination intensities. Similar photoconductivity measurements were reported earlier for $CuInTe_2$ and $Cu(In,Ga)Se_2$

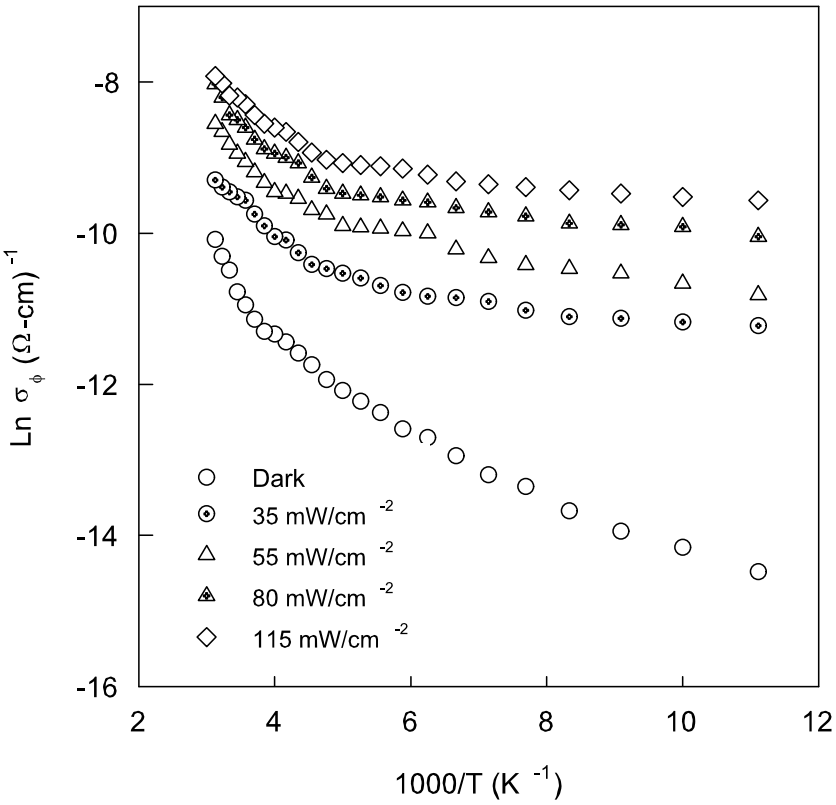

Figure 4.23: The temperature dependent photoconductivity of a typical Si-implanted and annealed sample (B2) for different illumination intensities.

films [82, 83]. To obtain the characteristics of trapping or recombination centers, photocurrent vs illumination intensity (ϕ) characteristics of all samples were measured at a constant electric field. Fig.4.24, 4.25 and 4.26 show the plot of Log (I_{pc}) versus Log ϕ for as-grown, N- and Si-implanted and annealed samples at different absolute temperature. The temperatures and calculated slopes are indicated on the figures. It can be observed from these figures, photocurrent increases with increasing temperature and these dependencies were of the $I_{pc} \propto \phi^n$ type. The power exponent n is a function of the recombination mechanism of non-equilibrium carriers. For all the samples n values vary in between 1 and 2.

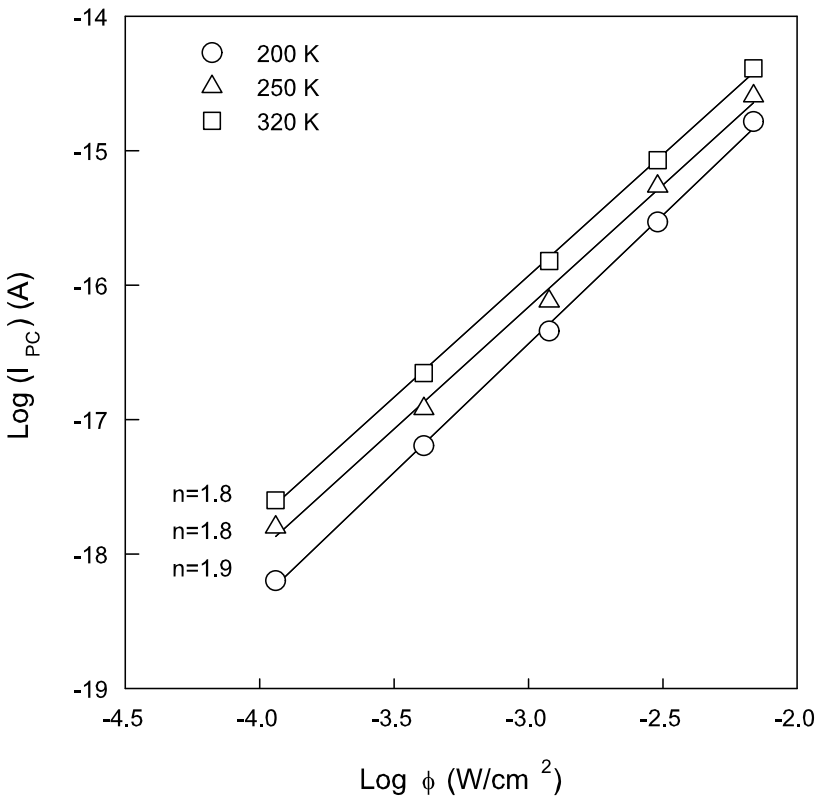

Figure 4.24: Photocurrent-illumination intensity behavior of as-grown GaSe single crystal at different ambient temperatures.

One can see from Fig.4.25, that n value increases with increasing temperature. The power exponents were determined as around 2 for as-grown and implanted-annealed at 700 ^{o}C and as 1.5 for as-implanted samples. The slopes n=1 and n=2 are due to impurity and two-photon process, respectively. The super-linear slope (n=2) of the photoconductivity can be explained by the influence of an energy barrier on the non-equilibrium carrier mobility [52, 84].

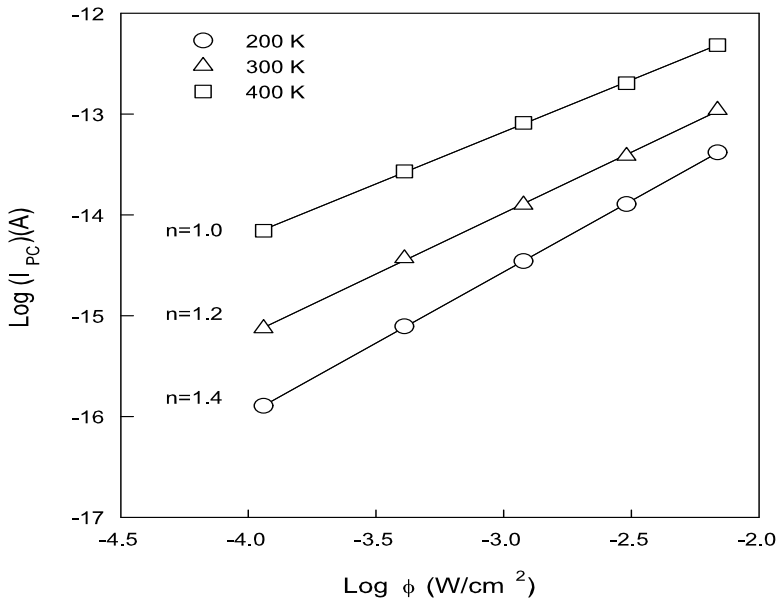

Figure 4.25: Photocurrent-illumination intensity behavior of a typical N-implanted and annealed at 500 ^{o}C sample (A2) at different ambient temperatures.

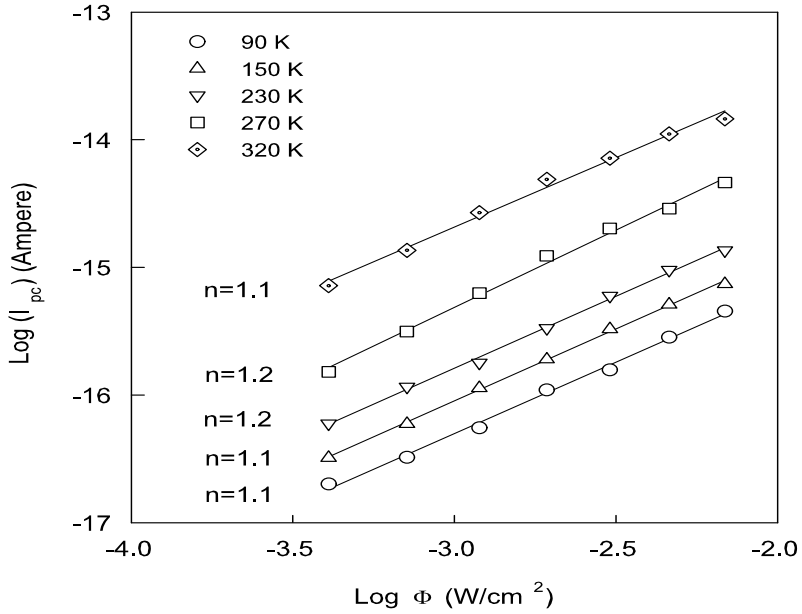

Figure 4.26: Photocurrent-illumination intensity behavior of a typical Si-implanted and annealed at 500 ^{o}C sample (B2) at different ambient temperatures.

Since the super-linear photoconductivity corresponds to an increase in lifetime with illumination intensity, thus the material is becoming more photosensitive as the illumination intensity is increased. These phenomena is associated with two-center effects, such as the incorporation of additional imperfections, and it leads to a larger lifetime for one of the carriers than previously presented. As a result, both dark conductivity and photoconductivity increase [58]. Therefore, the calculated values of activation energies obtained from dark and illuminated conductivities might be attributed to continuous trapping levels produced by the implantation of N-and Si-atoms and by the effect of annealing. Almost the same trapping levels were observed from the self-coactivated luminescence in Zn doped GaSe [35] and also De Blasi et al. obtained about the same exponent in their photoconductivity study of InSe single crystal [85].

The photocurrent-light intensity variations were also studied at different applied fields. Fig.4.27 shows the plot of Log (I_{pc}) versus Log ϕ for N-implanted and annealed at 500 ^{o}C sample for different field strengths. The power exponent is independent of the strength of applied fields as expected.

For the spectral photoconductivity analysis, we used an Oriel MS 257 monochromator and the photocurrent was measured in the wavelength range of 500-700 nm in steps of 5 nm by using HP 4140 picoammeter/dc voltage source. Fig.4.28 shows the spectral distribution of highly resistive as-grown GaSe single crystal at different temperatures. The photoconductivity spectrum exhibits rapid rise of the photocurrent around the band gap, i.e. in the photon energy range of 1.90-2.06 eV, and increases with the temperature. The maximum response of PC

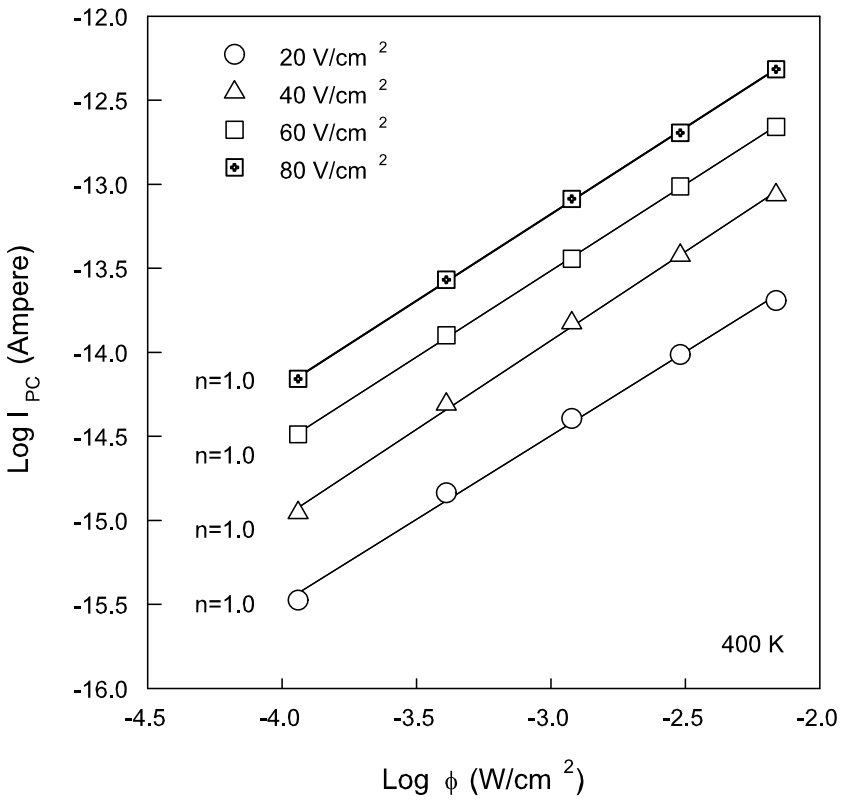

Figure 4.27: Photocurrent-illumination intensity behavior of a typical N-implanted and annealed sample (A2) at different applied fields.

spectra was obtained at about 2.06 at 50 K and 1.96 eV at 320 K for undoped as-grown GaSe single crystal. This is in agreement with the band gap of this crystal deduced from the optical absorption and photoluminescence measurements.

Asymmetrical broadening band of PC spectrum of GaSe crystal was observed in the energy range 2.0-2.4 eV. This can be due to structural defects and impurities. Similar broadening of the PC spectrum was reported for GaS_xSe_{1-x} mixed crystals and Na-intercalated GaSe single crystals [86, 87, 88]. This behavior was attributed to the presence of native structural defects such as Ga, S or Se interstitial atoms and/or vacancies and strain induced defects, as well as the presence of

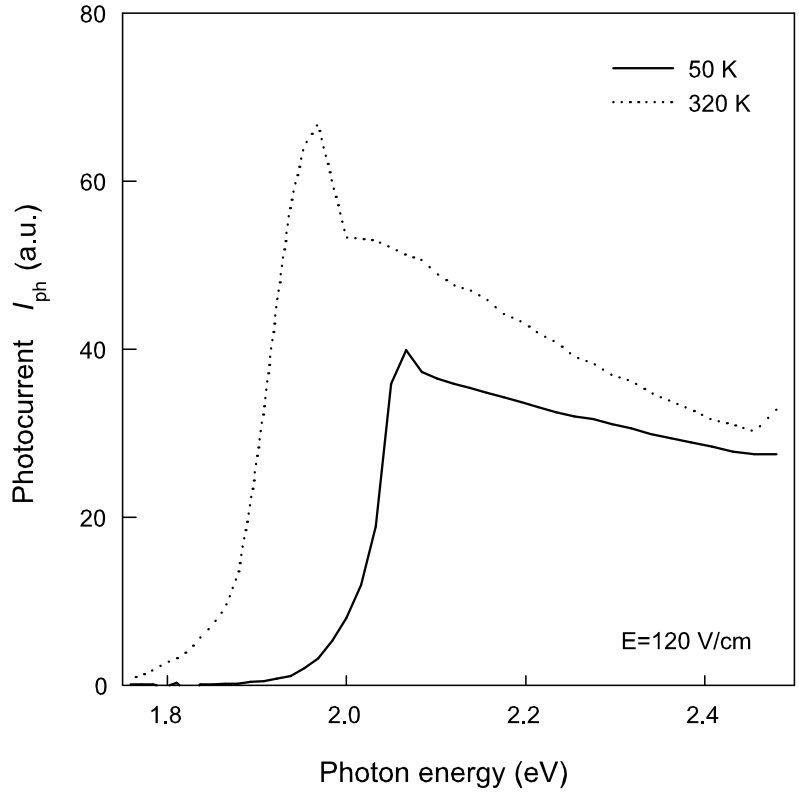

Figure 4.28: Spectral distribution of photoconductivity of as-grown GaSe single crystal at 50 and 320 K.

Si impurities introduced to the material during the growth process for uncoated ampoules

Fig.4.29 and 4.30 show the spectral distribution of N-and Si-implanted and annealed samples, respectively. In these figures, the spectral distribution of as-grown sample has also been given for comparison. As it can be seen from these figures, the maximum response was obtained at 2.03 eV for N-implanted and annealed samples. For Si-implanted and annealed samples, the maximum response was obtained at 2.04 eV at 50 K. This variation shows that N-and Si-implantation into GaSe single crystals together with annealing has a pronounced effect on the

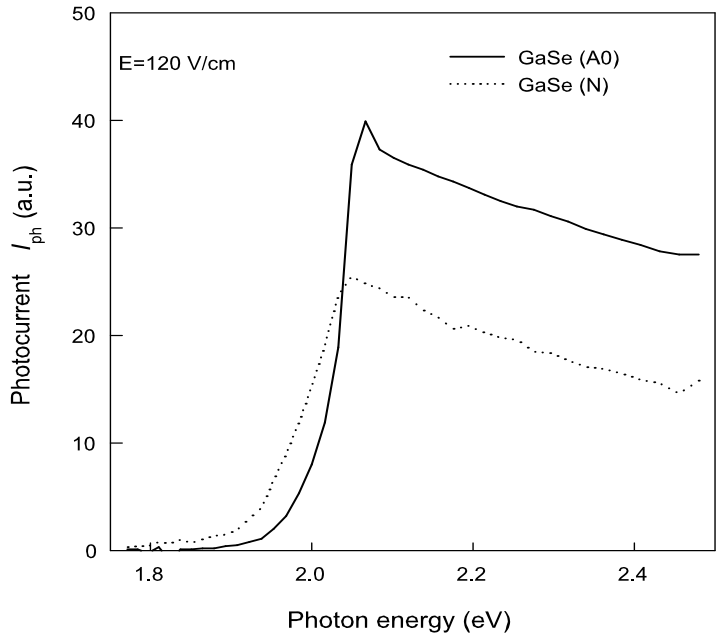

Figure 4.29: Spectral distribution of photoconductivity of as-grown and annealed (A2) GaSe single crystals at 50 K.

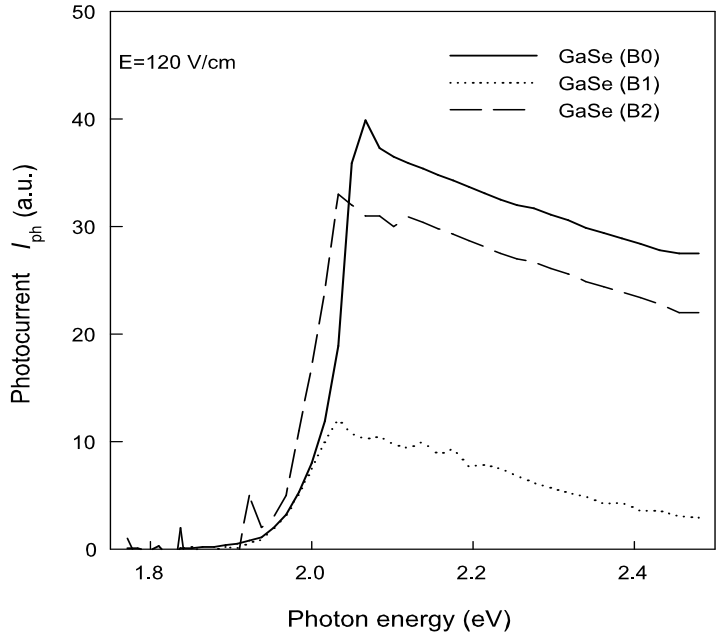

Figure 4.30: Spectral distribution of photoconductivity of as-grown, Si-implanted (B1) and annealed (B2) GaSe single crystals at 50 K.

photoconductivity properties. Therefore, we attributed this effect to the N- and Si-modification and doping of the semiconductor.

4.6 Optical Characterization of the Undoped, N- and Si-Implanted GaSe Single Crystal

4.6.1 Optical Absorbtion

Optical transmission or absorbtion are routinely used for characterization of the materials. These measurements give information about the optical absorbtion coefficient, band structure and impurity levels of a semiconductor. In these measurements, light is incident on the sample, and the transmitted light is measured as a function of wavelength. The optical absorbtion coefficient α can be determined using the relation

$$\alpha = \frac{1}{d} ln(\frac{1}{T}) \tag{4.5}$$

where d is the thickness of the material and T is the transmittance. In general, the relation between the absorbtion coefficient and photon energy is

$$\alpha h\nu = A[h\nu - E_g \pm E_p]^n \tag{4.6}$$

where A is a parameter depending on transition probability, E_g is band gap, E_p is the phonon energy (E_p=0 for direct transition) and n is a index which can be assumed to have values of 1/2, 3/2, 2 and 3 depending on nature of electronic transition responsible for the absorbtion. The values 1/2 and 3/2 refer to the allowed and forbidden direct transitions, respectively and 2 and 3 refer to the

allowed and forbidden indirect transition, respectively [61]. Fig.4.31 shows the absorbtion spectrum of undoped GaSe single crystal as a function of $h\nu$ measured by using a Perkin Elmer UV-VIS spectrometer. As it is seen, a plot of $(\alpha h\nu)^2$ versus $h\nu$ gave a straight line. Since the transmission measurements have been carried out at the room temperature and the value of α is in the order of $10^4 m^{-1}$, the presence of exciton is not possible. Therefore, the absorbtion is due to an allowed direct transition from the valance band to the conduction band. The band gap energy determined from the intercept was found as 1.985 eV at room temperature for undoped Gase.

The absorption spectrum for N- and Si-implanted GaSe crystals are shown in Fig.4.32 and Fig.4.33. As seen from these figures, the band gap of the GaSe crystal decreases with N- and Si-implantation and also decreases with annealing of the implanted sample. It is determined as around 1.975 eV after implantation and post annealing. The observed decrease in the band gap can be related with the structural defects introduced by implantation with subsequent annealing.

4.6.2 Photoluminescence Properties of GaSe Single Crystal

Photoluminescence (PL) spectroscopy is a contactless and nondestructive method for determining the electronic structure of materials. By the help of PL measurements, it is possible to determine the band gap, impurity levels and defects. It also gives information about the recombination mechanism within the crystal.

For the photoluminescence measurements, the samples were prepared by cleaving an ingot parallel to the layer which was perpendicular to the c-axis. A pulsed

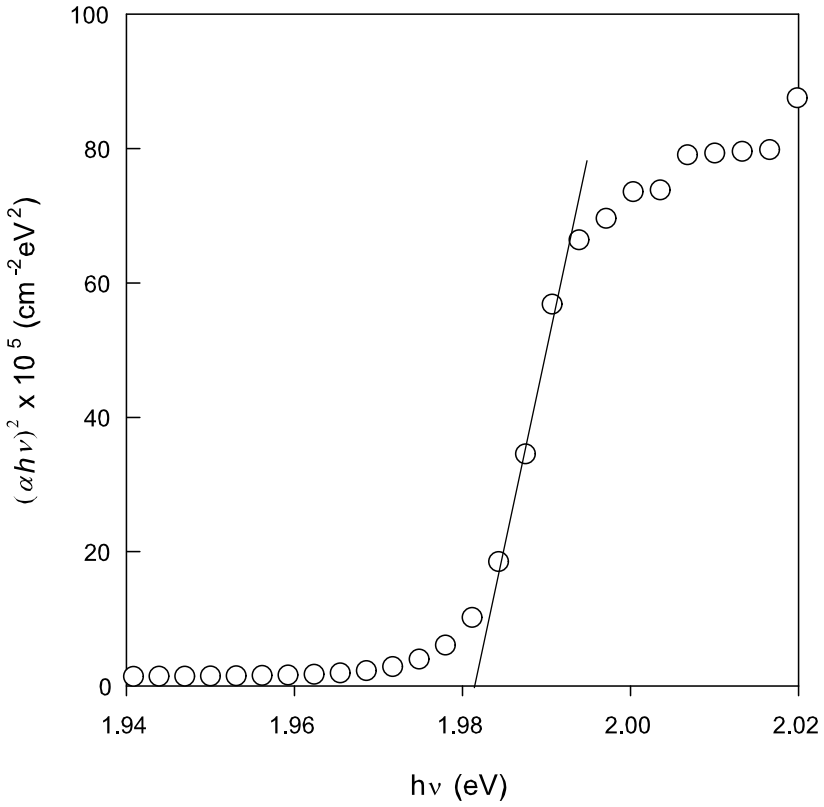

Figure 4.31: Optical absorption spectra of as-grown GaSe (A0) at room temperature.

nitrogen laser operating at a wavelength of 337 nm was used as the source of excitation. The intensity of the laser beam was about 7 mW/cm^2. Fig.4.34 shows the photoluminescence (PL) spectra of the undoped GaSe single crystal at 36 K. For the as-grown sample, three emission bands denoted A, B and C were observed at 2.114, 2.090 and 2.060 eV, respectively. The line at 2.114 eV agreeing with the value given in literature and it was attributed to the well known recombination of the direct free exciton (DFE). The ionization energy of the DFE was found to be 20 meV and using this value, the direct band gap of GaSe was calculated as 2.128 eV at 4.2 K [16].

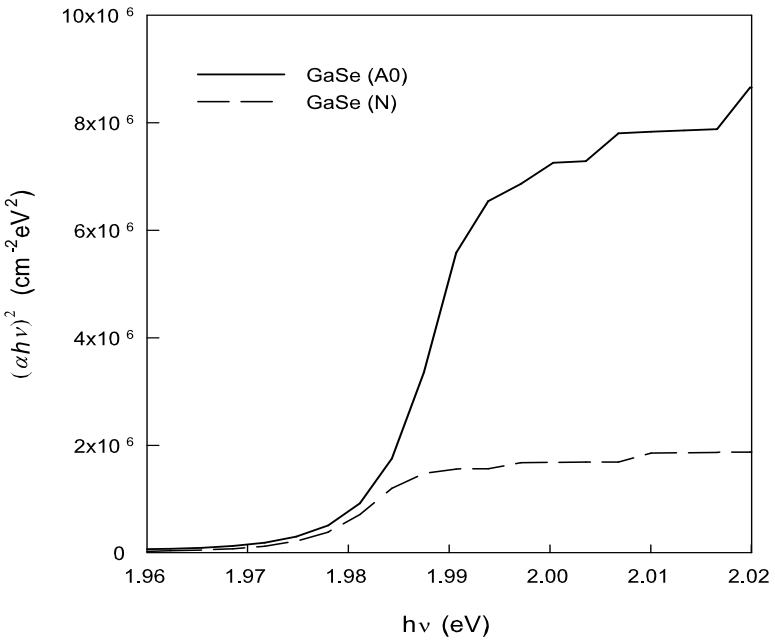

Figure 4.32: Optical absorption spectra of as-grown and annealed (A2) GaSe samples at room temperature.

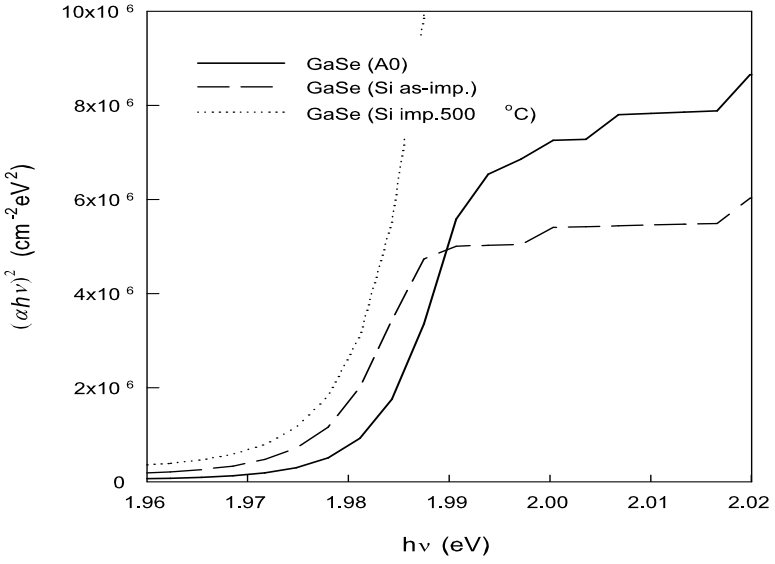

Figure 4.33: Optical absorption spectra of as-grown (B0), Si-Implanted (B1) and annealed at 500 ^{o}C (B2) GaSe samples at room temperature.

The intensity of photoluminescence and its dependencies on temperature are directly related to the dominant recombination process. It was found that, the variation of the peak energy with temperature is similar to the variation of the band gap for the bound excitation (BE) [89]. A similar behavior of the peak energy as a function of temperature has been observed for the band-impurity and the donor-acceptor transitions [90, 91]. In addition to these variations, a peak energy shift greater than the temperature variation of the band gap energy was observed for the donor-acceptor transition. This behavior was explained as transition involving substitutional acceptor and interstitial deep donor level [92].

Therefore, in order to determine the transition mechanisms and band structure of this layered crystal, the temperature dependent photoluminescence measurements have been carried out. The temperature dependence of the peak energy for the A and B emission bands are plotted against to the temperature in Fig.4.35. As seen from this figure, the variation of the peak energy of the B emission line with temperature is similar to band gap energy variation and decreases as the temperature increases with:

$$\frac{dE_{exc}}{dT} = -4.0 \times 10^{-4} eV/K \tag{4.7}$$

The same behavior was observed for the $n = 1$ exciton as -4.7×10^{-4} eV/K [93] and -3.1×10^{-4} eV/K [94].

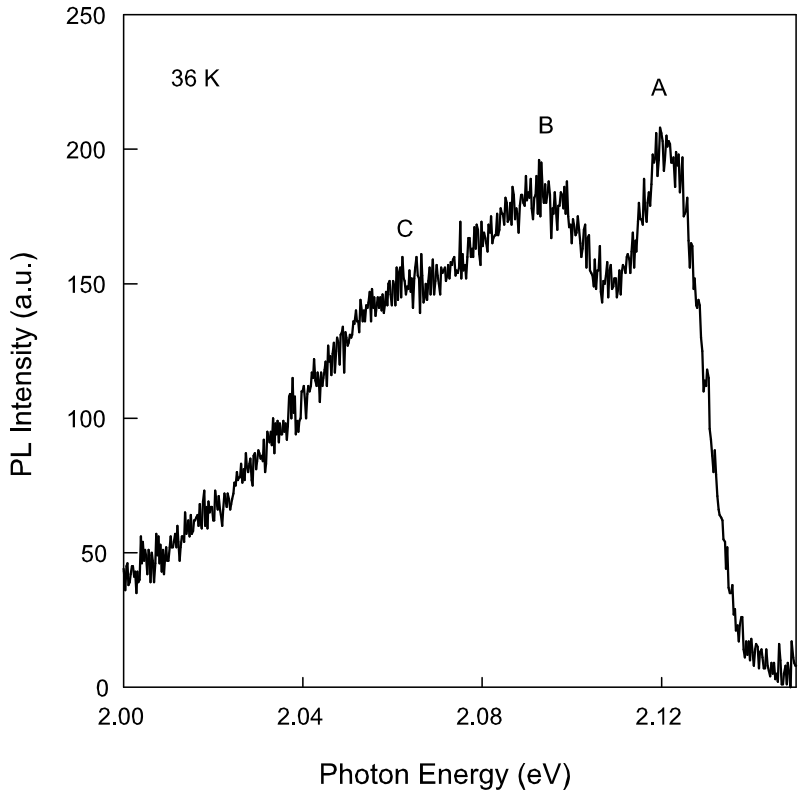

Figure 4.34: PL spectra of as-grown GaSe (A0) single crystal at 36 K.

Therefore we can attribute this emission line to the recombination of direct bound exciton (DBE). Conductivity and Hall effect measurements showed that our Bridgman grown samples shows p-type conductivity. Therefore, in order to determine the acceptor level position of the B emission line from the PL measurements, we have used effective-mass approximation [95]. This approximation describes the recombination of shallow exciton bound to neutral donors and acceptors. The energy $E(A^o, x)(\sigma^{-1})$ of the exciton-acceptor complex (A^o, x) is related to the energy $E(D^o, x)(\sigma)$ of the exciton-donor complex (D^o, x) and this

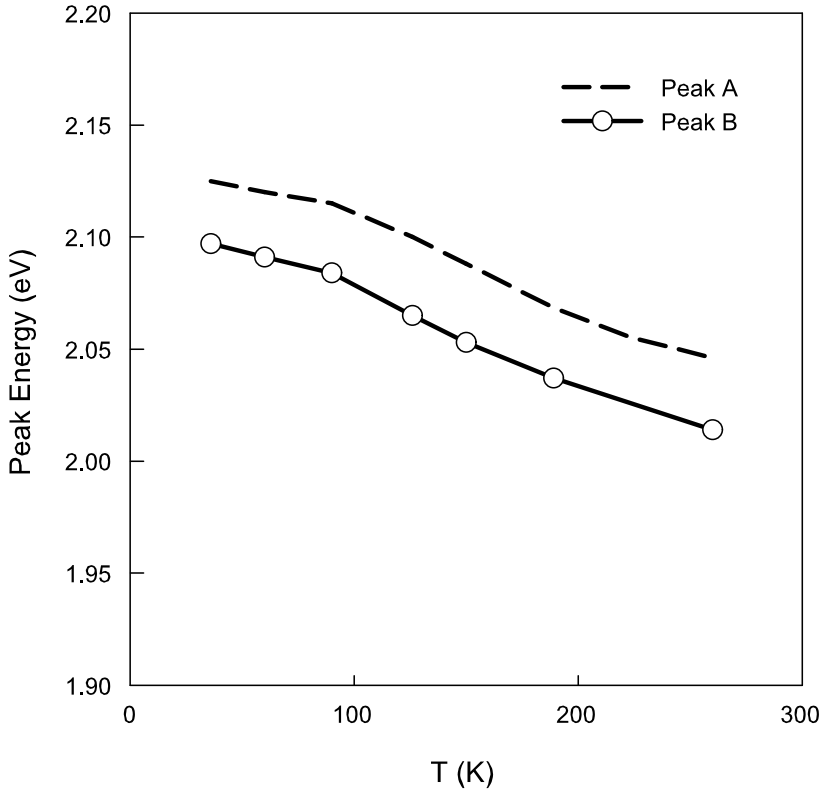

Figure 4.35: Temperature dependencies of the peak energies .

relation is given as;

$$\frac{E(A^o, x)(\sigma^{-1})}{E_D} = \frac{E(D^o, x)(\sigma)}{E_D} \tag{4.8}$$

The calculated binding energy W as a function of the mass ratio σ and of the inverse σ^{-1} was given by Ungier et al. in Fig.1 [95]. Using the effective electron and hole masses, the two ratios (σ values) of electron- to-hole masses relative to the direct and indirect parts, $\sigma^d = 0.41$ and $\sigma^i = 1.47$ was calculated by Capozzi et al. [26].

By using $\sigma^d = 0.41$ and curve A of Fig. 1 given by Ungier at al., we obtain $W^d(A^o, x)/2E_A = 4.7 \times 10^{-2}$. In our case, the binding energy (W) of this DBE

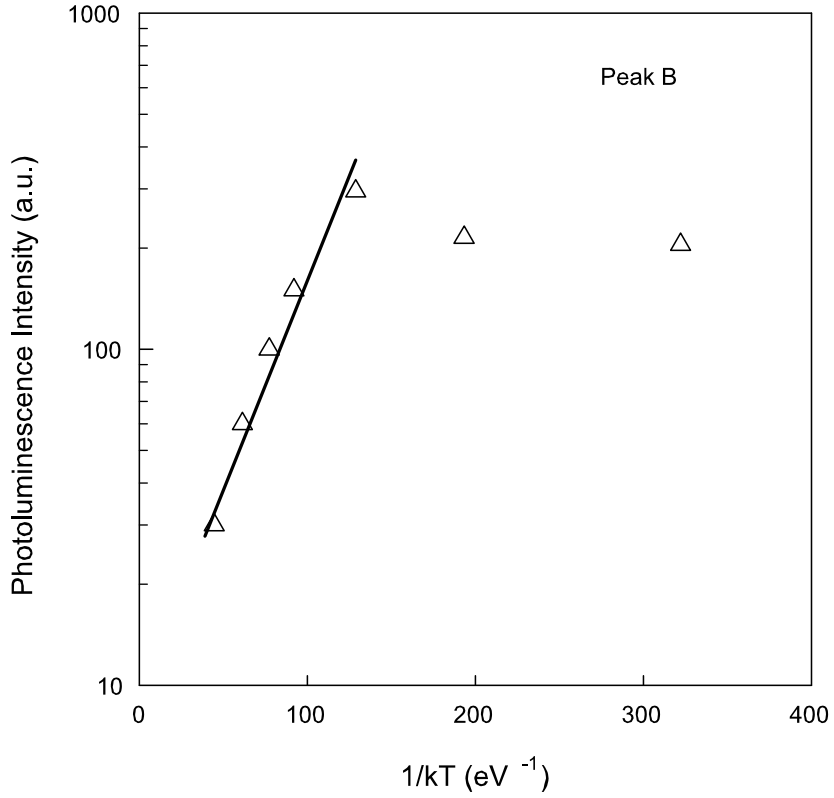

Figure 4.36: Variation of PL intensity with reciprocal temperature for peak B.

is equal to its activation energy. Semilogarithmic plots of the PL intensity of the B emission band is shown against the reciprocal temperature in Fig.4.36. The PL intensity of the B emission band gradually decreased with increasing temperatures between 90 and 160 K. The activation energy for thermal quenching of 23 meV in the B emission band was obtained from the slope of the straight line at this temperature interval. This thermal quenching energy is nearly the same as the energy difference between the A and B lines observed from the emission spectra (24 meV). Using this activation energy as the binding energy, the impurity level was calculated as 251 meV. This value is in agreement with the ionization

energy of the acceptor center deduced from the electrical measurements which was obtained as 243 meV. Then, we propose that the B line is due to the recombination of direct exciton bound to neutral acceptor at about 250 meV above the valance band. The same B lines has been observed in [96] at 2.075 eV at 77 K with 23 meV thermal activation energy which is the thermal freeing of excitons from impurities centers. But it was attributed that this is a donor level, lying 195 meV below the DCB [97]. In another study, this line was observed at 2.078 eV at 80 K with 20 meV thermal activation energy [26]. Using the calculation on excitons bound to neutral donors and acceptors proposed by Ungier et al., the activation energy was obtained as 213 meV and attributed to the acceptor center lying above the valance band.

The emission line observed at 2.060 eV was only seen at low temperature and disappeared rapidly with increasing temperature. Therefore, we could not observe the intensity variation with temperature in a wide temperature range. The peak, observed by Capozzi at 2.035 eV, probably is the same emission line and observed only for high-quality crystals. Because of the weak temperature dependence, this line was attributed to the radiative decay of the indirect free exciton (IFE) with emission of an $A_1^{'}$ phonon [97]. However, the rapid disappearing of this line with increasing temperature does not support this interpretation. Therefore, C emission band may be associated with the impurities introduced during the growth process. Similar intra-center transitions between trap states have been observed in doped GaSe single crystals [98, 16].

CHAPTER 5

CONCLUSION

In this study, using 3-zone vertical Bridgman-Stockbarger system, we have grown undoped (not intentionally doped) GaSe single crystals by direct solidification of the melt. In order to determine the dopping effect on GaSe, N- and Si-atoms were implanted to as-grown crystals. N-implantation to GaSe single crystals was carried out perpendicular to c-axis with ion beam of 6×10^{15} ions/cm^2 dose having energy values 30 keV and 60 keV. For Si-implantation, the dose was 1×10^{16} ions/cm^2 with energy values 100 keV. As-grown and implanted crystals were examined with respect to structural, electrical and optical properties. Most important results of this study can be summarized as follows:

Surface morphology, stoichiometry, and structure of the samples were examined with a JSM 6400 scanning electron microscope equipped with an EDAX unit and X-ray diffraction technique. It was observed that the resulting ingot was stoichiometric. The peak positions obtained from XRD of the as-grown sample agreed with those of as-implanted and annealed samples. Intensities of the peaks were weaker in as-implanted samples as compared to as-grown samples. This is the indication of the reduction of crystalline nature as a result of implantation. The XRD patterns of as-grown, as-implanted and annealed samples showed that the preferred orientation for all the samples is along the c-axis with

the direction of (004) plane. Another result is that the increasing peak intensity along the direction of this plane is the evidence of increasing crystallinity and decreasing in structural disorder. The observed reflection peaks of x-ray spectra can be attributed to the typical $(00l)$ lines of the hexagonal structure of GaSe. The c-axis of these samples seem to be preferentially oriented parallel to the layer plane.

The temperature dependent electrical conductivities along and perpendicular to the c-axis were carried out to investigate the electrical anisotropy of as-grown crystals. A temperature dependent conductivity anisotropy above the room temperature was observed with a 20 meV activation energy which seems to be the barrier height between the layers. The acceptor levels calculated from the conductivity measurements along the layers were 44, 243 and 414 meV in the temperature ranges 120-220, 230-320 and 330-450 K, respectively. The depth of the impurity centers along the c-axis were 68 and 140 meV in the temperature ranges 120-220, and 230-320 K, respectively. In the high temperature region (in between 330-450 K), the activation energy was found to be 18 meV.

The conductivity measurements along the layer were also carried out on N- and Si-implanted samples in the temperature range of 100-320 K. It was observed that both N- and Si-implantation decrease the resistivity values from 10^7 to 10^3 Ω-cm depending on the implantation and post annealing processes. In the high temperature region (200-320 K), the activation energies obtained from conductivity measurements of the N-implanted and annealed at 500 ^{o}C samples lie in the range of 252-269 meV, while in the low temperature region (in between

100-190 K), the activation energies vary in the range of 33-66 meV. High annealing temperatures above 500 ^{o}C yielded quite low activation energies at low temperatures such as, the activation energies of the N-implanted and annealed at 700 ^{o}C sample were determined 26 and 8 meV, in the high and low temperature regions, respectively. For the Si-implanted and annealed samples, activation energies obtained from conductivity measurements were calculated as 158, 147 and 37 meV, respectively in the high temperature region(100-200 K). At low temperature region between 100 and 200 K, the activation energies of the same samples were found to be around 47, 46 and 14 meV. It is obvious that annealing of the implanted samples above a critical temperature weakens the temperature dependence of the conductivity and this critical temperature depends on the type of the implanted ions. These critical temperatures were determined to be around 600 and 700 ^{o}C for the Si and N-ions, respectively. Annealing of the implanted samples above this critical temperature weakens the temperature dependence of the conductivity. The absence of exponential dependence is the indication of defective degenerate structure produced by diffusion of the implanted atoms and the implantation induced defects and it is also associated with the fact that as the annealing temperature increases implantation related states become electrically active. Moreover, the weak temperature dependence of the dark conductivity with small small activation energy at low temperature region showed that the conduction mechanism dominated by hopping instead of thermal excitation, and the upper limit of temperature range of hopping mechanism moves towards the higher temperature as the annealing temperature increases.

In order to obtain a detailed information about the defect produced by N- and Si-implantation, the temperature dependent Hall measurements of the as-grown, N-and Si-implanted GaSe samples were carried out by using van der Pauw method. All the doped and undoped GaSe samples studied here exhibited p-type conduction verified by hot probe techniques and Hall effect measurements. The carrier density obtained from the conductivity and Hall measurements was analyzed by using single donor-single acceptor model (SDSA). The acceptor activation energy of as-grown sample was determined as 350 meV and the acceptor and donor concentrations were found to be $1.0x10^{14}$ and $8.6x10^{12}cm^{-3}$, respectively. For the N-implanted and annealed at 500 ^{o}C sample, SDSA analysis gave a deep acceptor energy level lying at 450 meV above the valance band originating from the variation of N-induced defects by the annealing with the N_a=$1.0x10^{13}$ and N_d=$3.5x10^{10}cm^{-3}$. However, for the Si-implanted and annealed sample at the same temperature, the acceptor and donor concentrations were obtained as 8.4 $\times 10^{18}$ and 3.9×10^{17} cm^{-3}, respectively and acceptor ionization energy was around 150 meV. As observed from SDSA analysis, the hole and donor concentrations increase with Si-implantation, whereas the ionization energy decreases when compared with the as-grown and N-implanted samples. Such a behavior may be associated with the compensation of the previously presented levels by the Si ions and introducing new impurity levels during implantation process.

Temperature dependent mobility variation showed that all the undoped and implanted samples obey the power law $\mu \propto T^n$ with different n values depending on interstitial impurities and inter-layer defects which produce two dimensional

accumulation layer. The room temperature mobility of the as-grown sample was found to be 20 $cm^2/V.s$, while the mobilities of the N-implanted and annealed samples (A2 and A3) at room temperature were 52 and 13 $cm^2/V.s$, respectively. For the as-grown sample, while at lower temperature the Hall mobility is limited by ionized impurity scattering, at the high temperature above 240 K, the scattering of holes was mainly due to phonon scattering. The temperature dependence of the Hall mobility for the N-implanted and at 500^oC sample showed abrupt increase and decrease toward higher temperatures regions. In these temperature regions, the ionized impurity and phonon scattering mechanisms are effective, respectively. As a consequence of the Hall effect measurements, we observed that annealing of the samples at 700^oC extended the effective range of impurity scattering mechanisms is shifted toward higher temperature regions. The scattering of holes was mainly due to phonon scattering for Si-implanted and annealed at 500 ^{o}C sample at low temperatures. Above the room temperature, nearly temperature independent mobility variation was observed which can be ascribed to the neutral impurity scattering mechanism.

Furthermore, space-charge limited current measurements were carried out to identify the localized levels in as-grown GaSe single crystals in the temperature range of 100-450 K. From these measurements, localized energy level E_t has been found as 240 meV with trap density N_t=5.1×10^{12} cm^{-3}. This is in agreement with level obtained by conductivity measurements in this study.

To deduce the nature of impurity levels introduced during the implantation, photoconductivity (σ_ϕ) measurements have been carried out as a function of

temperature and illumination intensity. It was seen that the photoconductivity values of unimplanted sample much more greater than that of implanted and annealed samples under the illumination. Temperature dependent photoconductivity measurements under different light intensity showed that the photoconductivity increases exponentially with increasing temperature, and also increases with increasing illumination intensity at each absolute temperature with different activation energies. Therefore, the photoconductivity is governed by trapping or recombination centers above the valance band depending on the temperature and illumination intensity. A temperature insensitive photoconductivity was also observed with the increasing illumination intensities. This behavior was explained by the fully ionized impurity levels introduced during the implantation. For the characterization of trapping or recombination centers, photocurrent vs illumination intensity (ϕ) characteristics of all samples were measured at a constant electric field. These measurements showed an increase of photocurrent with increasing temperature and these dependencies were of the $I_{pc} \propto \phi^n$ type. The n values for all the samples were found in between 1 and 2. The super-linear behavior of photoconductivity is associated with the two-center effects, such as the incorporation of additional imperfections, and it leads to a larger lifetime for one of the carriers than previously presented. Therefore, this behavior was explained by the continuous trapping levels produced by the implantation of N- and Si-atoms and activated by the effect of annealing.

For the spectral analysis, the spectral distribution of photocurrent of the undoped and implanted samples were also measured in the wavelength of 500-700

nm. The maximum response of PC spectra was obtained at 2.06 eV at 50 K and 1.96 eV at 320 K for undoped as-grown GaSe single crystal. However, the maximum response of N- and Si-implanted and annealed samples were obtained at 2.03 eV and 2.04 eV, respectively. This variation on maximum response of the PC spectra reveals that N- and Si- implantation into GaSe single crystals together with annealing has a pronounced effect on the photoconductive properties and it was attributed to the N- and Si-modification and doping of the semiconductor. The same variation steamed from the implantation and post annealing was observed from the transmission measurements of the undoped and implanted samples. The observed decreases in the band gap was explained with the structural defects induced by the implantation with subsequent annealing. The same decrease was also observed as a result of spectral-photoconductivity measurements.

Finally, from the photoluminescence measurements of the undoped GaSe single crystals, three emission bands were observed at 2.114, 2.090 and 2.060 eV, respectively at 36 K. The line at 2.114 eV was attributed to the well known recombination of the direct free exciton (DFE). Considering the ionization energy of the DFE (20 meV), it was concluded that the bottom of the direct conduction band at 36 K lies at about 2.134 eV above the top of valance band. The emission line at 2.090 eV is due to direct bound exciton (DBE). By using the effective-mass approximation, it was found that this line is caused by the recombination of direct exciton bound to neutral acceptor at about 250 meV above the valance band. The emission line observed at 2.060 eV was explained by the

intra-center transitions between trap states since, this line was only seen at the low temperature and disappeared rapidly with increasing temperature.

REFERENCES

[1] B. G. Streetman. *Solid State Electronic Devices*. Prentice-Hall, New Jersey, 1995.

[2] G. Fisger and J. L. Brenber. *J. Phys. Chem. Solids*, 23:1363, 1962.

[3] M. K. Anis and F. M. Nazar. *J. Mater. Sci. Lett.*, 2:471, 1983.

[4] V. Capozzi. *Phys. Rev. B*, 28(8):4620, 1983.

[5] O. Karabulut, M. Parlak, R. Turan, U. Serincan, E. Tasarkuyu, and B. G. Akinoglu. *Crystal Res. and Techn.*, 38(9):811, 2003.

[6] O. Karabulut, M. Parlak, K. Yilmaz, R. Turan, and B. G. Akinoglu. *Crystal Res. and Techn.*, 38(12):1071, 2003.

[7] J. V. McCanny and R. B. Murray. *J. Phys. C Solid State*, 10(8):1211, 1977.

[8] R. H. Tregold and A. Clark. *Solid State Commun.*, 7:1519, 1969.

[9] M. K. Anis. *J. Crystal Growth*, 55:465, 1981.

[10] A. Kuhn, R. Chevalier, and A. Rimsky. *Acta Crystallogr. Sec. B*, 31:2841, 1975.

[11] J. C. J. M Terhell and R. M. a. Lieth. *J. Crys. Growth*, 16:54, 1972.

[12] A. Gouskov, J. Camassel, and L. Gouskov. *Crystal Growth and Charact.*, 5:323, 1982.

[13] A. Kuhn, A. Chevy, and R. Chevalier. *Phys. Stat. Sol. (a)*, 31:469, 1975.

[14] J. F. Sanchez-Royo, D. Errandonea, A. Segura, , L. Roa, and A. Chevy. *J. Appl. Phys.*, 83(9):4750, 1998.

[15] M. Schluter. *Nuovo Cimenti*, 13 B:313, 1973.

[16] J. P. Voitchovsky and A. Mercier. *Il. Nuovo Cimento*, 22B:273, 1974.

[17] V. L. Cardetta, A. M. Mancini, and A. Rizzo. *J. Crys. Growth*, 16:183, 1972.

[18] T. Ishii and N. Kambe. *J. Crys. Growth*, 76:489, 1986.

[19] A. Kuhn, A. Chevy, and E. Lendvay. *J. Crys. Growth*, 13/14:380, 1972.

[20] F. Levy. *Il. Nuovo Cimento*, 38 B(2):359, 1977.

[21] R. Fivaz and E. Mooser. *Phys. Rev.*, 163:743, 1967.

[22] C. Manfredotti, A. M. Mancini, R. Murri, A. Rizzo, and L. Vasanelli. *II Nuovo Cimento B*, 39:257, 1977.

[23] V. Augelli, C. Manfredotti, R. Murri, and L. Vasanelli. *Phys. Rev. B*, 17(8):3221, 1978.

[24] Ph. Schmid and E. Mooser. *Helv. Phys. Acta.*, 45:870, 1972.

[25] S. Shigetomi, I. Ikari, and H. Nakashima. *Japn. J. Appl. Phys.*, 39:5083, 2000.

[26] V. Capozzi, S. Caneppele, M. Montagne, and F. Levy. *Phys. Stat. Sol. (b)*, 129:247, 1985.

[27] E. Mooser and M. Schluter. *Nuovo Cimento B*, 18:164, 1973.

[28] V. L. Cardetta, A. M. Mancini, C. Manfredotti, and A. Rizzo. *J. Crys. Growth*, 17:155, 1972.

[29] C. Manfredotti, A. Rizzo, C. De Blasi, , S. Galassini, and L. Ruggiero. *J. Appl. Phys*, 46:4531, 1975.

[30] C. Manfredotti, R. Murri, A. Rizzo, S. Galassini, and L. Ruggiero. *Phys. Rev. B*, 10(8):3387, 1974.

[31] V. Capozzi, G. Mariotto, M. Montagne, A. Cingolani, and A. Minafra. *Phys. Stat. Sol. (a)*, 40:93, 1977.

[32] G. Micocci, A. Serra, and A. Tepore. *Phys. Stat. Sol.(a)*, 162:649, 1997.

[33] G. Micocci, A. Serra, and A. Tepore. *J. Appl. Phys.*, 82(5):2365, 1997.

[34] S. Shigetomi, T. Ikari, and H. Nakashima. *Jpn. J. Appl. Phys.*, 35:4291, 1996.

[35] S. Shigetomi, I. Ikari, and H. Nakashima. *J. Appl. Phys.*, 73:4686, 1993.

[36] S. Shigetomi, T. Ikari, and H. Nakashima. *J. Appl. Phys.*, 69(11):7936, 1991.

[37] S. Shigetomi, T. Ikari, and H. Nakashima. *Jpn. J. Appl. Phys.*, 32:2731, 1993.

[38] S. Shigetomi, I. Ikari, and H. Nakashima. *J. Appl. Phys.*, 80:4779, 1996.

[39] B. G. Tagiev, G. M. Niftiev, and F. S. Aidaev. *Phys. Stat. Sol. (b)*, 128:K65, 1985.

[40] S. Shigetomi and T. Ikari. *Philosophical Magazine Letters*, 79:575, 1999.

[41] S. Shigetomi, T. Ikari, and H. Nakashima. *Phys. Stat. Sol. (a)*, 160:159, 1997.

[42] S. Shigetomi, T. Ikari, and H. Nakashima. *J. Appl. Phys.*, 74(6):4125, 1993.

[43] B. Gurbulak, M. Yildirim, S. Tuzemen, H. Efeoglu, and Y. K. Yogurtcu. *J. Appl. Phys.*, 83:2030, 1998.

[44] S. Shigetomi, T. Ikari, and H. Nakashima. *Phys. Stat. Sol. (a)*, 156:k21, 1996.

[45] J. F. Sanchez-Royo, A. Segura, A. Chevy, and L. Roa. *J. Appl. Phys.*, 79:204, 1996.

[46] V. Capozzi and A. Minafra. *Solid State Commun.*, 38:341, 1981.

[47] J. W. Mayer, L. E. Eriksson, and J.A. Davies. *Ion Implantation in Semiconductors*. New York, 1970.

[48] I. V. Markov. *Crystal Growth for Beginners*. Singapore, 1998.

[49] J.C. Brice. *Crystal Growth Processes*. NY, 1986.

[50] B. D. Cullity. *Elements of X-Ray Diffraction*. Addison-Wesley, Second Edition, 1978.

[51] P. E. Werner, L. Eriksson, and M. Westdahl. *J. Appl. Cryst.*, 18:367, 1985.

[52] R. H. Bube. *Photoconduvtivity of Solids*. Jhon Wiley and Sons, Inc., NY, 1962.

[53] D. K. Schroder. *Semiconductor Material and Device Characterization*. Jhon Wiley and sons, NY, 1990.

[54] E. H. Putley. *The Hall Effect and Semi-Conductor Physics*. N.Y., 1960.

[55] N. F. Mott. *Electronic Processes in Non-Crystilline Materials*. Oxford, 1973.

[56] J. G. Simmons. *DC Conduction in Thin Films*. London, 1971.

[57] V. K. Mathur and R. P. Dahiya. *Solid State Electronics*, 17:61, 1974.

[58] R. H. Bube. *Photoelectronic Properties of Semiconductors*. Cambridge University Press, Cambridge, 1992.

[59] J. S. Blackmore. *Semiconductor Statistics*. Pergamon Press, N.Y., 1962.

[60] S. Pertkowitz. *Optical Characterization of Semiconductor: Infrared, Raman, and Photoluminescence spectroscopy*. Academic Press, London, 1993.

[61] J.I. Pankove. *Optical Processes in Semiconductor*. Prentice-Hall Inc., London, 1971.

[62] J. J. Gilman. *The Art and Science of Growing Crystals*. Jhon Wiley and Sons,Inc., London, 1963.

[63] Crystalox. *MSD4000 Operation Manual*. Crystalox Com., 1994.

[64] J. F. Ziegler, J. P. Biersack, and U. Litmark. *The Stopping and Range of Ions in Solids, Vol.1*. N.Y., 1985.

[65] L. J. Van der Pauw. *Philips Res. Repts.*, 13:1, 1958.

[66] P. H. Hemenger. *Rev. Sci. Instrum.*, 44(6):698, 1973.

[67] H. C. Montgomery. *J. Appl. Phys.*, 42(7):2971, 1970.

[68] L. Eriksson and M. Westdahl. *J. Appl. Cryst*, 18:367, 1985.

[69] JCPDS. *International Center for Difraction Data*, 1988.

[70] N. Benramdane, J. P. Guesdon, and C. Julien. *Phys. Stat. Sol.(a)*, 146:675, 1994.

[71] S. Shigetomi, T. Ikari, and N. Nishimura. *Phys. Stat. Sol.(a)*, 185(2):341, 2001.

[72] I. M. Aliev, A. R. Gadzhiev, and B. G. Tagirov. *Sov. Phys. Semicond.*, 15:1399, 1981.

[73] P. Singh, K. L. Bhatia, N. Kishore, N. Singh, S. K. Malik, and D. Kanjilal. *J. Non-Crystalline Materials Solids*, 191:146, 1995.

[74] D. K. Paul and S. S. Mitra. *Phys. Rev. Letter*, 31:1000, 1973.

[75] R. C. Da Silva, E. Alves, and M. M. Cruz. *Nucl. Instr. and Meth. in Phys. Res. B*, 191:158, 2002.

[76] B. Mari, A. Segura, and A. Chevy. *Applied Surface Science*, 50:415, 1991.

[77] H. S. Guder, B. Abay, H. Efeoglu, C. Coskun, S. Aydogan, and Y. K. Yogurtcu. *Turk. J. Phys.*, 25:523, 2001.

[78] A. Segura, C. Martinez-Tomas, A. Casanovas, A. Martinez-Poster, and A. Chevy. *Appl. Phys. A*, 48:445, 1989.

[79] S. Pall and D. N. Bose. *Solid State Comun.*, 97:725, 1996.

[80] M. A. Lampert and P. Mark. *Current Injection in Solids*. Academic, N.Y., 1970.

[81] M. K. Anis and A. R. Piercy. *J. Phys. D: Appl. Phys.*, 17:1229, 1984.

[82] C. Chakrabarti, B. Maiti, S. Chaudhuri, and A. K. Pal. *Solar Energy Mater. Sol. Cells*, 43:237, 1996.

[83] S. Roy, B. Bhattacharjee, S. N. Kundu, S. Chaudhuri, and A. K. Pal. *Materials Chem. and Phys. Semicond.*, 77:1079, 2003.

[84] V. I. Tagirov, G. B. Abdullaev, M. A. Sobeikh, and V. M. Salmanov. *Sov. Phys. Semicond.*, 11:1079, 1977.

[85] C. De Blasi, G. Micocci, A. Rizzo, and A. Tepore. *Phys. Stat. Sol.(a)*, 74:291, 1982.

[86] M. A. Osman. *Physica B*, 275:351, 2000.

[87] A. F. Qasrawi and N. M. Gasanly. *Phys. stat. sol. (a)*, 194(1):81, 2002.

[88] M. A. Osman, M. A. elosely, and A. A. Gadalla. *Physica B*, 252:216, 1998.

[89] Y. Shirakawa and H. Kukimato. *J. Appl. Phys.*, 51:2014, 1980.

[90] N. C. Giles, S. Hwang, J. F. Schetzina, S. McDevitt, and C. J. Johnson. *J. Appl. Phys.*, 64:2656, 1988.

[91] P. W. Yu and Y. S. Park. *J. Appl. Phys.*, 48:2434, 1977.

[92] E. A. Monte and G. J. Vangup. *J. Appl. Phys.*, 66:5549, 1989.

[93] T. K. Ozcan. *Optical Properties of GaSe Single Crystal. An Experimental Study.* M. Sc. thesis, METU, Ankara, 1996.

[94] Yu. P. Gnatenko. *Phys. Stat. Sol. (B)*, 161:419, 1990.

[95] W. Ungier, M. Suffczynski, and J. Adamowski. *Phys. Rev. B*, 24(4):2109, 1980.

[96] V. Capozzi and A. Minafra. *J. Phys. C: Solid State Phys.*, 14:4335, 1981.

[97] V. Capozzi. *Phys. Rev. B*, 23(2):836, 1981.

[98] B. G. Tagiev, G. M. Niftiev, and S. A. Abushov. *Phys. Stat. Sol. (b)*, 121:K195, 1985.

VITA

The author, Orhan Karabulut, was born in Elazığ in 1972. He began his studies in the department of Physics at the Atatürk University in 1988 and received his Bs.C degree in Physics in 1992. After he studied as a physics teacher in ministry of national education in between 1992-1995, joined the Physics Department of Pamukkale University as a research assistant and a M.Sc student. He received his M.Sc degree in 1997 and joined the Physics Department of METU as a research assistant and a Ph.D student.